



In situ synthesis of ultrafine TiO₂ nanoparticles modified g-C₃N₄ heterojunction photocatalyst with enhanced photocatalytic activity



Bin Zhang^{a,b,1}, Xu He^{b,1}, Xiaohan Ma^{a,1}, Qinghua Chen^a, Guocheng Liu^a, Yuanming Zhou^c, Dong Ma^a, Chunyue Cui^a, Jun Ma^{a,b}, Yanjun Xin^{a,*}

^a Qingdao Engineering Research Center for Rural Environment, College of Resource and Environment, Qingdao Agricultural University, Qingdao 266109, PR China

^b State Key Laboratory of Urban Water Resource and Environment, Harbin Institute of Technology, Harbin 150090, PR China

^c Central Laboratory, Qingdao Agricultural University, Qingdao 266109, PR China

ARTICLE INFO

Keywords:

Ultrafine TiO₂ nanoparticles
Graphitic carbon nitride
Tetracycline hydrochloride
Photodegradation

ABSTRACT

To improve the redox performance and light absorption property, the 2D/0D g-C₃N₄/TiO₂ heterojunction photocatalyst were successfully fabricated by co-annealing process based on melamine powder and ultrafine TiO₂ nanoparticles (about 9.87 nm) obtained from electrochemical etching technology. The surface micro-morphology, crystal structure, basic element composition, chemical structure, specific surface and optical performance were analyzed by SEM-EDS, TEM, HR-TEM, XRD, XPS, FTIR and Ultraviolet–visible diffuse reflection spectra (UV–vis DRS). The photocatalytic performance of g-C₃N₄/TiO₂ photocatalyst was assessed by the degradation of tetracycline hydrochloride (TC) under simulated sunlight irradiation. The results showed that the obtained TiO₂ powder had extremely smaller particle size and higher photocatalytic activity than commercial P25. The coupling of 0D TiO₂ nanoparticles and 2D g-C₃N₄ nanosheet further promoted the visible light absorption performance of TiO₂. The unique g-C₃N₄/TiO₂ heterojunction photocatalyst exhibited remarkable photocatalytic performance for the degradation of TC, whose degradation rate could reach to 99.40% under 120 min irradiation. The kinetic constant of the g-C₃N₄/TiO₂ photocatalyst was 1.48 times of that of TiO₂. The ESR results confirmed ·OH and ·O₂⁻ radicals produced in the photocatalytic process. This work could provide an effective reference for the fabrication of ultrafine TiO₂ powder and binary heterojunction photocatalyst with excellent photocatalytic activity for organic pollutants degradation in water purification.

1. Introduction

During the past decades, the water body has been largely destroyed due to the random discharge of organic pollutants [1]. Among them, tetracycline hydrochloride (TC), as an emerging antibiotic contaminant, has attracted widespread attention due to its high persistence and ecotoxicity [2]. Furthermore, TC is easily accumulated in the aquatic environment due to high solubility [3], which could seriously threaten the human health. Therefore, it is necessary for investigate economical and effective technology to remove TC in contaminated water. Photocatalysis, as an increasingly cost-effective technology, has a promising application for the degradation of organic pollutants in water. Semiconductor materials such as titanium dioxide (TiO₂) [4], graphite carbon nitride (g-C₃N₄) [5], tungsten trioxide (WO₃) [6] and cadmium sulfide (CdS) [7], play important roles in the field of photocatalysis [8,9]. Among numerous semiconductors, TiO₂ was considered

as a remarkable photocatalyst for its high stability [10], non-toxic [11], low cost [12], environmental friendly [13] and high reactivity [14].

In recent years, the commercial TiO₂ with an average particle size of 25 nm (P25) is widely considered as a successful catalyst with high photocatalytic activity [15]. The grain size of photocatalyst is one of the crucial factors determining photocatalytic activity by affecting its optical, specific surface area and other aspects [16–18]. Ultrafine particles (1–10 nm) with the size of the quantum effect can lead to blue shift of absorption band edge and enhance the specific surface area of catalysts [19,20]. And the quantization of size can increase charge transfer rate of semiconductor, reduce the probability of photo-generated electron-hole pair recombination and improve the efficiency of photocatalytic reaction [19]. In addition, studies have reported that ultrafine nanostructures can expose more active sites and exhibit enhanced quantum size effects, which will contribute to attractive photocatalytic performance [20]. Therefore, it is necessary to reduce the grain size of TiO₂

* Corresponding author.

E-mail address: xintom2000@126.com (Y. Xin).

¹ Bin Zhang, Xu He and Xiaohan Ma contribute equally to this work.

particles to achieve higher photocatalytic activity. Generally, the synthesis methods of TiO₂ nanoparticles mainly include hydrothermal [21], sol-gel [22], sputtering [23], etc [24–26]. But, the grain size of TiO₂ prepared by these methods is still larger (~20 nm or 50–60 nm), which limits the further improvement of the photocatalytic performance [22,27]. In addition, hydrothermal processes usually require for the creation of high temperature and pressure environment [21,28]. And the sol-gel method requires for the use of titanium salt with high cost, and the calcination process will produce extra carbon pollution [29,30]. The sputtering method has high requirements on equipment and technology [23,27], however, the recovery rate is low and cost is high. Compared with the these methods, the electrochemical etching method has the advantages of mild operational conditions, simple device, environmental friendliness, and can produce more uniform and ultrafine sized TiO₂ particles. In previous researches, we found that the TiO₂ nanoparticles obtained by electrochemical etching technology have smaller particle size and excellent photocatalytic activity compared with P25. In addition, the practical application of TiO₂ was limited due to the wide band gap (anatase: 3.2 eV), which leads to the low utilization of sunlight. Furthermore, the photocatalytic efficiency was unsatisfactory for the rapid recombination rate of photo-generated electron-hole pairs. Therefore, TiO₂ has been modified by various methods to improve its photocatalytic performance and response to visible light [24,31,32]. Among them, semiconductor coupling technique is regarded as an effective approach to improve the performance of photocatalyst.

G-C₃N₄, a fantastic metal-free semiconductor material [33], has attracted extensive attention for its suitable band gap, low price, simple and convenient in preparation, eco-friendliness and high chemical stability [34–37]. Particularly, g-C₃N₄ has a preferably absorption of visible light (< 460 nm) for the narrower band gap (2.7 eV). Nevertheless, the photocatalytic performance of g-C₃N₄ is restricted by high recombination rate of photo-generated electron-hole pairs [38]. For g-C₃N₄, the top of valence band (VB) and the bottom of conduction band (CB) are located at 1.60 eV and -1.10 eV vs normal hydrogen electrode (NHE), respectively [38]. Meanwhile, those of TiO₂ are located at 2.91 eV and -0.29 eV vs NHE [13], respectively. It can be seen that, g-C₃N₄ have stronger reduction capacity and weaker oxidation capacity, while TiO₂ showed stronger oxidation capacity and weaker reduction capacity. Therefore, the unique binary semiconductor photocatalyst, with strong oxidation and reduction capacity at the same time, could be constructed by coupling TiO₂ and g-C₃N₄ for the appropriate band position [39]. And the constructed g-C₃N₄/TiO₂ heterojunction photocatalyst might not only enhance visible light absorption performance, but also improve the separation efficiency of photo-generated carriers [40]. Thus, it is significant to fabricate and analyze the properties of g-C₃N₄/TiO₂ composite photocatalyst using the ultrafine TiO₂ nanoparticles with high active.

Based on the above discussion, the highly active ultrafine TiO₂ nanoparticles were successfully prepared by electrochemical etching process, and the g-C₃N₄/TiO₂ heterojunction photocatalyst was further fabricated via in situ synthesis by the annealing of melamine powder and ultrafine TiO₂ nanoparticles. The surface morphology, crystal structure, element composition, surface area, chemical structure and optical properties of composite photocatalyst were analyzed. Moreover, the photocatalytic property and mechanism for the removal of TC was also studied in depth.

2. Experiments

2.1. Chemicals and materials

Titanium foils (purity > 99.8%, 0.2 mm thickness) were obtained from Dongguan Tai Fu Metal Materials limited company (Co. LTD). Degussa P25 was purchased from Shaoxing Lijie chemical Co. LTD. TC (99.7%) was purchased from Shanghai Aladdin reagent Co. LTD. Other

reagents were purchased as analytical pure from Sinopharm Chemical Reagent Co. LTD. All solutions were prepared with deionized water.

2.2. Photocatalyst preparation

The highly active ultrafine TiO₂ nanoparticles were obtained from the electrochemical etching process. Prior to electrochemical etching, Ti foils were pretreated as follows: (1) Soaking in hydrofluoric acid solution to remove the oxide film on the surface. (2) Ultrasonic cleaning in deionized water, mixed solution of ethanol and acetone, and deionized water in series. The electrochemical etching process was carried out in a glass reactor containing a mixed electrolyte solution of Na₂SO₄ (1 mol/L) and NaF (0.5 wt%). The as-pretreated Ti foils (the reaction area is 40 mm × 10 mm) and Pt sheet were used as anode and cathode, respectively. The distance between the two electrodes was 2 cm. Meanwhile, the conditions of the electrochemical etching process were controlled at constant voltage of 20 V and temperature of 25°C. Ultrafine TiO₂ powder was etched from the Ti foils and deposited on the bottom of the glass reactor. Then ultrafine TiO₂ powder is further collected through filtration. And ultrafine TiO₂ powder was washed with acid, alkaline and deionized water, respectively, until the pH value was approached to 7. Then, the ultrafine TiO₂ nanoparticles were dried at 80°C for further use.

The g-C₃N₄/TiO₂ heterojunction photocatalyst was prepared by a simple annealing method. In details, the precursor of composite photocatalyst was obtained by melamine powder mixed with TiO₂ nanoparticles in a certain proportion (yield-mass ratio). Then, the g-C₃N₄/TiO₂ composite photocatalyst was obtained by annealing in tube furnace at 500 °C under nitrogen atmosphere for 2 h, with a heating rate of 5°C·min⁻¹. Subsequently, the g-C₃N₄/TiO₂ composite photocatalyst was further ground to uniform size. The mass ratio of TiO₂ to g-C₃N₄ was 5:1, which was marked as g-C₃N₄/TiO₂. Besides, the other mass ratio of TiO₂ to g-C₃N₄ was 10:1, 2:1, 1:1, 1:2, 1:5 and 1:10 which were denoted as CT10, CT2, CT1, CT0.5, CT0.2 and CT0.1. At the same time, pure g-C₃N₄ was prepared by the same method without addition of TiO₂.

2.3. Photocatalyst characterization

The surface morphology and elemental compositions of the samples were characterized by scanning electron microscope (SEM, Japan JEOL 7500F) with energy dispersive X-ray spectrometer (EDS). The micro-morphology and structure of g-C₃N₄/TiO₂ were investigated by high-resolution transmission electron microscopy (HR-TEM, Tecnai G2 F20). The crystal structure was investigated by X-ray Powder Diffractometer (XRD, Bruker AXS D8 ADVANCE) with Cu K α radiation (λ = 0.15418 nm). The average crystal size of all samples was calculated using the Scherrer's formula, $D = 0.89\lambda/\beta \cos \theta$ where D is the grain size, λ is the X-ray wavelength of 0.15418 nm, β is the line width at half-maximum and θ is Bragg angle. In order to measure the basic element composition of samples, X-ray photoelectron spectroscopy (XPS) was analyzed by Multifunctional imaging electron spectrometer (Thermo ESCALAB 250Xi) using an Al-K α X-ray (1486.6 eV) source at 150 W. In order to determine chemical structure, the samples were detected in a range of 400–4000 cm⁻¹ with a resolution of 4 cm⁻¹ by Fourier transform infrared spectroscopy (FTIR, Bruker Optics Tensor 27). The Brunauer-Emmett-Teller (BET) specific surface area and pore structure of the samples were investigated by specific surface and aperture analyzers (JW-BK122 W) in the relative pressure (P/P₀) range of 0.00–1.0. Ultraviolet-visible diffuse reflection spectra (UV-Vis DRS) were recorded by a spectrophotometer (Beijing Purkinje General Instrument Co, Ltd) with scanning wavelength of 200–800 nm using BaSO₄ as reference. The additive product of active radicals was detected by ESR technique (ELEXSYS-II E560, BRUKER). Specifically, •OH and •O₂⁻ radicals were determined using deionized water and methanol as solvent, respectively. Firstly, 1.5 mg of g-C₃N₄/TiO₂ was added to 5 mL

of the corresponding solvent. After xenon lamp illumination for three mins, the capillary tube were used for absorbed part of the solution to determine the generation of radicals.

2.4. Measurement of photocatalytic activity

The photocatalytic activity of samples was estimated by the degradation rate of TC under xenon lamp (150 W) irradiation. The quartz reactor contains photocatalyst (250 mg/L) and 40 mL TC solution (20 mg/L) with magnetic stirring. The distance between the quartz reactor and the xenon lamp was controlled at 2 cm. Before irradiation, TC solution was placed in the dark for 30 min to accomplish adsorption equilibrium. The concentration of TC was detected by HPLC (Agilent 1100, America) consisting of an Eclipse XDB-C18 column (4.6×150 mm, $5 \mu\text{m}$) at 30°C . The mobile phase was methanol/oxalic acid solution (0.05 M) = 4:6 with a 1.0 mL/min flow rate.

3. Results and discussions

3.1. SEM-EDS and TEM analysis

The surface micromorphology and elemental composition of all samples were characterized by SEM and EDS (Fig. 1). It could be seen that the prepared TiO_2 nanoparticles were irregular aggregates

(Fig. 1a). And the $\text{g-C}_3\text{N}_4$ sheets also showed an irregular two-dimension (2D) lamellar structure (Fig. 1b). For $\text{g-C}_3\text{N}_4/\text{TiO}_2$ composite photocatalyst, it could be clearly seen that some zero-dimension (0D) TiO_2 nanoparticles were scattered on $\text{g-C}_3\text{N}_4$ sheets (Fig. 1c), which showed the successful coupling of $\text{g-C}_3\text{N}_4$ and TiO_2 . Noticeably, 0D TiO_2 nanoparticles and 2D $\text{g-C}_3\text{N}_4$ sheets showed better dispersivity and ductility in $\text{g-C}_3\text{N}_4/\text{TiO}_2$, respectively, which might provide favorable conditions for the improvement of photocatalytic activity. The EDS result showed that the elemental composition of $\text{g-C}_3\text{N}_4/\text{TiO}_2$ photocatalyst were C, N, O and Ti, whose atomic ratio were 35.87%, 19.75%, 39.55% and 4.83%, respectively (Fig. 1d). Among them, C and N element came from $\text{g-C}_3\text{N}_4$. Furthermore, TEM and HR-TEM images of $\text{g-C}_3\text{N}_4/\text{TiO}_2$ were displayed in Fig. 1e and 1f. It could clearly observed that the ultrafine TiO_2 nanoparticles were attached to thin sheets of $\text{g-C}_3\text{N}_4$. And the HR-TEM image showed that the different lattice spacing were 0.350 nm and 0.326 nm, which corresponded to the crystal planes of TiO_2 (1 0 1) and $\text{g-C}_3\text{N}_4$ (0 0 2). The close connection of the two types of crystal planes indicated the formation of heterogeneous structures.

3.2. XRD characterization

The XRD spectra of etched TiO_2 were shown in Fig. 2a. The anatase TiO_2 (JCPDS 21-1272), rutile TiO_2 (JCPDS 21-1276) and brookite TiO_2 (JCPDS 29-1360) were marked with triangle, dot and rhombus,

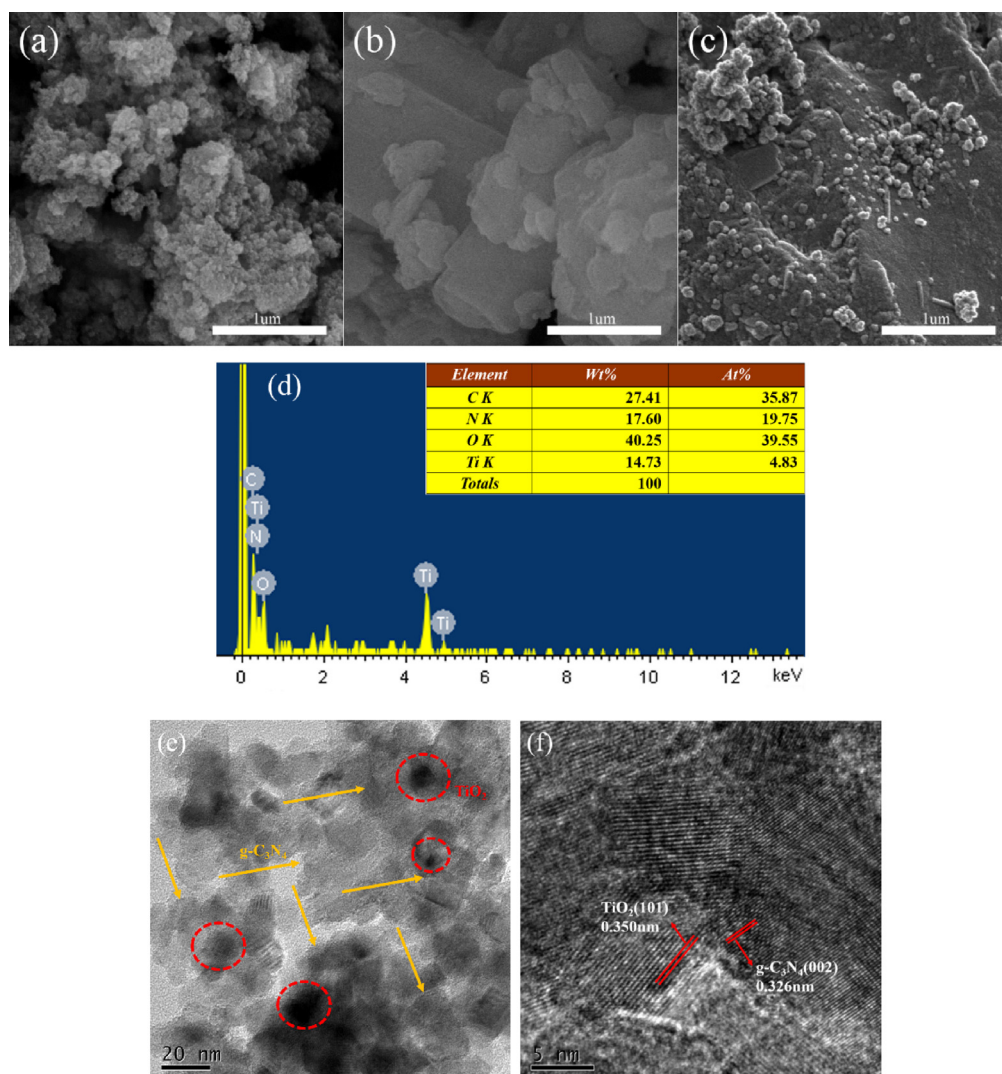


Fig. 1. SEM images of TiO_2 (a), $\text{g-C}_3\text{N}_4$ (b) and $\text{g-C}_3\text{N}_4/\text{TiO}_2$ (c); EDS of $\text{g-C}_3\text{N}_4/\text{TiO}_2$ (d) TEM (e) and HR-TEM (f) images of $\text{g-C}_3\text{N}_4/\text{TiO}_2$.

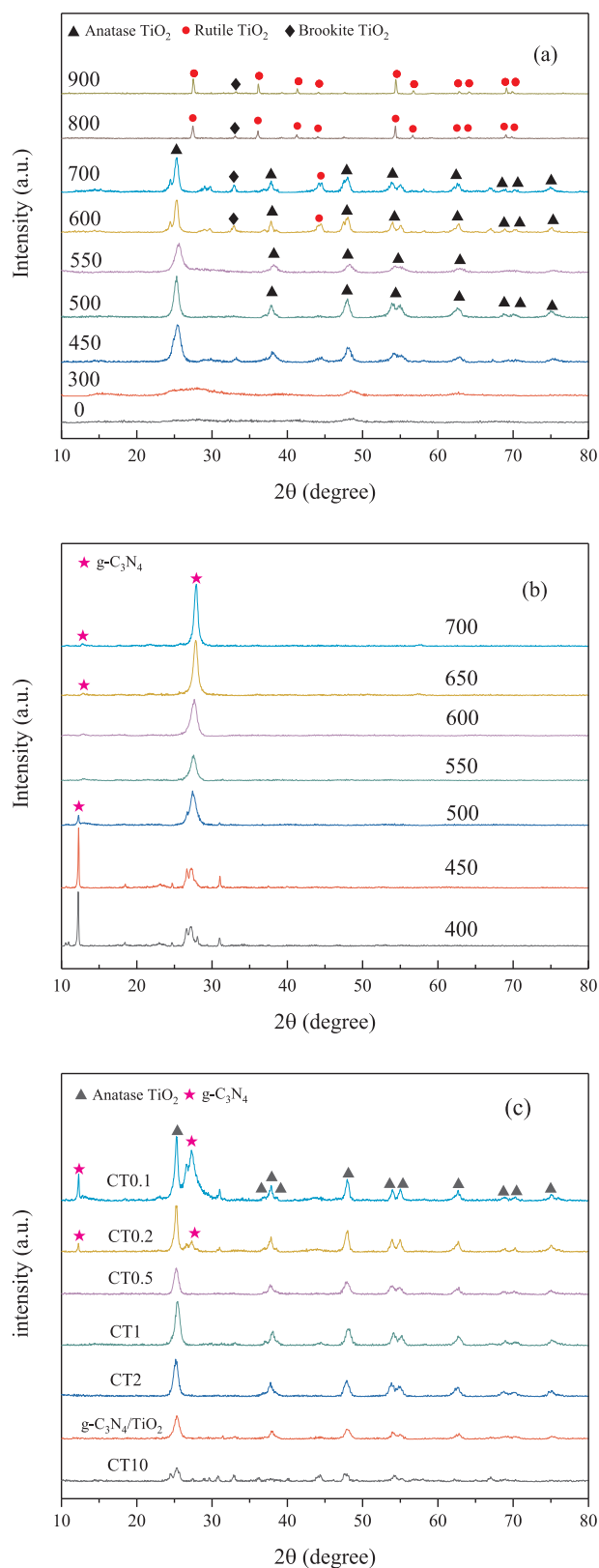


Fig. 2. XRD of TiO₂ (a) and g-C₃N₄ (b) annealed at different temperature; XRD of g-C₃N₄/TiO₂ (c) with different mass ratio annealed at 500 °C.

respectively. The peaks of g-C₃N₄ (JCPDS 87-1526) were marked with star. The unannealed TiO₂ particles were amorphous without any crystal peaks. And the crystal shape began to appear in TiO₂ samples after annealing. Along with the temperature increased to 600°C, rutile

TiO₂ characteristic peak appeared. All the anatase peaks disappeared and were replaced by rutile and brookite crystal peaks after the annealing temperature increased to 800°C. It is known that the particle size of P25 photocatalyst is about 25 nm. Interestingly, the average particle crystal size of etched TiO₂ powder was calculated as 9.87 nm. The much smaller particle size of ultrafine TiO₂ than that of P25 was more beneficial to the enhancement of photocatalytic performance [19]. Fig. 2b showed the XRD spectra of g-C₃N₄ annealed at different temperature. The characteristic peak approximately at 13° was identified as (1 0 0) facet of tri-s-triazine units [41]. The peak approximately at 27° was identified as (0 0 2) facet of interlayer spacing, which corresponding to the inter-planar staking of conjugated aromatic system [42,43]. In addition, the layer spacing of g-C₃N₄ conjugated aromatic systems were calculated as 0.326 nm, which was consistent with the literature [13].

Fig. 2c showed the XRD spectra of g-C₃N₄/TiO₂ with different TiO₂ and g-C₃N₄ annealed at 500 °C. It is obvious that the peak of g-C₃N₄ was not found in the g-C₃N₄/TiO₂ when the mass ratio of TiO₂ to g-C₃N₄ was larger than 0.5, which could be attributed to the lower g-C₃N₄ content. When the mass ratio of TiO₂ to g-C₃N₄ decreased to 0.2, the crystal surface peaks of g-C₃N₄ (1 0 0) and (0 0 2) facet appeared in the composite photocatalyst. The above results confirmed that g-C₃N₄/TiO₂ heterojunction photocatalyst has been successfully synthesized. The average crystal size of g-C₃N₄/TiO₂ was 9.08 nm, which was smaller than that of etched TiO₂ nanoparticles. The reduced particle size may be attributed to the enhanced dispersion of TiO₂ particles for the coupling of g-C₃N₄ (Fig. 1c), which would be favorable to improve photocatalytic activity.

3.3. XPS analysis

The XPS survey spectra of TiO₂, g-C₃N₄ and g-C₃N₄/TiO₂ were shown in Fig. 3a. The high-resolution C 1s, O 1s, Ti 2p and N 1s XPS spectra and fitting results of g-C₃N₄/TiO₂ composite photocatalyst were shown in Fig. 3b-e. Fig. 3a showed that the characteristic diffraction peak of N appeared in the full spectrum of g-C₃N₄/TiO₂ photocatalyst. And the atomic percentages of C, O, N, and Ti elements are 34.94%, 37.90%, 5.48% and 24.64%, respectively. As shown in Fig. 3b, the peak of C1s could be divided into three minor peaks at 248.7 eV, 286.3 eV and 288.5 eV, which could be identified as C-C or adventitious carbon [44], C-OH group [45] and N-C=N groups of g-C₃N₄, respectively. The peaks of O 1s located at 529.7 eV and 531.6 eV (Fig. 3c) were identified as Ti-O-Ti bond and surface -OH groups [46,47]. As shown in Fig. 3d, the two peaks centered at 464.5 eV and 458.3 eV correspond to Ti 2p 1/2 and Ti 2p 3/2, respectively. The space of 5.8 eV between Ti 2p 1/2 and Ti 2p 3/2 indicated the Ti element exists in the form of Ti⁴⁺ in TiO₂ [45]. The high-resolution N 1s spectrum of g-C₃N₄/TiO₂ showed two peaks located at 398.8 eV and 400.3 eV (Fig. 1c), which could be assigned to the sp²-hybridized aromatic nitrogen (C=N-C) and tertiary nitrogen (N-C₃) of g-C₃N₄, respectively [48,49]. These results, combined with the SEM (Fig. 1c) and XRD (Fig. 2c) analysis, indicated that the g-C₃N₄/TiO₂ photocatalyst has been successfully synthesized.

3.4. FTIR analysis

The chemical structure of the TiO₂, g-C₃N₄ and g-C₃N₄/TiO₂ was detected by FT-IR spectra (Fig. 4). For pure TiO₂, the absorption peak at 400–700 cm⁻¹ could be attributed to the stretching vibration of Ti–O–Ti bond [46,47]. The two characteristic peaks located at 1620 cm⁻¹ and 3400 cm⁻¹ were identified as the –OH groups and adsorbed H₂O, respectively. The peaks at 813 cm⁻¹ and 3154 cm⁻¹ belonged to the breathing mode of tri-s-triazine ring [50,51] and the stretching vibration of N-H bond [46,50] in g-C₃N₄, respectively. Furthermore, the peaks at 1240 cm⁻¹, 1330 cm⁻¹, 1409 cm⁻¹, 1460 cm⁻¹, 1580 cm⁻¹ and 1650 cm⁻¹ were corresponded to typical stretching vibration of C-N bonds in heterocycles [52,53]. For g-C₃N₄/

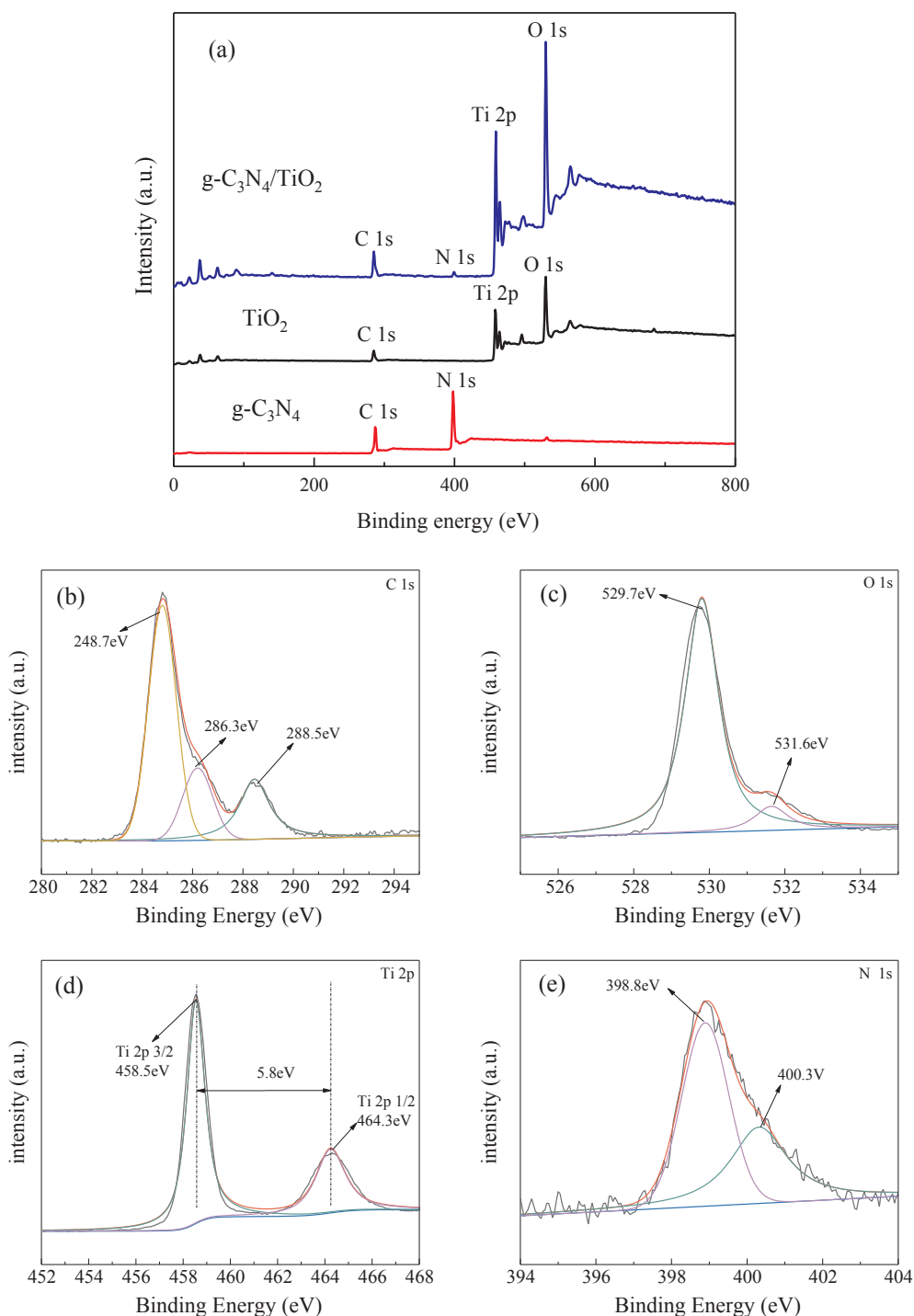


Fig. 3. (a) XPS survey spectra of TiO_2 , $\text{g-C}_3\text{N}_4$ and $\text{g-C}_3\text{N}_4/\text{TiO}_2$; high-resolution (b) C 1s, (c) O 1s, (d) Ti 2p and (e) N 1s XPS spectra of $\text{g-C}_3\text{N}_4/\text{TiO}_2$.

TiO_2 , the characteristic absorption peaks of both $\text{g-C}_3\text{N}_4$ and TiO_2 appeared in the spectrum, which proved that $\text{g-C}_3\text{N}_4$ and TiO_2 semiconductor materials were successfully coupled together. In addition, the position of Ti–O–Ti bond was slightly shifted compared with the TiO_2 spectra, which could be attributed to the heterogeneous interface formed between $\text{g-C}_3\text{N}_4$ and TiO_2 [47].

3.5. N_2 adsorption-desorption isotherms

In order to investigate BET specific surface area and pore size distribution of all samples, the N_2 adsorption-desorption isotherms and pore diameter distribution curves were shown in Fig. 5 and the average

pore diameter, pore volume and BET specific surface area of ultrafine TiO_2 , $\text{g-C}_3\text{N}_4$ and $\text{g-C}_3\text{N}_4/\text{TiO}_2$ were presented in Table 1. It could be clearly seen that all isotherms of $\text{g-C}_3\text{N}_4$, ultrafine TiO_2 and $\text{g-C}_3\text{N}_4/\text{TiO}_2$ belong to type IV of IUPAC classification (Fig. 5a), indicating these photocatalyst belonged to mesoporous (2–50 nm) adsorbent materials. At relative pressure range from 0.3 to 1.0, the typical H3 hysteresis loop appeared in the isotherm of $\text{g-C}_3\text{N}_4/\text{TiO}_2$ photocatalyst, implying the slit-like pores were formed by the accumulation of plate-like particles [38]. In addition, Fig. 5b showed that compared with $\text{g-C}_3\text{N}_4$, ultrafine TiO_2 and $\text{g-C}_3\text{N}_4/\text{TiO}_2$ photocatalyst have more mesoporous, and the mesoporous distribution characteristics were similar, which might be caused by the perfect dispersity of ultrafine TiO_2 on the $\text{g-C}_3\text{N}_4$

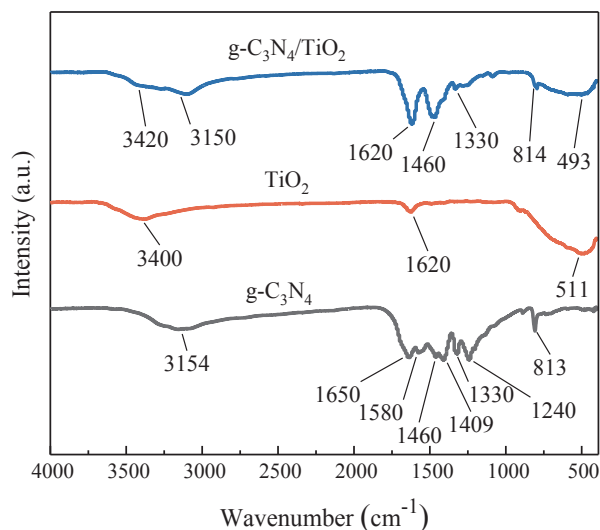


Fig. 4. FT-IR spectra of TiO₂, g-C₃N₄ and g-C₃N₄/TiO₂.

nanosheet. The abundant mesoporous pores could provide a large specific surface area.

Table 1 showed that both pore volume and pore diameter of g-C₃N₄/TiO₂ composites were smaller than that of ultrafine TiO₂, which could be attributed to the fact that ultrafine TiO₂ particles inserted into the g-C₃N₄ nanosheet layer and filled part of the pore channels with each other, resulting in the reduction of them. The TiO₂ particles have a larger specific surface area (90.042 m²/g) than P25 (50 m²/g) [54], which could be attributed to its ultra-fine particle size (Fig. 2). Besides, the BET specific surface area of g-C₃N₄/TiO₂ composite (97.26 m²/g) was larger than that of pristine TiO₂ and g-C₃N₄, which was also ascribed to the perfect dispersity of ultrafine TiO₂ on the g-C₃N₄ nanosheet (Fig. 1c). And a larger specific surface area might provide more active sites, which is advantageous to improve the adsorption of pollutants, thus improve the photocatalytic activity.

3.6. UV-vis characterization

As shown in Fig. 6a, the light absorption properties of ultrafine TiO₂, g-C₃N₄ and g-C₃N₄/TiO₂ photocatalyst were investigated. Obviously, in the ultraviolet region (200–390 nm), ultrafine TiO₂ has the strongest light absorption capacity, followed by g-C₃N₄/TiO₂ and pristine g-C₃N₄. In the visible light region (390–440 nm), the light

Table 1
Average pore diameter, Pore volume and BET specific surface area of TiO₂, g-C₃N₄ and g-C₃N₄/TiO₂.

Sample	Pore diameter (nm)	Pore Volume (cm ³ /g)	Specific surface area (m ² /g)
TiO ₂	13.66	0.31	90.04
g-C ₃ N ₄	12.50	0.05	15.79
g-C ₃ N ₄ /TiO ₂	11.55	0.28	97.26

absorption performance of the g-C₃N₄/TiO₂ composite was obviously stronger than that of pristine TiO₂. The results showed that the visible light absorption of TiO₂ was enhanced by g-C₃N₄. According to the Kubelka–Munk formula [45]:

$$(\alpha hv)^2 = A(hv - E_g)$$

where α , $h\nu$, E_g and A were absorption coefficient, the photon energy, the band gap and a constant, respectively. The $(A h\nu)^{1/2} \sim h\nu$ curves of all samples were shown in Fig. 6b. The calculation results showed the band gaps of TiO₂, g-C₃N₄ and g-C₃N₄/TiO₂ were 3.06 eV, 2.55 eV and 2.66 eV, respectively. Compared with ultrafine pristine TiO₂, the band gaps of g-C₃N₄/TiO₂ reduced 0.51 eV for the combining with g-C₃N₄. In a word, the coupling of g-C₃N₄ expanded the response range of visible light and promoted the separation efficiency of photon-generated carriers of TiO₂.

3.7. Photocatalytic performance

The photocatalytic activity of TiO₂, g-C₃N₄, and g-C₃N₄/TiO₂ was evaluated by photocatalytic degradation of TC. As shown in Fig. 7a, dark treatment was performed for 30 min to achieve adsorption-desorption equilibriums of TiO₂, g-C₃N₄ and g-C₃N₄/TiO₂ before illumination. For all photocatalysts, the rank of adsorption capacity was consistent with that of the specific surface area, and the adsorption capacity of g-C₃N₄/TiO₂ was strongest owing to the largest specific surface area (Fig. 5b and Table 1). Under 120 min irradiation, the photocatalytic degradation rate of TC by TiO₂, g-C₃N₄ and g-C₃N₄/TiO₂ were 95.81%, 90.16% and 99.40%, respectively. The photocatalytic degradation rate of TC could be described by pseudo-first-order reaction rate equation as follows:

$$\ln(C_0/C_t) = kt$$

where C_t is the TC concentration at reaction time t , C_0 was the TC concentration after adsorption equilibrium, and k is the kinetic rate constant.

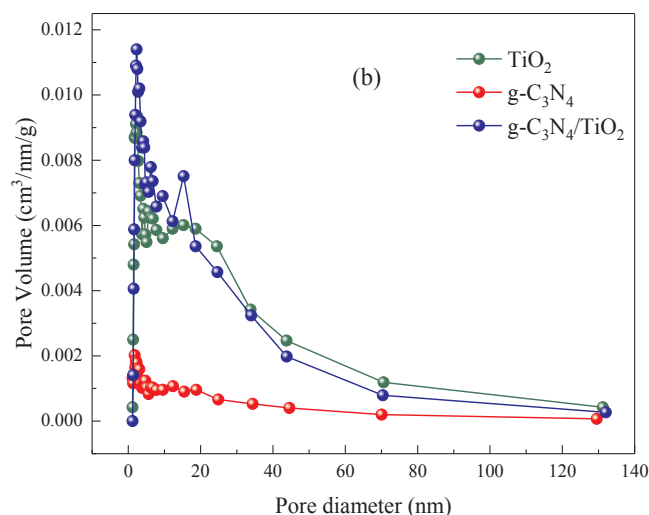
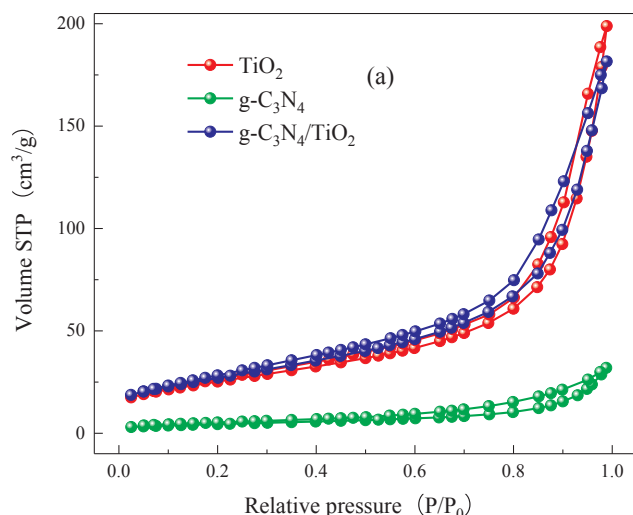


Fig. 5. N₂ adsorption-desorption isotherms (a) and pore diameter distribution curves (b) of TiO₂, g-C₃N₄ and g-C₃N₄/TiO₂.

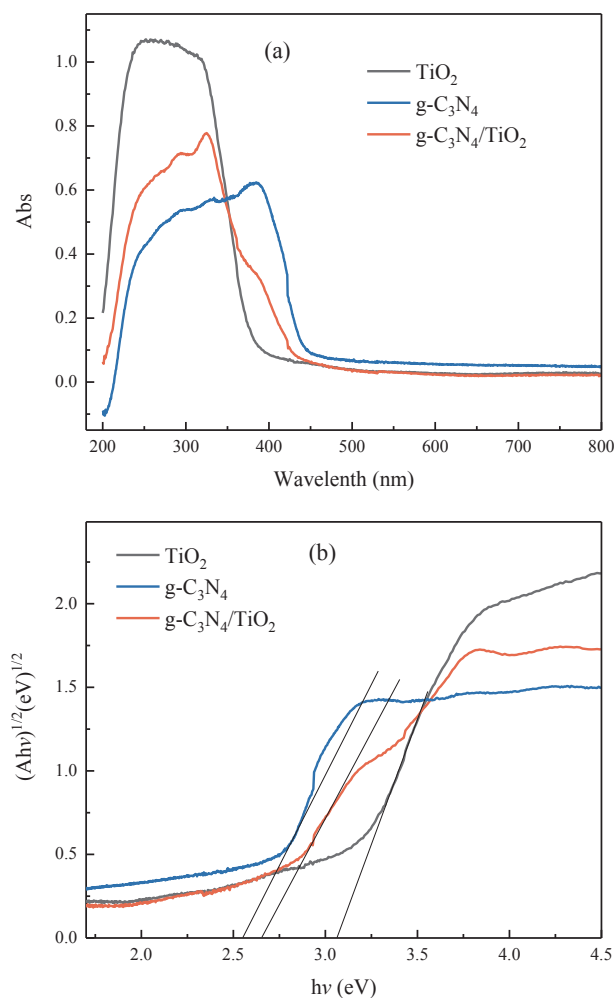


Fig. 6. (a) UV-vis absorption spectra of TiO_2 , $\text{g-C}_3\text{N}_4$ and $\text{g-C}_3\text{N}_4/\text{TiO}_2$ (b) $(Ah\nu)^{1/2} \sim hv$ curves of TiO_2 , $\text{g-C}_3\text{N}_4$ and $\text{g-C}_3\text{N}_4/\text{TiO}_2$.

As shown in Fig. 7b, the kinetic rate constants of P25, TiO_2 , $\text{g-C}_3\text{N}_4$ and $\text{g-C}_3\text{N}_4/\text{TiO}_2$ were 2.10 , 2.40 , 2.00 and $3.70 \times (10^{-4} \text{ min}^{-1})$, respectively. Obviously, $\text{g-C}_3\text{N}_4/\text{TiO}_2$ composite photocatalyst showed the highest degradation rate, which was attributed to the high specific surface area (Table 1) and ultrafine particle size (Fig. 2a) to provide more active sites. And pristine TiO_2 exhibited higher photocatalytic activity than P25 owing to the ultrafine particle size (Fig. 2) as well as large specific surface area (Fig. 5). Meanwhile, the size effect of ultrafine TiO_2 particles improves the separation efficiency of photo-generated electron-holes, resulting in prominent photocatalytic efficiency [19]. $\text{g-C}_3\text{N}_4$ has favorable visible-light absorption property (Fig. 6), but the position at the top of VB is not high enough to exhibit high oxidation capacity. At the same time, the photocatalytic property is limited because photo-generated electron holes are easy to recombine (Fig. 7). Particularly, the results showed that $\text{g-C}_3\text{N}_4/\text{TiO}_2$ had higher photocatalytic activity than $\text{g-C}_3\text{N}_4$, TiO_2 and P25, which could be attributed to the following reasons: (1) The heterogeneous structure were constructed due to the matching energy band structure between $\text{g-C}_3\text{N}_4$ and TiO_2 , which could promote the transfer of charge within the composite photocatalyst. Furthermore, the composite photocatalyst demonstrated strong oxidation and reduction capacity, thus improving the photocatalytic efficiency. (2) The improvement of visible light absorption performance could stimulate the photocatalyst to produce more photogenic electrons and holes, leading to the generation of more free radicals, which would be conducive to the further degradation of TC. (3) The improved adsorption performance of $\text{g-C}_3\text{N}_4/\text{TiO}_2$

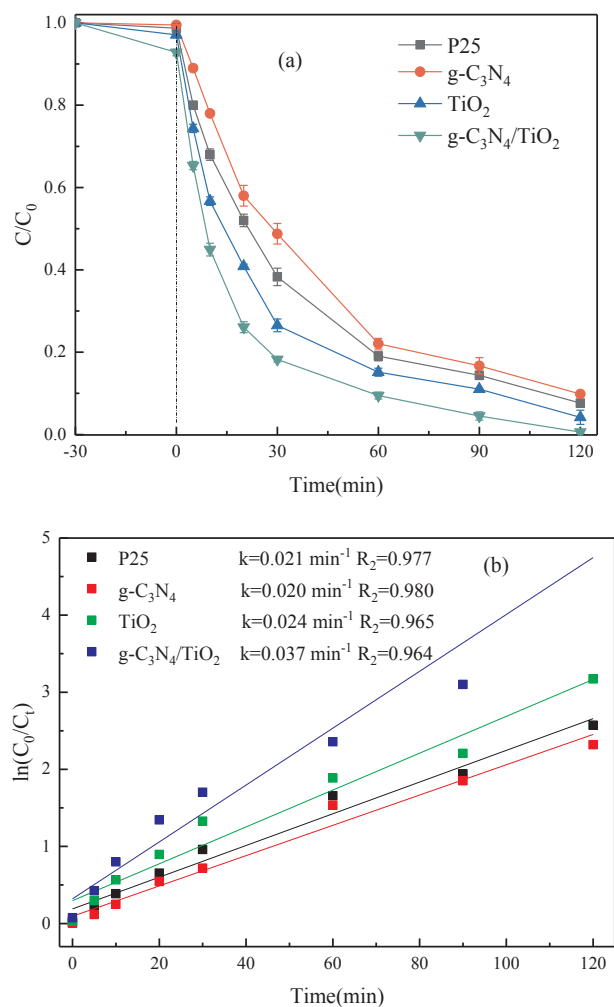


Fig. 7. (a) Photocatalytic degradation of TC and (b) pseudo first-order kinetics fitting curves of by TiO_2 , $\text{g-C}_3\text{N}_4$ and $\text{g-C}_3\text{N}_4/\text{TiO}_2$ under 120 min irradiation.

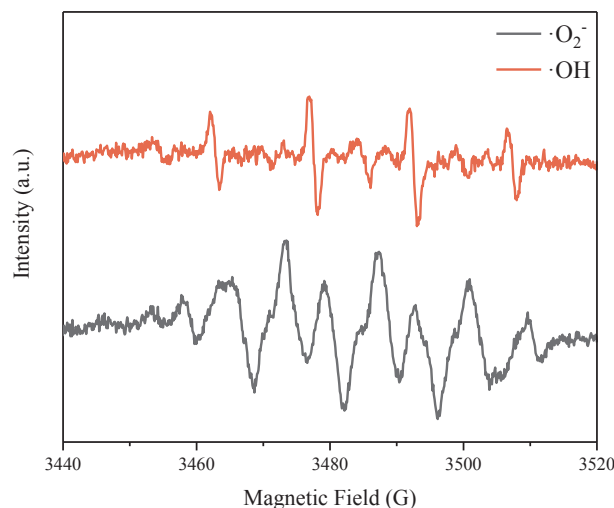


Fig. 8. ESR spectra of $\text{DMPO}\cdot\text{OH}$ and $\text{DMPO}\cdot\text{O}_2^-$ adducts of $\text{g-C}_3\text{N}_4/\text{TiO}_2$ under xenon lamp irradiation.

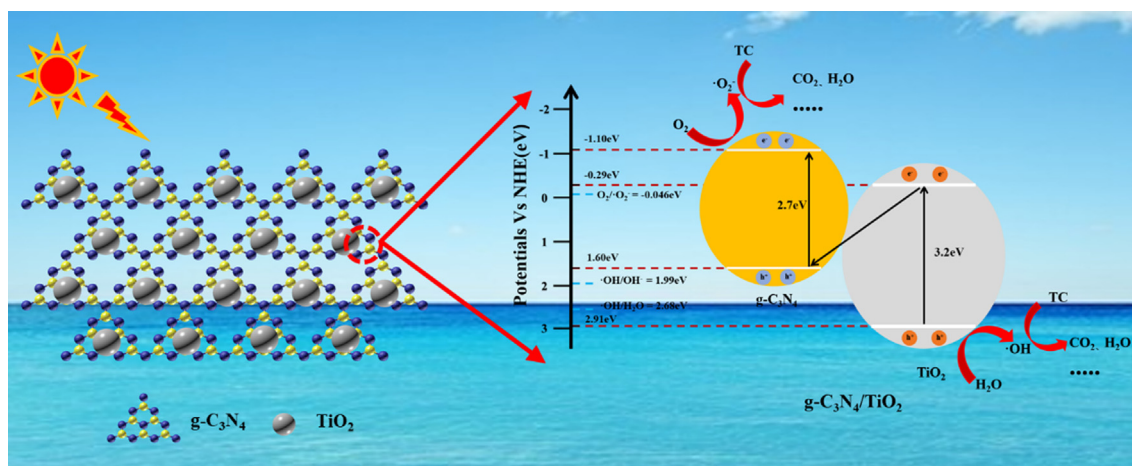


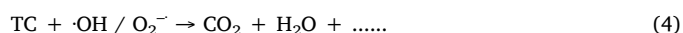
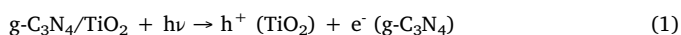
Fig. 9. Schematic diagrams for photocatalytic mechanism of $g\text{-C}_3\text{N}_4/\text{TiO}_2$ composite.

promoted the reaction rate of photocatalytic process [55].

3.8. Photocatalytic mechanism

To identify the presence of active species in photocatalytic processes, the ESR test of $g\text{-C}_3\text{N}_4/\text{TiO}_2$ was performed. And the ESR test results of the $g\text{-C}_3\text{N}_4/\text{TiO}_2$ were shown in Fig. 8. It can be clearly seen that adduct of hydroxyl radicals (DMPO- $\cdot\text{OH}$) have typical characteristic peaks of 1:2:2:1. In addition, the peak of superoxide radicals adduct (DMPO- $\cdot\text{O}_2^-$) was also detected, which confirmed that a large number of $\cdot\text{O}_2^-$ radicals were produced in the photocatalytic process. Based on the above results, $\cdot\text{O}_2^-$ radicals and $\cdot\text{OH}$ radicals were produced simultaneously during photocatalytic degradation.

As shown in Fig. 9, a probable photocatalytic degradation mechanism of TC for $g\text{-C}_3\text{N}_4/\text{TiO}_2$ photocatalyst was proposed. In the process of photocatalysis, $\cdot\text{O}_2^-$ and $\cdot\text{OH}$ radical play the vital role (Fig. 8). The VB potential positions of $g\text{-C}_3\text{N}_4$ and TiO_2 were 1.60 eV and 2.91 eV (vs. NHE), and their CB were -1.10 eV and -0.29 eV (vs. NHE), respectively [38,56]. The VB potential energy of $g\text{-C}_3\text{N}_4$ was lower than that of $\cdot\text{OH}/\text{H}_2\text{O}$ (2.68 eV vs NHE) and $\cdot\text{OH}/\text{OH}^-$ (1.99 eV vs NHE) [57] so that the hole cannot produce $\cdot\text{OH}$. Although both $g\text{-C}_3\text{N}_4$ and TiO_2 have the ability to produce $\cdot\text{O}_2^-$ radical for $\text{O}_2/\cdot\text{O}_2^-$ (-0.046 eV vs NHE) [58]. Nevertheless, the CB of $g\text{-C}_3\text{N}_4$ is more negative than of TiO_2 , so O_2 tend to react with electrons of $g\text{-C}_3\text{N}_4$ to form $\cdot\text{O}_2^-$. For pristine TiO_2 photocatalyst, after being illuminated by xenon lamp, the excited electrons could transit to the CB and the holes were left in the VB. But photo-electrons could easily return to the VB and recombine with hole. For $g\text{-C}_3\text{N}_4/\text{TiO}_2$ photocatalyst, both of $g\text{-C}_3\text{N}_4$ and TiO_2 were stimulated by photon energy to produce photo-generated electrons and holes [Eq. (1)]. Because the CB of $g\text{-C}_3\text{N}_4$ is more negative than that of TiO_2 , the electrons at the CB of $g\text{-C}_3\text{N}_4$ will migrate to the CB of TiO_2 , thus effectively inhibiting the recombination of photo-generated carriers. Furthermore, a heterojunction interface is formed between TiO_2 and $g\text{-C}_3\text{N}_4$ after the coupling of two semiconductors. And electrons on the CB of TiO_2 could bind to holes in the VB of $g\text{-C}_3\text{N}_4$ through the heterojunction interface [57]. This photocatalytic system could promote the rapid separation of photo-generated carriers, thus improve the light absorption performance (Fig. 6) and photocatalytic quantum efficiency (Fig. 7). In addition, the unique binary semiconductor photocatalyst has the stronger oxidation and reduction ability. And electrons could react with oxygen to form $\cdot\text{O}_2^-$ radicals [Eq. (2)], and holes could combine with H_2O to form $\cdot\text{OH}$ radicals [Eq. (3)]. TC will be degraded into small molecule organic compounds and finally mineralized to CO_2 and H_2O under the action of radicals [Eq. (4)].



4. Conclusions

In conclusion, $g\text{-C}_3\text{N}_4/\text{TiO}_2$ heterostructure photocatalyst were successfully synthesized via a co-annealing of melamine powder and ultrafine TiO_2 nanoparticles. The as-prepared ultrafine TiO_2 nanoparticles possessed finer size and exhibited higher photocatalytic activity. The coupling of $g\text{-C}_3\text{N}_4$ greatly improved the visible light absorption properties and photocatalytic activity of TiO_2 . The unique heterojunction photocatalyst has remarkable oxidation and reduction capacity. Furthermore, the semiconductor heterostructure formed by 2D $g\text{-C}_3\text{N}_4$ and 0D TiO_2 nanoparticles promoted the separation efficiency of photo-generated electron-hole pairs. Both $\cdot\text{OH}$ and $\cdot\text{O}_2^-$ radicals contribute to the photocatalytic process. In our work, the synthesis of $g\text{-C}_3\text{N}_4/\text{TiO}_2$ heterojunction photocatalyst will provide a reliable and effective basis for the treatment of antibiotic-contaminated wastewater.

CRedit authorship contribution statement

Bin Zhang: Investigation, Writing - original draft, Methodology, Formal analysis. **Xu He:** Writing - review & editing, Formal analysis. **Xiaohan Ma:** Methodology, Validation, Formal analysis. **Qinghua Chen:** Data curation, Formal analysis. **Guocheng Liu:** Data curation, Project administration. **Yuanming Zhou:** Data curation, Formal analysis. **Dong Ma:** Data curation, Formal analysis. **Chunyu Cui:** Data curation, Formal analysis. **Jun Ma:** Supervision. **Yanjun Xin:** Conceptualization, Writing - review & editing, Resources, Supervision, Funding acquisition.

Declaration of Competing Interest

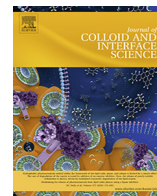
The authors declare that they have no known competing financial interests or personal relationships that could have appeared to influence the work reported in this paper.

Acknowledgements

This work was supported by National Natural Science Foundation of China (No. 51678323 and 51208274), Natural Science Foundation of Shandong Province (No. ZR2017MEE026), and Science and Technology Project of Shandong Province (No. J16LD02).

References

- [1] O.M.L. Alharbi, A.A. Basheer, R.A. Khattab, I. Ali, Health and environmental effects of persistent organic pollutants, *J. Mol. Liq.* 263 (2018) 442–453.
- [2] Y. Chen, Y. Ma, J. Yang, L. Wang, J. Lv, C. Ren, Aqueous tetracycline degradation by H₂O₂ alone: removal and transformation pathway, *Chem. Eng. J.* 307 (2017) 15–23.
- [3] H.M. Jang, E. Kan, A novel hay-derived biochar for removal of tetracyclines in water, *Bioresour. Technol.* 274 (2019) 162–172.
- [4] J. Low, B. Cheng, J. Yu, Surface modification and enhanced photocatalytic CO₂ reduction performance of TiO₂: a review, *Appl. Surf. Sci.* 392 (2017) 658–686.
- [5] J. Ding, S. Lu, L. Shen, R. Yan, Y. Zhang, H. Zhang, Enhanced photocatalytic reduction for the dechlorination of 2-chlorodibenzo-p-dioxin by high-performance g-C₃N₄/NiO heterojunction composites under ultraviolet-visible light illumination, *J. Hazard. Mater.* 384 (2019) 121255.
- [6] N. Lu, P. Wang, Y. Su, H. Yu, N. Liu, X. Quan, Construction of Z-Scheme g-C₃N₄/RGO/WO₃ with in situ photoreduced graphene oxide as electron mediator for efficient photocatalytic degradation of ciprofloxacin, *Chemosphere* 215 (2019) 444–453.
- [7] T. Di, B. Cheng, W. Ho, J. Yu, H. Tang, Hierarchically CdS–Ag₂S nanocomposites for efficient photocatalytic H₂ production, *Appl. Surf. Sci.* 470 (2019) 196–204.
- [8] J.S. Lee, J. Jang, Hetero-structured semiconductor nanomaterials for photocatalytic applications, *J. Ind. Eng. Chem.* 20 (2014) 363–371.
- [9] Z. Zhao, J. Fan, X. Deng, J. Liu, One-step synthesis of phosphorus-doped g-C₃N₄/Co₃O₄ quantum dots from vitamin B12 with enhanced visible-light photocatalytic activity for metronidazole degradation, *Chem. Eng. J.* 360 (2019) 1517–1529.
- [10] Z. Shayegan, C. Lee, F. Haghghat, TiO₂ photocatalyst for removal of volatile organic compounds in gas phase – a review, *Chem. Eng. J.* 334 (2018) 2408–2439.
- [11] S. Ni, F. Han, W. Wang, D. Han, Y. Bao, D. Han, H. Wang, L. Niu, Innovations upon antioxidant capacity evaluation for cosmetics: a photoelectrochemical sensor exploitation based on N-doped graphene/TiO₂ nanocomposite, *Sens. Actuat. B.* 259 (2018) 963–971.
- [12] N.O. Balayeva, M. Fleisch, D.W. Bahnemann, Surface-grafted WO₃/TiO₂ photocatalysts: Enhanced visible-light activity towards indoor air purification, *Catal. Today.* 313 (2018) 63–71.
- [13] C. Han, Y. Wang, Y. Lei, B. Wang, N. Wu, Q. Shi, Q. Li, In situ synthesis of graphitic-C₃N₄ nanosheet hybridized N-doped TiO₂ nanofibers for efficient photocatalytic H₂ production and degradation, *Nano Res.* 8 (2014) 1199–1209.
- [14] G. Zhang, H. Miao, X. Hu, J. Mu, X. Liu, T. Han, J. Fan, E. Liu, Y. Yin, J. Wan, A facile strategy to fabricate Au/TiO₂ nanotubes photoelectrode with excellent photoelectrocatalytic properties, *Appl. Surf. Sci.* 391 (2017) 345–352.
- [15] T. Wang, Y. Zhang, J. Pan, B. Li, L. Wu, B. Jiang, Hydrothermal reduction of commercial P25 photocatalysts to expand their visible-light response and enhance their performance for photodegrading phenol in high-salinity wastewater, *Appl. Surf. Sci.* 480 (2019) 896–904.
- [16] K. Kočí, L. Obalová, L. Matějová, D. Plachá, Z. Lačný, J. Jirkovský, O. Šolcová, Effect of TiO₂ particle size on the photocatalytic reduction of CO₂, *Appl. Catal. B: Environ.* 89 (2009) 494–502.
- [17] M. Ou, Q. Zhong, Y. Zhao, Y. Xue, F. Song, Graphene-decorated 3D BiVO₄ photocatalysts with controlled size and shape for efficient visible-light-induced photocatalytic performance, *Mater. Lett.* 184 (2016) 227–231.
- [18] K. Chen, Q. Fan, C. Chen, Z. Chen, A. Alsaedi, T. Hayat, Insights into the crystal size and morphology of photocatalysts, *J. Colloid Interface Sci.* 538 (2019) 638–647.
- [19] S.C. Shi-Jane Tsai, Effect of TiO₂ crystalline structure in photocatalytic degradation of phenolic contaminants, *Catal. Today.* 33 (1997) 227–237.
- [20] W. Wang, J. Fang, H. Chen, Nano-confined g-C₃N₄ in mesoporous SiO₂ with improved quantum size effect and tunable structure for photocatalytic tetracycline antibiotic degradation, *J. Alloys Compd.* 819 (2020).
- [21] Y. Yan, W. Kuang, L. Shi, X. Ye, Y. Yang, X. Xie, Q. Shi, S. Tan, Carbon quantum dot-decorated TiO₂ for fast and sustainable antibacterial properties under visible-light, *J. Alloys Compd.* 777 (2019) 234–243.
- [22] M.Z. Yahaya, M.Z. Abdullah, A.A. Mohamad, Centrifuge and storage precipitation of TiO₂ nanoparticles by the sol-gel method, *J. Alloys Compd.* 651 (2015) 557–564.
- [23] C. Bundesmann, T. Amelal, Secondary particle properties for the ion beam sputtering of TiO₂ in a reactive oxygen atmosphere, *Appl. Surf. Sci.* 485 (2019) 391–401.
- [24] M. Ge, J. Cai, J. Iocozzia, C. Cao, J. Huang, X. Zhang, J. Shen, S. Wang, S. Zhang, K. Zhang, Y. Lai, Z. Lin, A review of TiO₂ nanostructured catalysts for sustainable H₂ generation, *Int. J. Hydrogen Energy.* 42 (2017) 8418–8449.
- [25] H. Rasoulnezhad, G. Kavei, K. Ahmadi, M.R. Rahimpour, Combined sonochemical/CVD method for preparation of nanostructured carbon-doped TiO₂ thin film, *Appl. Surf. Sci.* 408 (2017) 1–10.
- [26] F. Shi, Y. Li, H. Wang, Q. Zhang, Formation of core/shell structured polystyrene/anatase TiO₂ photocatalyst via vapor phase hydrolysis, *Appl. Catal. B: Environ.* 123–124 (2012) 127–133.
- [27] S. Park, J. Heo, Characteristics of N-doped titanium oxide prepared by the large scaled DC reactive magnetron sputtering technique, *Sep. Purif. Technol.* 58 (2007) 200–205.
- [28] S. S. K.L. Nagashree, T. Maiyalagan, G. Keerthiga, Photocatalytic degradation of 2, 4-dichlorophenoxyacetic acid – a comparative study in hydrothermal TiO₂ and commercial TiO₂, *Appl. Surf. Sci.* 449 (2018) 371–379.
- [29] M. Lafjah, F. Djafri, A. Bengueddach, N. Keller, V. Keller, Beta zeolite supported sol-gel TiO₂ materials for gas phase photocatalytic applications, *J. Hazard. Mater.* 186 (2011) 1218–1225.
- [30] Y. Wang, Y. He, Q. Lai, M. Fan, Review of the progress in preparing nano TiO₂: an important environmental engineering material, *J. Environ. Sci. (China)* 26 (2014) 2139–2177.
- [31] H. Dong, G. Zeng, L. Tang, C. Fan, C. Zhang, X. He, Y. He, An overview on limitations of TiO₂-based particles for photocatalytic degradation of organic pollutants and the corresponding countermeasures, *Water Res.* 79 (2015) 128–146.
- [32] V. Etacheri, C. Di Valentin, J. Schneider, D. Bahnemann, S.C. Pillai, Visible-light activation of TiO₂ photocatalysts: advances in theory and experiments, *J. Photochem. Photobiol. C Photochem. Rev.* 25 (2015) 1–29.
- [33] J. Fu, Q. Xu, J. Low, C. Jiang, J. Yu, Ultrathin 2D/2D WO₃/g-C₃N₄ step-scheme H₂-production photocatalyst, *Appl. Catal. B: Environ.* 243 (2019) 556–565.
- [34] L. Jiang, X. Yuan, Y. Pan, J. Liang, G. Zeng, Z. Wu, H. Wang, Doping of graphitic carbon nitride for photocatalysis: a review, *Appl. Catal. B: Environ.* 217 (2017) 388–406.
- [35] G. Mamba, A.K. Mishra, Graphitic carbon nitride (g-C₃N₄) nanocomposites: a new and exciting generation of visible light driven photocatalysts for environmental pollution remediation, *Appl. Catal. B: Environ.* 198 (2016) 347–377.
- [36] D. Masih, Y. Ma, S. Rohani, Graphitic C₃N₄ based noble-metal-free photocatalyst systems: a review, *Appl. Catal. B: Environ.* 206 (2017) 556–588.
- [37] M. Xiao, B. Luo, S. Wang, L. Wang, Solar energy conversion on g-C₃N₄ photocatalyst: light harvesting, charge separation, and surface kinetics, *J. Energy Chem.* 27 (2018) 1111–1123.
- [38] D. Ma, J. Wu, M. Gao, Y. Xin, T. Ma, Y. Sun, Fabrication of Z-scheme g-C₃N₄/RGO/Bi₂WO₆ photocatalyst with enhanced visible-light photocatalytic activity, *Chem. Eng. J.* 290 (2016) 136–146.
- [39] L. Kong, X. Zhang, C. Wang, J. Xu, X. Du, L. Li, Ti³⁺ defect mediated g-C₃N₄/TiO₂ Z-scheme system for enhanced photocatalytic redox performance, *Appl. Surf. Sci.* 448 (2018) 288–296.
- [40] X. Wang, M. Liu, Photocatalytic enhancement mechanism of direct Z-scheme heterojunction O-g-C₃N₄@Fe-TiO₂ under visible-light irradiation, *Appl. Surf. Sci.* 485 (2019) 353–360.
- [41] X. Chen, J. Wei, R. Hou, Y. Liang, Z. Xie, Y. Zhu, X. Zhang, H. Wang, Growth of g-C₃N₄ on mesoporous TiO₂ spheres with high photocatalytic activity under visible light irradiation, *Appl. Catal. B: Environ.* 188 (2016) 342–350.
- [42] X. Song, Y. Hu, M. Zheng, C. Wei, Solvent-free in situ synthesis of g-C₃N₄/(001)TiO₂ composite with enhanced UV- and visible-light photocatalytic activity for NO oxidation, *Appl. Catal. B: Environ.* 182 (2016) 587–597.
- [43] Y. Tan, Z. Shu, J. Zhou, T. Li, W. Wang, Z. Zhao, One-step synthesis of nanostructured g-C₃N₄/TiO₂ composite for highly enhanced visible-light photocatalytic H₂ evolution, *Appl. Catal. B: Environ.* 230 (2018) 260–268.
- [44] S. Zhou, Y. Liu, J. Li, Y. Wang, G. Jiang, Z. Zhao, D. Wang, A. Duan, J. Liu, Y. Wei, Facile in situ synthesis of graphitic carbon nitride (g-C₃N₄)-N-TiO₂ heterojunction as an efficient photocatalyst for the selective photoreduction of CO₂ to CO, *Appl. Catal. B: Environ.* 158–159 (2014) 20–29.
- [45] G. Wang, Q. Chen, Y. Xin, Y. Liu, Z. Zang, C. Hu, B. Zhang, Construction of graphene-WO₃/TiO₂ nanotube array photoelectrodes and its enhanced performance for photocatalytic degradation of dimethyl phthalate, *Electrochim. Acta.* 222 (2016) 1903–1913.
- [46] X. Wang, F. Wang, C. Bo, K. Cheng, J. Wang, J. Zhang, H. Song, Promotion of phenol photodecomposition and the corresponding decomposition mechanism over g-C₃N₄/TiO₂ nanocomposites, *Appl. Surf. Sci.* 453 (2018) 320–329.
- [47] H. Wang, Y. Liang, L. Liu, J. Hu, W. Cui, Highly ordered TiO₂ nanotube arrays wrapped with g-C₃N₄ nanoparticles for efficient charge separation and increased photoelectrocatalytic degradation of phenol, *J. Hazard. Mater.* 344 (2018) 369–380.
- [48] J. Zhang, S. Fang, J. Mei, G. Zheng, X. Zheng, X. Guan, High-efficiency removal of rhodamine B dye in water using g-C₃N₄ and TiO₂ co-hybridized 3D graphene aerogel composites, *Sep. Purif. Technol.* 194 (2018) 96–103.
- [49] S. Yu, Y. Wang, F. Sun, R. Wang, Y. Zhou, Novel mpg-C₃N₄/TiO₂ nanocomposite photocatalytic membrane reactor for sulfamethoxazole photodegradation, *Chem. Eng. J.* 337 (2018) 183–192.
- [50] D. Jiang, T. Wang, Q. Xu, D. Li, S. Meng, M. Chen, Perovskite oxide ultrathin nanosheets/g-C₃N₄ 2D–2D heterojunction photocatalysts with significantly enhanced photocatalytic activity towards the photodegradation of tetracycline, *Appl. Catal. B: Environ.* 201 (2017) 617–628.
- [51] G. Zhang, T. Zhang, B. Li, S. Jiang, X. Zhang, L. Hai, X. Chen, W. Wu, An ingenious strategy of preparing TiO₂/g-C₃N₄ heterojunction photocatalyst: In situ growth of TiO₂ nanocrystals on g-C₃N₄ nanosheets via impregnation-calcination method, *Appl. Surf. Sci.* 433 (2018) 963–974.
- [52] M. Huang, J. Yu, Q. Hu, W. Su, M. Fan, B. Li, L. Dong, Preparation and enhanced photocatalytic activity of carbon nitride/titania(001 vs 101 facets)/reduced graphene oxide (g-C₃N₄/TiO₂/rGO) hybrids under visible light, *Appl. Surf. Sci.* 389 (2016) 1084–1093.
- [53] T. Giannakopoulou, I. Papailias, N. Todorova, N. Boukos, Y. Liu, J. Yu, C. Trapalis, Tailoring the energy band gap and edges' potentials of g-C₃N₄/TiO₂ composite photocatalysts for NOx removal, *Chem. Eng. J.* 310 (2017) 571–580.
- [54] A. Mishra, A. Mehta, S. Basu, Clay supported TiO₂ nanoparticles for photocatalytic degradation of environmental pollutants: a review, *J. Environ. Chem. Eng.* 6 (2018) 6088–6107.
- [55] Y. Sheng, Z. Wei, H. Miao, W. Yao, H. Li, Y. Zhu, Enhanced organic pollutant photodegradation via adsorption/photocatalysis synergy using a 3D g-C₃N₄/TiO₂ free-separation photocatalyst, *Chem. Eng. J.* 370 (2019) 287–294.
- [56] L. Hu, J. Yan, C. Wang, B. Chai, J. Li, Direct electrospinning method for the construction of Z-scheme TiO₂/g-C₃N₄/RGO ternary heterojunction photocatalysts with remarkably ameliorated photocatalytic performance, *Chin. J. Catal.* 40 (2019) 458–469.
- [57] L. Lu, G. Wang, M. Zou, J. Wang, J. Li, Effects of calcining temperature on formation of hierarchical TiO₂/g-C₃N₄ hybrids as an effective Z-scheme heterojunction photocatalyst, *Appl. Surf. Sci.* 441 (2018) 1012–1023.
- [58] R. Hao, G. Wang, H. Tang, L. Sun, C. Xu, D. Han, Template-free preparation of macro/mesoporous g-C₃N₄/TiO₂ heterojunction photocatalysts with enhanced visible light photocatalytic activity, *Appl. Catal. B: Environ.* 187 (2016) 47–58.



Fabrication of rGO and g-C₃N₄ co-modified TiO₂ nanotube arrays photoelectrodes with enhanced photocatalytic performance

Bin Zhang^{a,b,1}, Xiaohan Ma^{a,1}, Jun Ma^{a,b}, Yuanming Zhou^c, Guocheng Liu^a, Dong Ma^a, Zhihan Deng^d, Mingming Luo^e, Yanjun Xin^{a,*}

^a Qingdao Engineering Research Center for Rural Environment, College of Resource and Environment, Qingdao Agricultural University, Qingdao 266109, PR China

^b State Key Laboratory of Urban Water Resource and Environment, Harbin Institute of Technology, Harbin 150090, PR China

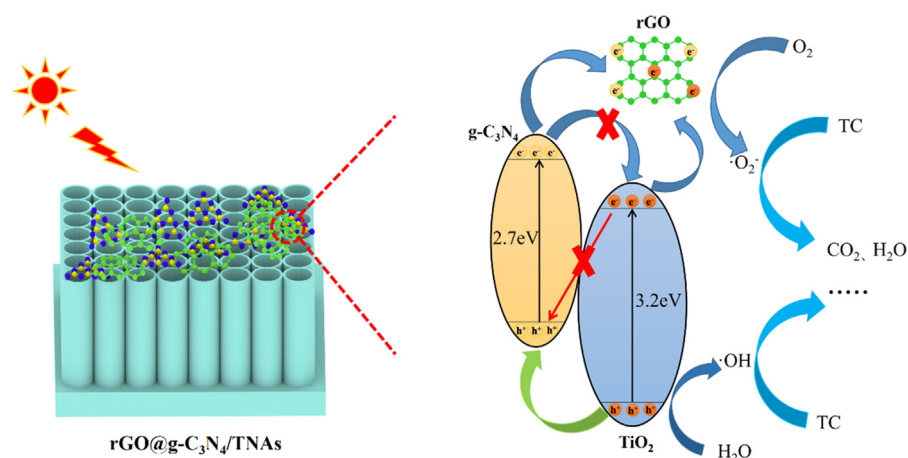
^c Central Laboratory, Qingdao Agricultural University, Qingdao 266109, PR China

^d Financial Department, Qingdao Agricultural University, Qingdao 266109, PR China

^e Construction Engineering College, Qingdao Agricultural University, Qingdao 266109, PR China

GRAPHICAL ABSTRACT

The photocatalytic activity of the 3D TiO₂ nanotube arrays photoelectrode was greatly improved by the modification of 2D reduced graphene oxide (rGO) and graphitic carbon nitride (g-C₃N₄). And the 3D rGO@g-C₃N₄/TNAs photoelectrode has excellent solar absorption capacity, photoelectric conversion performance and redox ability. Hydroxyl ($\cdot\text{OH}$) and superoxide ($\cdot\text{O}_2^-$) radicals were proved to be the main active species in photocatalytic degradation of TC by rGO@g-C₃N₄/TNAs photoelectrode.



ARTICLE INFO

Article history:

Received 7 March 2020

Revised 3 May 2020

Accepted 10 May 2020

Available online 22 May 2020

Keywords:

TiO₂ nanotube arrays

* Corresponding author.

E-mail address: xintom2000@126.com (Y. Xin).

¹ Bin Zhang and Xiaohan Ma contribute equally to the article.

ABSTRACT

To enhance the photocatalytic performance of titanium dioxide (TiO₂) and reduce the photocorrosion of graphitic carbon nitride (g-C₃N₄), two-dimensional (2D) reduced graphene oxide (rGO) and g-C₃N₄ co-modified three-dimensional (3D) TiO₂ nanotube arrays (rGO@g-C₃N₄/TNAs) photoelectrodes were fabricated by the combination of impregnation, annealing and electrochemical cathode deposition. The micro-morphology and microstructure were observed by SEM and TEM. The crystalline structure and element composition were characterized by XRD, XPS and Raman spectra. The optical and photo-electrochemical properties were analyzed by UV-vis DRS, open circuit potential and photocurrent density. Results

Graphitic carbon nitride
Reduced graphene oxide
Photoelectrodes
Photo-degradation

indicated that g-C₃N₄ and rGO were successfully loaded on the surface of the TNAs photoelectrodes and formed rGO@g-C₃N₄/TNAs heterostructure. The photocatalytic activity of the photoelectrodes was evaluated by the degradation rate of tetracycline hydrochloride (TC) under xenon lamp irradiation. The introduction of g-C₃N₄ and rGO reduced the band gap of TNAs photoelectrodes and promoted the separation of photo-induced electron-hole pairs. The rGO@g-C₃N₄/TNAs photoelectrodes exhibited higher photoelectrochemical properties and photocatalytic activity. The removal rate of TC by rGO@g-C₃N₄/TNAs photoelectrodes could reach 90% under 120 min photo-degradation and reaction kinetic constant was 2.38 times that of TNAs photoelectrodes. The active radicals capture and ESR experiments results showed that ·O₂⁻ radical and ·OH radical played the major role in photocatalytic degradation of TC. The possible photocatalytic mechanism of rGO@g-C₃N₄/TNAs photoelectrodes was presented.

© 2020 Elsevier Inc. All rights reserved.

1. Introduction

Recently, semiconductor-based photocatalysis technology has been extensively concerned owing to their excellent features for degradation of organic pollutants [1]. Titanium dioxide (TiO₂) semiconductor was regarded as a high-efficiency photocatalyst among various semiconductor materials (such as ZnO [2], CdS [3], SnO₂ [4], etc.) by reason that its abundance [5], inexpensive, non-toxicity [6], high chemical stability [7] and noncorrosive property [8]. However, the main defects of TiO₂ are the low use of sunlight owing to large band gap (~3.2 eV) as well as the low quantum production efficiency for high reintegration rate of photon-generated carriers, which significantly limits its practical applications [9]. To date, researchers have made a lot of research and efforts for further enhance the photocatalytic performance of TiO₂, including metals and non-metals doping [8], noble metal depositing [10], surface modification of carbon nanomaterials [9], dye-sensitization, semiconductor coupling [11,12], and so on [13–15]. Particularly, the semiconductor heterostructure constructed by coupling with narrower band gap semiconductors is considered a contributing approach to improve photocatalytic activity [11]. This unique heterostructure can broaden the light response region of TiO₂, and increase the separation efficiency of photogenic electron-hole pairs, thus prominently improve visible light photocatalytic performance [16–18].

Graphitic carbon nitride (g-C₃N₄), a fine two-dimensional (2D) non-metal semiconductor material, has attracted much attention due to narrower band gap (2.7 eV), low price, environmental friendliness, high chemical stability, corrosion resistance and high reduction potential [19–23]. At the same time, g-C₃N₄ has a strong ability to absorb visible light (380–460 nm). But g-C₃N₄ has a low oxidizability for organic pollutants owing to the low oxidation potential and high recombination rate of photon-generated carriers [24]. The construction of semiconductor heterogeneous structure between the TiO₂ and g-C₃N₄ might provide a high-efficiency approach to enhance the visible light photocatalytic property and redox capacity of pristine TiO₂ or g-C₃N₄ [25,26]. The conduction band (CB) of g-C₃N₄ (-1.10 eV vs NHE) is more negative than that of TiO₂ (-0.29 eV vs NHE) [27], which results in that the excited electrons on the CB of g-C₃N₄ could migrate to that of TiO₂ by means of contact with the heterojunction interface [21,28]. Therefore, the reintegration of photo-induced hole-electron pairs might be high-efficiency suppressed to enhance their separation efficiency, even the photocatalytic activity. However, in the process, some of the high-energy electrons will be lost as the electrons migrate from the CB of g-C₃N₄ to that of the TiO₂, thus leads to a reduction in reduction capacity of g-C₃N₄. Xiao et al. [29] has confirmed that g-C₃N₄/TiO₂ heterojunction photocatalyst was prepared via melt-infiltrating dicyandiamide and the photocatalytic degradation rate of Rhodamine B was improved. Other researchers also successfully prepared g-C₃N₄/TiO₂ photocatalysts

by hydrothermal method [30], in-situ thermal polymerization method [31], calcination method [32], solvent-free in situ method [33], thermal transformation methodology [34], pyrolysis process [35], dipping method [21], solid sublimation and transition method [36], and so on [25,37–40]. It is a pity that most of the reported g-C₃N₄/TiO₂ photocatalysts displayed lower utilization and difficult recycling due to the disordered structure and powder state. Fortunately, 2D g-C₃N₄ modified three-dimensional (3D) TiO₂ nanotube arrays [21,28,40] (g-C₃N₄/TNAs) photoelectrodes possess highly ordered structure, larger surface area [17] and higher photoelectric conversion ability [40]. However, g-C₃N₄/TNAs photoelectrodes were still instability for the lower electron transfer ability of g-C₃N₄ [41]. In particular, the electrons transfer between CB of g-C₃N₄ and TiO₂ reduces the reduction capacity of g-C₃N₄. Therefore, the electrons transfer capacity and redox ability of g-C₃N₄/TNAs photoelectrodes need to be further improved.

Graphene, a unique two-dimensional (2D) structure carbon materials, has a large specific surface area [42], superior electron transfer ability [27,43], high chemical stability, high transparency [44] and strong adsorption capacity [45]. The introduction of graphene might transfer the electrons quickly from g-C₃N₄ and TNAs photoelectrodes. As a result, the photocorrosion of g-C₃N₄ could be reduced and the stability of the photoelectrodes would be improved. Furthermore, the reduction ability of g-C₃N₄ is effectively retained due to the rapid electron transfer ability of graphene, which will contribute to the generation of active free radicals and promote photocatalytic activity. At the same time, tetracycline hydrochloride (TC), as a kind of antibiotic pollutants, has attracted great attention in the field of water treatment for its high solubility [46]. Due to high persistence and toxicity [47], TC is not only difficult to be biodegradable, but also can damage the aquatic environment and further threaten people health. Therefore, it is urgent to remove TC from contaminated water by an efficient and environmentally friendly way. To the best of our knowledge, the 2D rGO and g-C₃N₄ co-modified 3D TiO₂ nanotube arrays (rGO@g-C₃N₄/TNAs) photoelectrodes and its photocatalytic degradation performance of TC have not been reported.

In this paper, 3D rGO@g-C₃N₄/TNAs photoelectrodes was prepared through the combination of impregnation, annealing and electrochemical deposition. The morphology, crystal structure and elemental composition were studied systematically. To further study the influence of rGO on electrons transfer rate of g-C₃N₄/TNAs photoelectrode, the open circuit photo-generated potential and photocurrent density were further analyzed. The photocatalytic performance and stability of rGO@g-C₃N₄/TNAs photoelectrodes were assessed by the degradation of TC. On the basis of active radical scavenging and electron spin resonance (ESR) experiments, the possible degradation mechanism for 3D rGO@g-C₃N₄/TNAs photoelectrodes under simulated sunlight irradiation have also been proposed.

2. Experiments

2.1. Chemicals

Titanium (Ti) sheets (fineness > 99.8%) were supplied by Dongguan Tai Fu Metal Materials limited company (Co. LTD). TC (99.7%) was purchased from Shanghai Aladdin reagent Co. LTD. Other reagents were purchased as analytical pure without further treatment. All experiments were conducted using deionized water.

2.2. Fabrication of 3D rGO@g-C₃N₄/TNAs photoelectrodes

TiO₂ nanotube array photoelectrodes were synthesized through an anodization process according to our previous research [17,48] except that the reaction area was 40 mm × 10 mm.

The 3D g-C₃N₄/TNAs photoelectrodes were prepared by a simple dipping and calcining process. Firstly, the melamine solution of 20,000 mg/L was prepared as solvent with ethylene glycol. Secondly, the TNAs photoelectrodes were dipped in melamine solution with stirring for 10 min and afterwards the glycol on the TNAs photoelectrodes were evaporated in muffle furnace at 210 °C under nitrogen atmosphere. Then, repeated the above steps four times. Thirdly, the g-C₃N₄/TNAs photoelectrodes were obtained by annealing in tube furnace at 500 °C and maintain two hours under nitrogen atmosphere. The rGO@g-C₃N₄/TNAs photoelectrodes were prepared by cathodic electrodeposition. The g-C₃N₄/TNAs photoelectrodes were used as cathode and Pt sheet as the anode. The deposition was in the solution of 50 mg/L graphene oxide at glass reactor. In detail, graphene oxide was prepared on the basis of the improved Hummers method [43,49]. The 3D rGO@g-C₃N₄/TNAs photoelectrodes were obtained after an electrochemical cathode deposition process. The applied deposition voltage was 2.5 V, and the deposition process was maintained for 3 min. Finally, the rGO@g-C₃N₄/TNAs photoelectrodes were evaporated through vacuum drying oven at 105 °C.

2.3. Photoelectrodes characterization

The micromorphology and microstructure of the as-prepared samples were investigated by cold field launch scanning electron microscope (SEM, Hitachi S-4800) and field emission transmission electron microscope (TEM, Tecnai G2 F20). The crystalline structure was characterized via X-ray diffractometer (XRD, D8 ADVANCE, Bruker AXS) with Cu K α radiation ($\lambda = 0.15418$ nm). The composition and structure of the substance were analyzed using Raman spectrometer (DXR Raman Microscope). Spectrometer: DXR Raman Microscope. The detailed test parameters of Raman were as follows: Laser: 532 nm; Laser power level: 6 mW; Exposure time: 1.00 sec; Number of exposure: 20. In order to measure the basic element composition of photoelectrodes film, X-ray photoelectron spectroscopy (XPS) was analyzed through Multifunctional imaging electron spectrometer (Thermo ESCALAB 250Xi) using an Al-K α X-ray (1486.6 eV) source. UV–Vis diffuse reflectance spectra were acquired by a UV–Vis spectrophotometer (TU-1901, Beijing). The photo-electrochemical properties of as-prepared photoelectrodes were measured using an electrochemical workstation (LK2010, LANLIKE). Specifically, 0.1 M Na₂SO₄ was serve as an electrolyte solution for the three-electrode operating system. The as-prepared photoelectrodes and Platinum plate were used as the working electrode and counter electrode, respectively. The saturated calomel electrode was used as the reference electrode. The active radicals adducts were determined by ESR technique (ELEXSYS-II E560, BRUKER) with DMPO as trapping agent. Particularly, ·OH and ·O₂⁻ radicals were determined by using deionized water and methanol as solvent, respectively.

2.4. Measurement of photocatalytic activity

The photocatalytic activity of the photoelectrodes was evaluated by the degradation rate of TC under xenon lamp irradiation. The newly prepared photoelectrode was placed vertically in a quartz reactor containing 40 mL TC solution (20 mg/L) with magnetic stirring. The distance between the photoelectrode and xenon lamp (150 W) was at 2 cm. The concentration of TC was measured by Waters 1525 HPLC equipped with a Waters Symmetry C18 column (4.6 × 150 mm, 5 μ m particle size) at every 20 min intervals. The mobile phase was 40% methanol and 60% acetic acid (0.1%) with a flow rate of 1.0 mL/min, and the absorption wavelength was controlled at 356 nm.

The removal rate of TC was calculated according to the following equation:

$$\text{Removal (\%)} = [(C_0 - C)/C_0] \times 100$$

where C₀ was the initial concentration of TC before irradiation; C was the concentration of TC after irradiation for *t* min.

3. Results and discussions

3.1. SEM and TEM analysis

The micromorphology and microstructure of various photoelectrodes were investigated by SEM and TEM (Fig. 1). The ordered 3D nanotube arrays with a diameter of about 90 nm grown on the substrate of photoelectrodes and the average wall thickness of nanotubes was approximately 25 nm. It could be clearly observed that floccules were deposited on the top of the nanotubes (Fig. 1b) after loading the 2D g-C₃N₄ particles. For 3D rGO@g-C₃N₄/TNAs photoelectrodes, some transparent irregularity film covered the nanotubes (Fig. 1c), which indicated that 2D g-C₃N₄ and rGO were successfully loaded on 3D TNAs photoelectrodes. As shown in Fig. 1d, TiO₂ was tightly bound to g-C₃N₄ sheets in transparent thin layers of graphene. The HR-TEM image of rGO@g-C₃N₄/TNAs photoelectrode (Fig. 1e) clearly revealed the formation of composite heterogeneous interfaces of rGO, g-C₃N₄ and TiO₂, and the lattice spacing of anatase TiO₂ crystal plane (1 0 1) and g-C₃N₄ crystal plane (0 0 2) were 0.35 nm and 0.33 nm [50], respectively. At the same time, the selected-area diffraction rings (Fig. 1f) confirmed the polycrystalline structure of the 3D rGO@g-C₃N₄/TNAs photoelectrode. The EDX spectra of rGO@g-C₃N₄/TNAs photoelectrodes was shown in Fig. 1g. Obviously, the characteristic peaks of Ti, O, C and N elements were observed in rGO@g-C₃N₄/TNAs photoelectrodes, where N elements came from g-C₃N₄ and C elements might come from rGO or g-C₃N₄. According to the above results, it could be determined that g-C₃N₄ and rGO were successfully loaded on TNAs photoelectrodes.

3.2. XRD and Raman characterization

The crystalline structure of the TNAs, g-C₃N₄/TNAs and rGO@g-C₃N₄/TNAs photoelectrodes were investigated by XRD and Raman spectra. Fig. 2a showed that diffraction peaks of anatase TiO₂ (JCPDSNO. 21-1272) and Ti (JCPDSNO. 65-3362) metal phase appeared in all photoelectrodes, which were marked with triangle and dot. According to the Scherrer's formula, TiO₂ lattice size of all the above mentioned photoelectrodes were approximately 37 nm, which showed that the introduction of g-C₃N₄ and rGO has no significant change on the crystalline structure of TiO₂. Similarly, the average crystal sizes of g-C₃N₄ was calculated as 23 nm. The peaks at 12.2° and 27.5° were identified as (1 0 0) and (0 0 2) crystal plane of g-C₃N₄ (JCPDS 87-1526), respectively. And the sharp characteristic peak at 27.5° represented the interlayer stacking of the

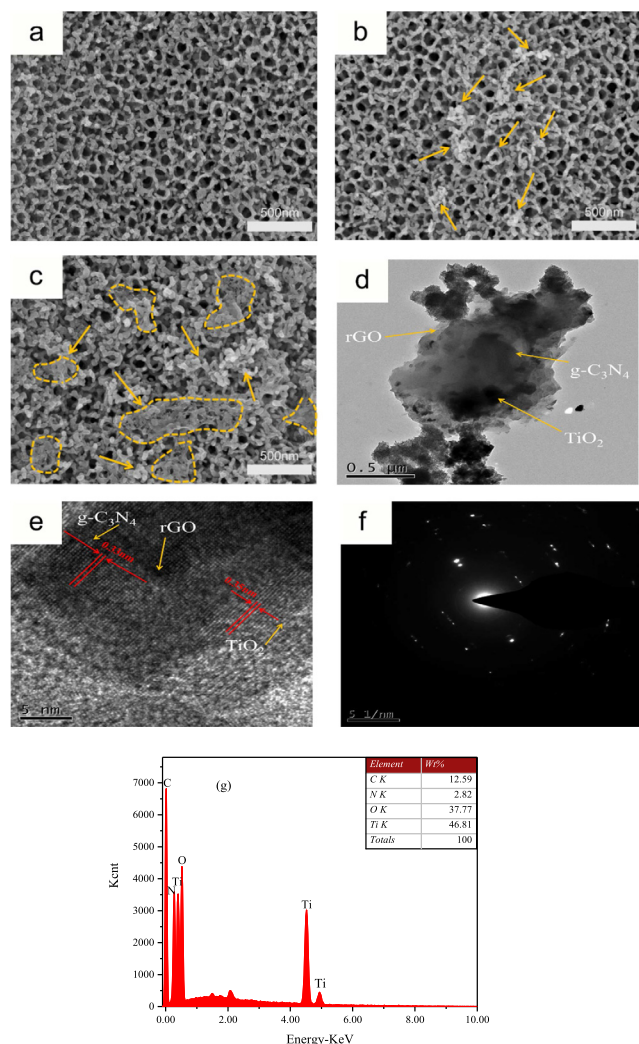


Fig. 1. SEM images of TNAs (a), $g\text{-C}_3\text{N}_4/\text{TNAs}$ (b), $\text{rGO}@g\text{-C}_3\text{N}_4/\text{TNAs}$ (c) photoelectrodes; TEM image of $\text{rGO}@g\text{-C}_3\text{N}_4/\text{TNAs}$ (d) photoelectrodes; HR-TEM image of $\text{rGO}@g\text{-C}_3\text{N}_4/\text{TNAs}$ (e); Selected-area electron diffraction rings of $\text{rGO}@g\text{-C}_3\text{N}_4/\text{TNAs}$ (f) photoelectrodes; EDX spectrum of $\text{rGO}@g\text{-C}_3\text{N}_4/\text{TNAs}$ (g) photoelectrodes.

conjugated aromatic system, and the distance was 0.325 nm according to the Bragg equation, which was in accordance with the reported literature [32]. Compared to the TNAs photoelectrodes, the characteristic diffraction peak at 27.5° for $g\text{-C}_3\text{N}_4/\text{TNAs}$ and $\text{rGO}@g\text{-C}_3\text{N}_4/\text{TNAs}$ photoelectrodes, indicated that $g\text{-C}_3\text{N}_4$ has been successfully loaded on the TNAs photoelectrodes. However, no obvious characteristic peak of rGO was found in $\text{rGO}@g\text{-C}_3\text{N}_4/\text{TNAs}$ photoelectrodes, which should be caused by the lower content [42] and high dispersity of rGO on the surface [51].

Fig. 2b showed the Raman spectra of TNAs, $g\text{-C}_3\text{N}_4/\text{TNAs}$ and $\text{rGO}@g\text{-C}_3\text{N}_4/\text{TNAs}$ photoelectrodes including the characteristic D and G bands. For all photoelectrodes, the major Raman bands of TiO_2 anatase phase appeared at 145, 198, 398, 516, 636 cm^{-1} [17]. It was clear that there was no significant change in the crystals structure of TNAs after the deposition of $g\text{-C}_3\text{N}_4$ and rGO. For the Raman spectrum of $\text{rGO}@g\text{-C}_3\text{N}_4/\text{TNAs}$ photoelectrodes, two obvious characteristic peaks appeared at around 1348 and 1597 cm^{-1} , which is related to the D and G bands of rGO, respectively. And the D and G band represent the existence of defects of sp^3 hybridized carbon atoms and in-plane stretching vibration of carbon atom sp^2 hybridized, respectively [52,53]. Therefore, it could be further proved that rGO has been successfully deposited on the film of the photoelectrodes. In addition, no typical charac-

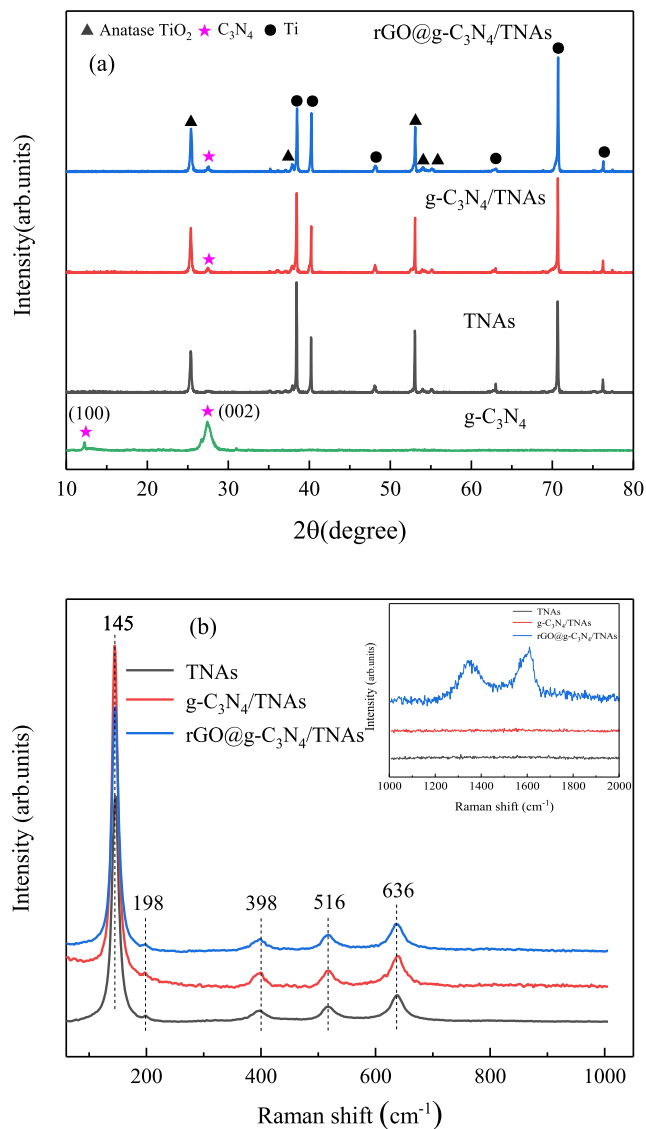


Fig. 2. XRD spectra (a) and Raman spectra (b) of TNAs, $g\text{-C}_3\text{N}_4/\text{TNAs}$, $\text{rGO}@g\text{-C}_3\text{N}_4/\text{TNAs}$ photoelectrodes.

teristic peak of $g\text{-C}_3\text{N}_4$ was discovered in $g\text{-C}_3\text{N}_4/\text{TNAs}$ and $\text{rGO}@g\text{-C}_3\text{N}_4/\text{TNAs}$ photoelectrodes. And the result might be caused by a lower $g\text{-C}_3\text{N}_4$ content and the weak response of $g\text{-C}_3\text{N}_4$ to Raman absorbance [53–55]. The results of XRD and Raman spectrum indicated that $g\text{-C}_3\text{N}_4$ and rGO has been successfully loaded on the surface of TNAs, which confirmed the results of SEM and TEM (Fig. 1).

3.3. XPS analysis

The XPS survey spectrum of $\text{rGO}@g\text{-C}_3\text{N}_4/\text{TNAs}$ photoelectrodes and high-resolution XPS spectra of Ti 2p, C 1s, O 1s, N 1s were shown in Fig. 3. The photoelectrodes film mainly contained four elements of Ti, C, O and N (Fig. 3a). Fig. 3b revealed that two peaks appeared in the binding energy of 458.6 and 464.4 eV corresponding to Ti 2p_{3/2} and Ti 2p_{1/2}, respectively. Meanwhile, the separation distance was 5.8 eV between Ti 2p_{3/2} and Ti 2p_{1/2}, which was consistent with the binding energy of Ti^{4+} in TiO_2 [56,57]. The high-resolution XPS spectrum of C 1s was shown in Fig. 3c, the sharp C1s peak centered at 284.7 eV corresponding to the C=C, C–H, and sp^2 hybridized carbon atoms (C–C) in rGO [42,58]. The other two

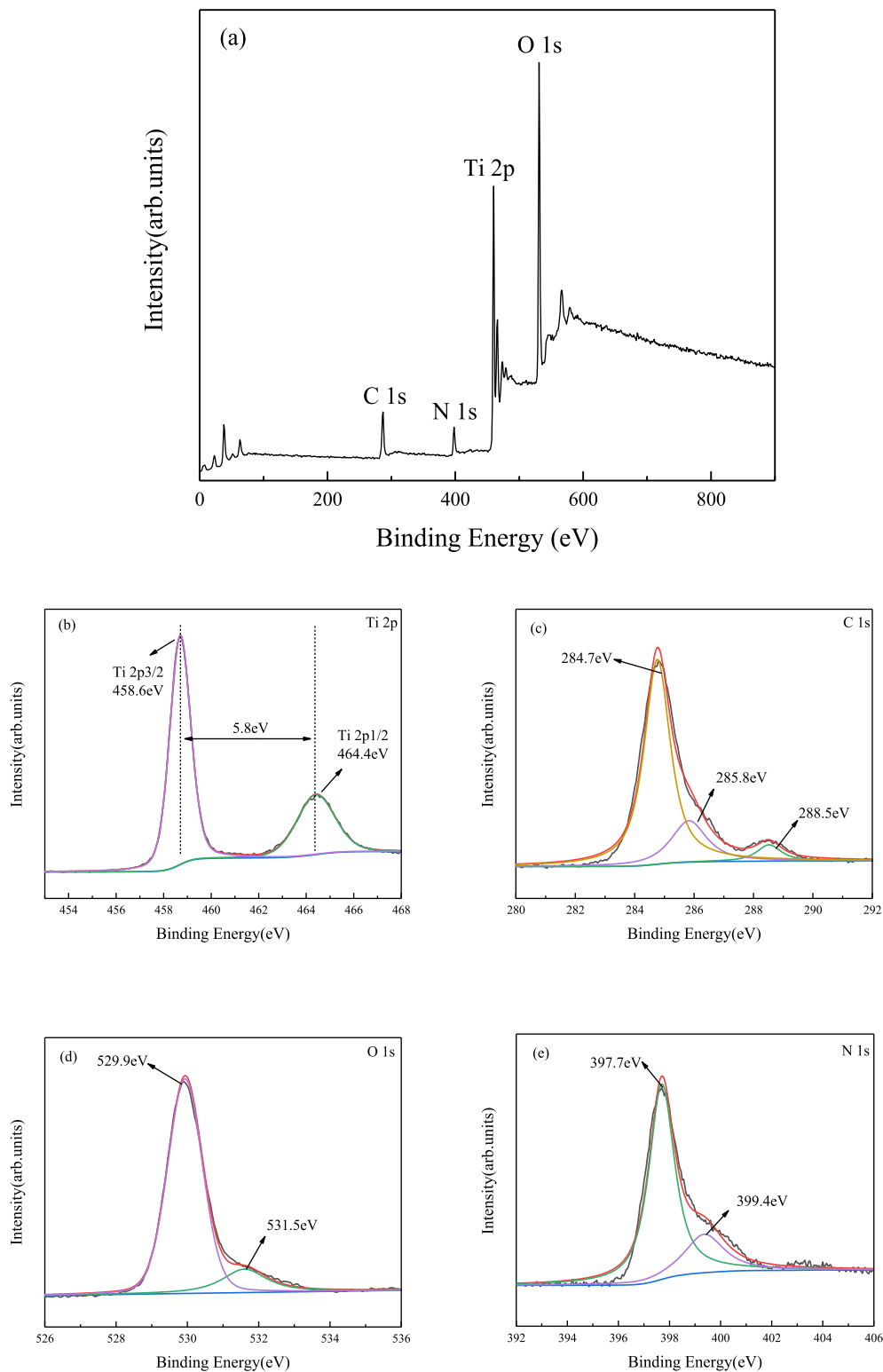


Fig. 3. XPS survey spectrum of rGO@g-C₃N₄/TNAs (a) photoelectrodes; High-resolution XPS spectra of (b) Ti 2p, (c) C 1s, (d) O 1s and (e) N 1s.

peaks of C 1s centered at 285.8 and 288.5 eV were regarded as the C=N (sp²) and C–N (sp³) or C–(N)₃ groups, respectively [24,59]. As shown in Fig. 3d, the O 1s peaks appeared at 529.9 and 531.5 eV were identified as the Ti–O bond and surface –OH groups [40]. The high-resolution XPS spectrum of N 1s was separated into two weaker peaks (Fig. 4e) at 397.7 eV and 399.4 eV, which could be attributed to sp² hybridized nitrogen in triazine rings (C=N–C) and tertiary nitrogen(N–(C)₃) [18,25,41], respectively. According

to this XPS results, as well as XRD and Roman, g-C₃N₄ and rGO have been successfully combined with TNAs.

3.4. UV–vis characterization

UV–vis diffuse reflectance spectra (DRS) play a significant impact in measuring the light absorption performance of the photoelectrode [17]. The DRS and band gap of the as-prepared

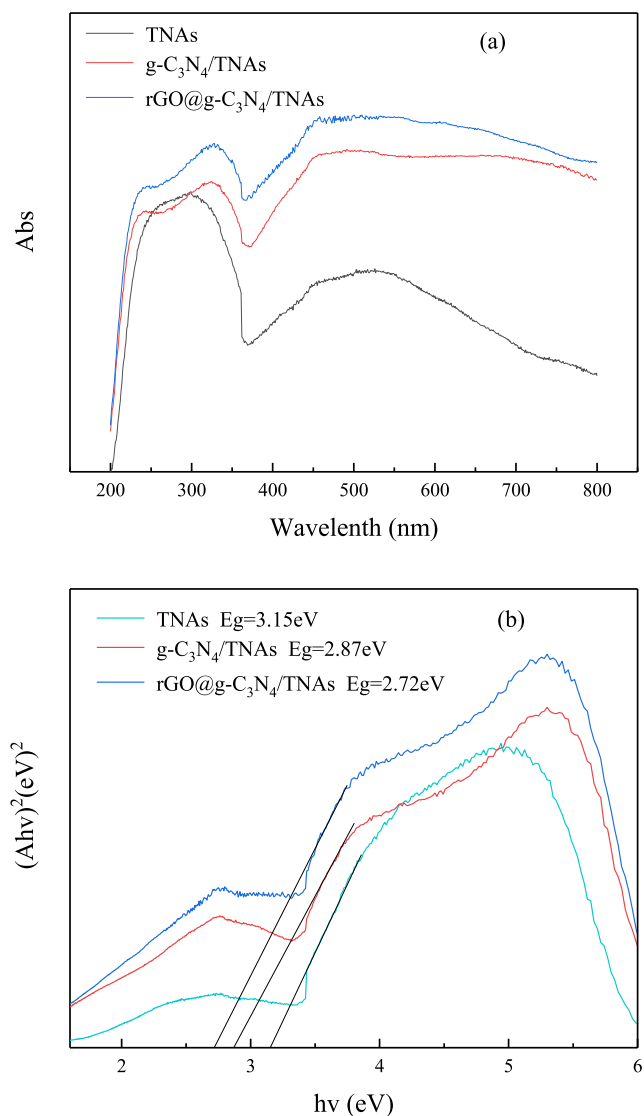


Fig. 4. UV-vis absorption spectra (a) $(Ah\nu)^2 \sim hv$ curves (b) of TNAs, g-C₃N₄/TNAs, rGO@g-C₃N₄/TNAs photoelectrodes.

photoelectrodes were analyzed and shown in Fig. 4. It is apparent that optical absorption property of rGO@g-C₃N₄/TNAs photoelectrodes has been greatly enhanced in visible light region (>390 nm) compared with the TNAs photoelectrodes. The results indicated that g-C₃N₄ and rGO significantly promoted the light absorption of TNAs. Based on the Kubelka-Munk function Eq. [18]:

$$(\alpha h\nu)^2 = A(h\nu - E_g)$$

where α , $h\nu$, E_g and A were absorption coefficient, photon energy, band gap and a proportionality constant, respectively. At the same time, the $(Ah\nu)^2$ versus $h\nu$ curves of samples were presented in Fig. 4b. According to the results, the band gaps of TNAs, g-C₃N₄/TNAs, rGO@g-C₃N₄/TNAs photoelectrodes were 3.15 eV, 2.87 eV and 2.72 eV, respectively, which indicated that the longer waves would be absorbed for the introduction of g-C₃N₄ or rGO. As a result, the red shift of the light absorption wavelength and increased absorption property, which could provide probable conditions for the improved visible light photocatalytic activity of the composite photoelectrodes.

3.5. Photo-electrochemical properties

To in-depth investigate the separation efficiency of photon-generated carriers, the open circuit potential and photo-generated current of all photoelectrodes were measured. As shown in Fig. 5a, the open circuit potential sharply increased for the accumulation of photoelectrons when light was on and gradually decreased once the light was off for the accumulated photoelectrons transferred to the solution or recombined with photoholes. The open circuit potential of rGO@g-C₃N₄/TNAs photoelectrode was the highest (~0.20 V), which was 1.25-fold that of TNAs photoelectrode (~0.16 V) and 1.1-fold that of g-C₃N₄/TNAs photoelectrode (~0.18 V). Based on the UV-vis diffuse reflectance spectra (Fig. 4), rGO@g-C₃N₄/TNAs photoelectrodes could produce more photo-induced electrons owing to the greatly enhanced light absorption ability of TNAs photoelectrode. Meanwhile, the separation efficiency of photo-generated carriers was greatly improved due to excellent electrons transfer ability of rGO [27]. Thus, rGO@g-C₃N₄/TNAs photoelectrodes revealed a higher potential. For TNAs photoelectrodes, the open circuit potential rose rapidly, which suggested that the ordered 3D nanotube structure of TNAs photoelectrodes could transfer electrons quickly [48]. For g-C₃N₄/TNAs photoelectrodes, the open circuit potential was significantly

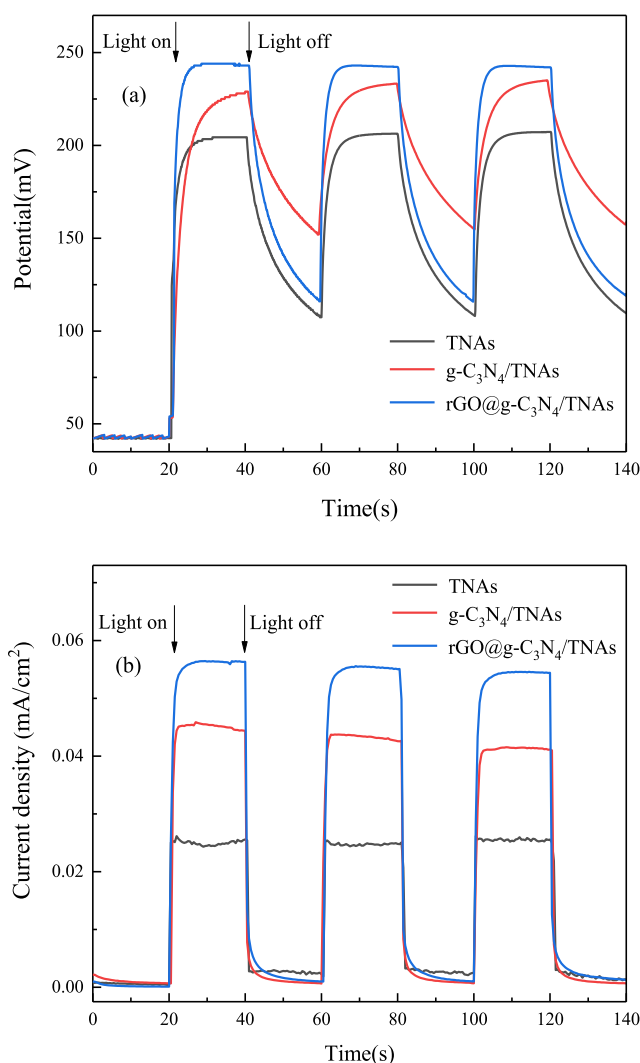


Fig. 5. Open circuit potential (a) and Photocurrent density (b) of TNAs, g-C₃N₄/TNAs, rGO@g-C₃N₄/TNAs photoelectrodes.

enhanced compared with that of TNAs photoelectrodes, which might be attributed to the reason that the enhancement of light absorption capacity (Fig. 4) could lead to the increase of photo-induced electrons. However, it could be apparently seen that the open circuit potential of $g\text{-C}_3\text{N}_4/\text{TNAs}$ photoelectrodes increased slower than that of TNAs and $r\text{GO}@g\text{-C}_3\text{N}_4/\text{TNAs}$ photoelectrodes, and the hysteretic effect was shown [42,48]. For $r\text{GO}@g\text{-C}_3\text{N}_4/\text{TNAs}$ photoelectrodes, the open circuit potential increased rapidly and hysteresis effect was reduced. It can be seen from the above results that only the open circuit potential of $g\text{-C}_3\text{N}_4/\text{TNAs}$ photoelectrodes has obvious hysteresis effect, which might be interpreted by the following reasons: (1) For the TNAs photoelectrodes, under the illumination of xenon light, the generated carriers was smaller and the ordered nanotube array is sufficient to transfer rapidly the electrons. Thus hysteresis effect is very difficult to appear. (2) However, as $g\text{-C}_3\text{N}_4/\text{TNAs}$ photoelectrodes, a large electrons could be generated with the illumination, which could not transfer quickly for the weak electron transfer ability of $g\text{-C}_3\text{N}_4$. Furthermore, the transfer ability of nanotube arrays is also difficult to meet the requirements of transferring quickly the increased electrons. Thus the hysteretic effect was shown. (3) And the introduction of rGO could efficiently and quickly transfer the increasing electrons, thus the hysteresis effect was reduced. Furthermore, the ultra-fast electron transfer capability of rGO promote the separation of photo-induced electrons and holes, and thus $r\text{GO}/g\text{-C}_3\text{N}_4/\text{TNAs}$ photoelectrodes were able to quickly reach a higher open circuit potential.

Similarly, when the light source was removed, the open circuit potential of $g\text{-C}_3\text{N}_4/\text{TNAs}$ photoelectrodes decreased slower than that of TNAs and $r\text{GO}@g\text{-C}_3\text{N}_4/\text{TNAs}$ photoelectrodes due to the hysteresis effect. In addition, the recombination rate of photo-induced holes and electrons was regarded as an important factor of photocurrent density [17]. As shown in Fig. 5b, the photocurrent increased or decreased rapidly when the light was on or off, which indicated that all the photoelectrodes were extremely sensitive to illumination. The photocurrent density of the TNAs, $g\text{-C}_3\text{N}_4/\text{TNAs}$, $r\text{GO}@g\text{-C}_3\text{N}_4/\text{TNAs}$ photoelectrode were 0.024 mA cm^{-2} , 0.045 mA cm^{-2} and 0.056 mA cm^{-2} , respectively, which indicated that the separation efficiency of photon-generated carrier were improved obviously after decorated $g\text{-C}_3\text{N}_4$ and rGO. Meanwhile, it was obvious that the photocurrent density curve of the $r\text{GO}@g\text{-C}_3\text{N}_4/\text{TNAs}$ photoelectrode was smoother than TNA photoelectrode, which could be attributed to excellent stability of $r\text{GO}@g\text{-C}_3\text{N}_4/\text{TNAs}$ photoelectrode. According to the above results, $r\text{GO}@g\text{-C}_3\text{N}_4/\text{TNAs}$ photoelectrode exhibited superior photoelectrochemical properties.

3.6. Photocatalytic performance

The photocatalytic performance of $r\text{GO}@g\text{-C}_3\text{N}_4/\text{TNAs}$ photoelectrodes was further investigated by photocatalytic removal rates of TC. As shown in Fig. 6a, after 120 min photodegradation, the removal rates of TC by TNAs, $g\text{-C}_3\text{N}_4/\text{TNAs}$ and $r\text{GO}@g\text{-C}_3\text{N}_4/\text{TNAs}$ photoelectrodes were 61.28%, 78.36% and 90.23%, respectively.

The results indicated that $r\text{GO}@g\text{-C}_3\text{N}_4/\text{TNAs}$ photoelectrodes have a much higher photocatalytic performance than TNAs (about 1.47 times). As shown in Fig. 6b, the removal of TC could be described by pseudo first-order reaction kinetic equation as follows:

$$\ln(C_0/C) = kt$$

where C_0 was the initial concentration of TC, C was the concentration of TC after irradiation for t min, and the k is the pseudo first-order rate constant. For $r\text{GO}@g\text{-C}_3\text{N}_4/\text{TNAs}$ photoelectrodes, the k was 0.019 min^{-1} , which was 1.58 and 2.38 times that of $g\text{-C}_3\text{N}_4/$

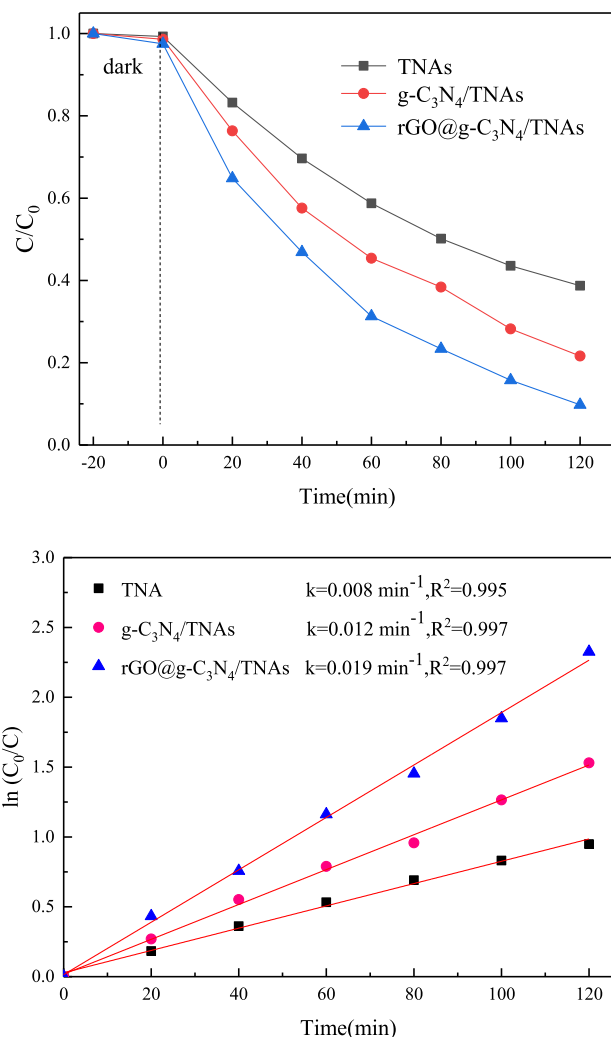


Fig. 6. Photocatalytic removal rates of TC (a) and pseudo first-order kinetics fitting curves (b) of over TNAs, $g\text{-C}_3\text{N}_4/\text{TNAs}$, $r\text{GO}@g\text{-C}_3\text{N}_4/\text{TNAs}$ photoelectrodes.

TNAs and TNAs photoelectrodes, respectively. The results shown that $r\text{GO}@g\text{-C}_3\text{N}_4/\text{TNAs}$ photoelectrodes revealed the highest photocatalytic performance, which were attributed to the enhancement of light absorption performance (Fig. 4) and higher electron mobility (Fig. 5) due to the decoration of $g\text{-C}_3\text{N}_4$ and rGO. In addition, the stability of the $r\text{GO}@g\text{-C}_3\text{N}_4/\text{TNAs}$ photoelectrodes were investigated (Fig. 7). It could be obviously seen that the removal rate of TC, which decreased by less than 4% after five cycles, was still higher than 87%. The results showed $r\text{GO}@g\text{-C}_3\text{N}_4/\text{TNAs}$ photoelectrodes possessed superior stability, which could be ascribed to the rapid electron transfer capability of rGO, and thus inhibit the photocorrosion of $g\text{-C}_3\text{N}_4$. In addition, it also could be ascribed to the formation of more stable semiconductor coupling structures because rGO strengthen the close contact between $g\text{-C}_3\text{N}_4$ and TNAs photoelectrodes [58].

3.7. Photocatalytic mechanism

In general, active radicals play the decisive role in photocatalytic degradation of pollutants. To further explore the photocatalytic degradation mechanism of $r\text{GO}@g\text{-C}_3\text{N}_4/\text{TNAs}$ photoelectrodes for TC, the active radical capture experiment was performed. As demonstrated in Fig. 8, the photocatalytic removal rates of TC were inhibited by 37.28%, 21.67%, and 8.83%, in the

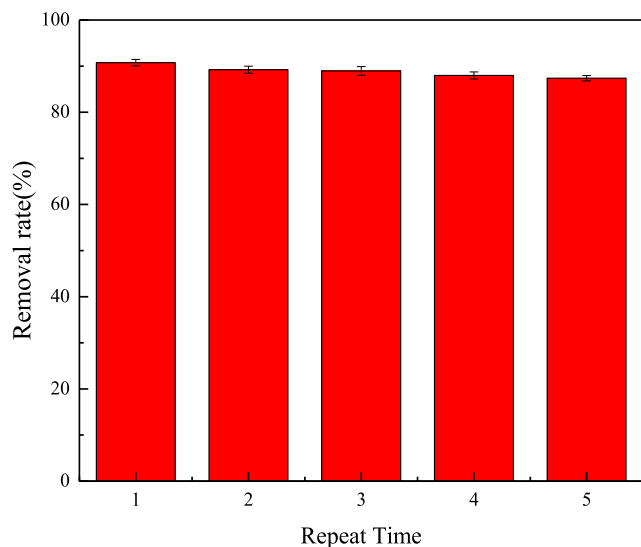


Fig. 7. Photocatalytic removal rates of TC by rGO@g-C₃N₄/TNAs photoelectrodes for five run cycles.

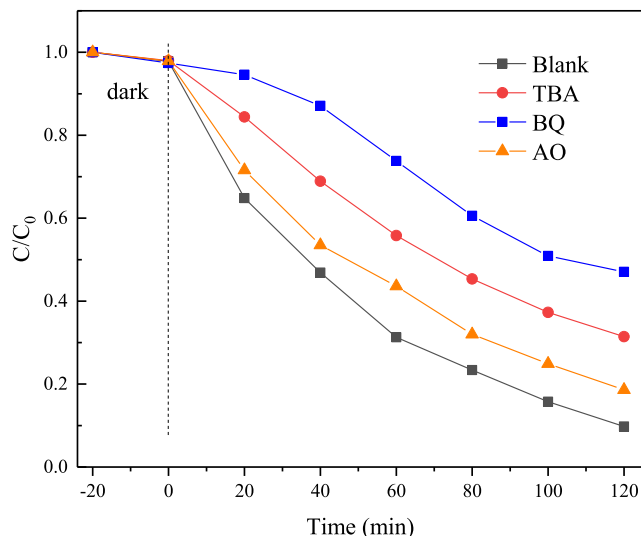


Fig. 8. Photocatalytic removal rates of TC by rGO@g-C₃N₄/TNAs photoelectrodes in the presence of radical scavenger.

presence of BQ (scavengers of $\cdot\text{O}_2^-$), TBA (scavengers of $\cdot\text{OH}$) and AO (scavengers of h^+), respectively. Notably, the order of contribution rates of active free radicals in photocatalytic degradation was as follows: $\cdot\text{O}_2^- > \cdot\text{OH} > h^+$, which further revealed that $\cdot\text{O}_2^-$ and $\cdot\text{OH}$ play a dominant role in photocatalytic degradation of TC by rGO@g-C₃N₄/TNAs photoelectrodes.

The spin-trapping ESR techniques was used to further detect $\cdot\text{O}_2^-$ and $\cdot\text{OH}$ radicals generated during photocatalytic degradation on rGO@g-C₃N₄/TNAs photoelectrodes. As displayed in Fig. 9, four peaks with a peak intensity ratio of 1:2:2:1 were present in the case of the rGO@g-C₃N₄/TNAs photoelectrodes illuminated by xenon lamps, which indicated that significant $\cdot\text{OH}$ were produced in the process of photocatalysis. At the same time, the peaks of $\cdot\text{O}_2^-$ radicals adders (DMPO- $\cdot\text{O}_2^-$) also appear in the ESR spectra. Obviously, the peak strength of DMPO- $\cdot\text{O}_2^-$ was significantly higher than that of DMPO- $\cdot\text{OH}$, which indicated that the concentration of $\cdot\text{O}_2^-$ radicals generated in the photocatalytic process was higher than that of $\cdot\text{OH}$ radicals. The ESR results were consistent with the radicals scavenging experiment.

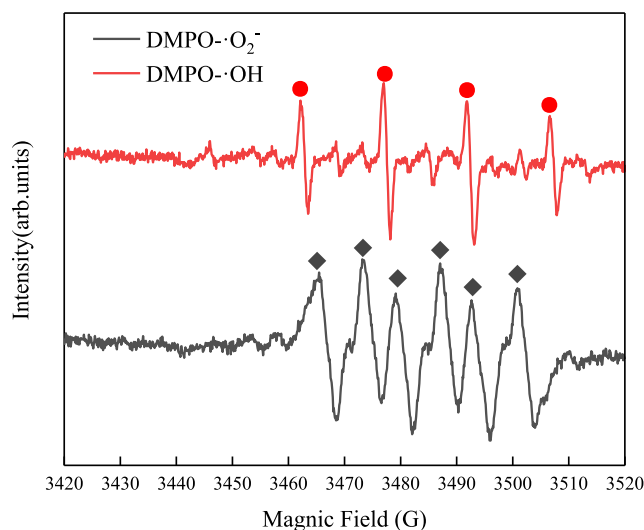


Fig. 9. ESR spectra of DMPO- $\cdot\text{OH}$ and DMPO- $\cdot\text{O}_2^-$ adducts of rGO@g-C₃N₄/TNAs photoelectrodes under xenon lamp irradiation.

On the basis of the above mentioned consequence, the possible mechanisms for photocatalytic degradation of TC over as-prepared photoelectrodes under simulated sunlight irradiation were proposed in Fig. 10. According to previous reports, the CB and valence band (VB) potentials of TiO₂ are -0.29 eV vs NHE and 2.91 eV vs NHE [42,60], respectively. And the CB and VB potentials of g-C₃N₄ are -1.10 eV vs NHE and 1.60 eV vs NHE [27], respectively. Thus, both electrons in CB of TiO₂ and g-C₃N₄ possess the ability to create superoxide ($\cdot\text{O}_2^-$) radicals because the potential is negative enough ($E^0(\text{O}_2/\cdot\text{O}_2^-) = -0.046$ eV) [18,27,61]. At the same time, for pristine TiO₂, the hole oxidation capacity of VB is sufficient to generate hydroxyl ($\cdot\text{OH}$) radical because the potential of VB is higher than $E^0(\text{OH}^-/\cdot\text{OH}) = 1.99$ eV and $E^0(\cdot\text{OH}/\text{H}_2\text{O}) = 2.68$ eV, while g-C₃N₄ is not sufficient to produce $\cdot\text{OH}$ due to the weak oxidation potential of the CB. Fig. 10a showed that TNAs photoelectrodes possessed higher photo-generated hole-electrons recombination rate and lower solar light absorption capacity (Fig. 4) for the wide band gap of 3.2 eV. Thus, the degradation efficiency of TC by pristine TNAs photoelectrode was the lowest (Fig. 6). For g-C₃N₄/TNAs photoelectrodes, both g-C₃N₄ and TNAs could be excited and g-C₃N₄ could absorb the visible light, thus much more photo-generated electrons and holes could appear in their CB and VB. Some of the holes in the VB of TiO₂ could migrate to that of the g-C₃N₄ because the VB of TiO₂ is more positive than that of g-C₃N₄. Similarly, some electrons in the CB of g-C₃N₄ could be transferred to that of TiO₂ for the CB of g-C₃N₄ is more negative. The result will result in the loss of high-energy electrons in CB of g-C₃N₄, reducing the formation rate of $\cdot\text{O}_2^-$. The accumulated electrons on the CB of TiO₂ would react with O₂ to form $\cdot\text{O}_2^-$ and the accumulated holes on the VB of TiO₂ would react with H₂O to generate $\cdot\text{OH}$ [26]. Meanwhile, some photo-generated electrons might also transfer to the VB of g-C₃N₄ and recombine with the accumulated holes on the VB of g-C₃N₄ (Fig. 10b). Furthermore, the photocorrosion of g-C₃N₄ will be reduced for the fast electrons transfer rate. It is known that radicals such as $\cdot\text{OH}$ and $\cdot\text{O}_2^-$ undertake the crucial tasks during the photocatalytic degradation system [40]. For rGO@g-C₃N₄/TNAs photoelectrodes, the generated electrons in the CB of g-C₃N₄ would be quickly transferred to rGO instead of CB of TiO₂. The transferred electrons could be captured by O₂ and produce $\cdot\text{O}_2^-$ (Fig. 10c), which will effectively avoid the loss of high-energy electrons and the photocorrosion of g-C₃N₄. Thus, the high reduction properties of g-C₃N₄ were preserved, which will

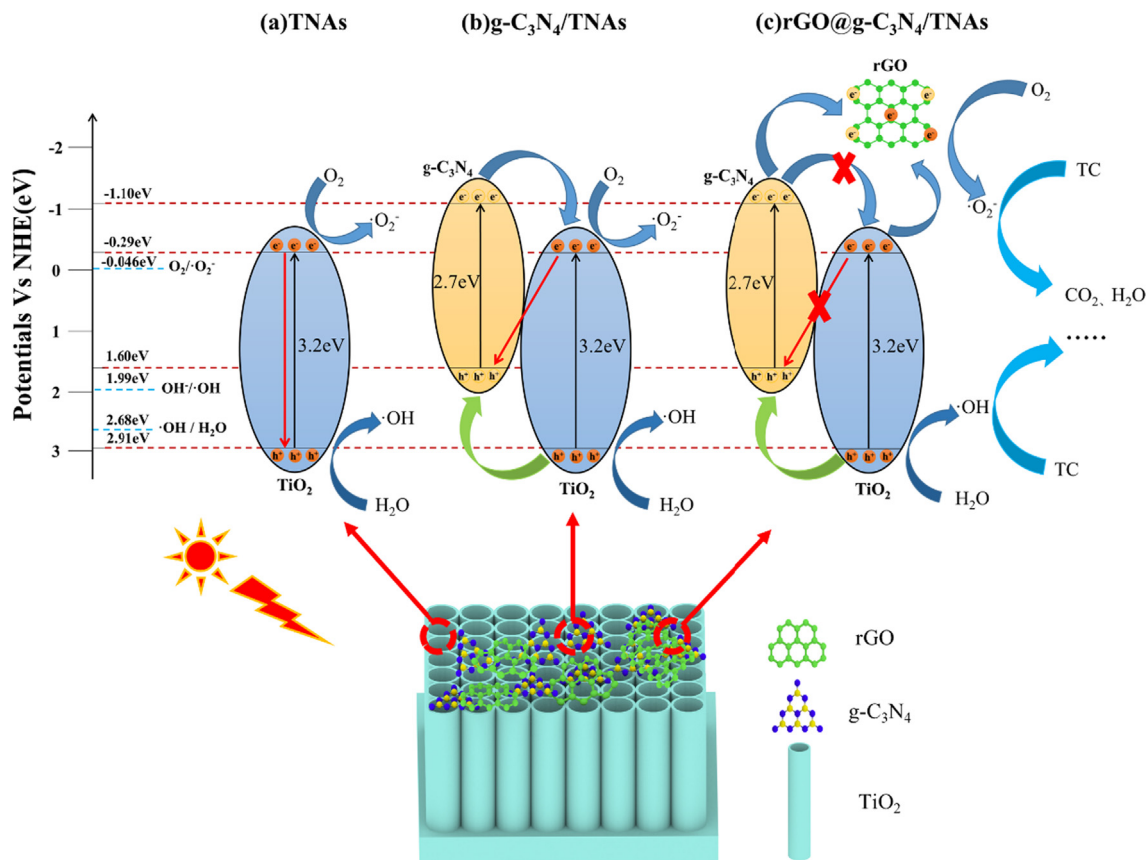


Fig. 10. Schematic diagrams for photocatalytic mechanism of (a) TNAs, (b) $g\text{-C}_3\text{N}_4/\text{TNAs}$ and (c) $\text{rGO}@g\text{-C}_3\text{N}_4/\text{TNAs}$ photoelectrodes.

be more favorable to the formation of $\cdot\text{O}_2^-$ radicals. Besides, the electrons in the CB of TiO_2 will also be transferred by rGO rather than recombined with photo-generated holes in the VB of $g\text{-C}_3\text{N}_4$. Hence, the reintegration of photo-generated electrons and holes (as-mentioned in Fig. 10b) could be effectively inhibited or hysteresis to prolong the life of photo-generated holes. Finally, $\text{rGO}@g\text{-C}_3\text{N}_4/\text{TNAs}$ photoelectrodes exerted the superior photocatalytic performance for the degradation of TC (Fig. 6). Depend on the functions of various radicals such as $\cdot\text{OH}$ and $\cdot\text{O}_2^-$, TC could be degraded to produce CO_2 , H_2O and other small molecules.

4. Conclusions

In summary, 2D rGO and $g\text{-C}_3\text{N}_4$ co-modified 3D TiO_2 nanotube arrays photoelectrodes were successfully prepared through the process of impregnation, annealing and electrochemical deposition. The introduction of $g\text{-C}_3\text{N}_4$ and rGO not only enhanced visible light adsorption, but also promoted the transfer of photo-generated electrons between $g\text{-C}_3\text{N}_4$ and TiO_2 . The high reduction properties of $g\text{-C}_3\text{N}_4$ were effectively preserved due to the prominent electrons transfer ability of rGO. Meanwhile, $\text{rGO}@g\text{-C}_3\text{N}_4/\text{TNAs}$ photoelectrodes demonstrated the higher open circuit potential and transient photocurrent density compared to TNAs and $g\text{-C}_3\text{N}_4/\text{TNAs}$ photoelectrodes. The $\text{rGO}@g\text{-C}_3\text{N}_4/\text{TNAs}$ photoelectrodes exhibited excellent photocatalytic degradation performance for TC. Besides, $\text{rGO}@g\text{-C}_3\text{N}_4/\text{TNAs}$ photoelectrodes showed a remarkable stability due to the reduction of photocorrosion. The photocatalytic degradation mechanism was dominated by $\cdot\text{OH}$ and $\cdot\text{O}_2^-$ radicals. In this work, the preparation of 3D $\text{rGO}@g\text{-C}_3\text{N}_4/\text{TNAs}$ photoelectrodes would provide useful experimental basis for the purification of organic pollutants in water body.

CRediT authorship contribution statement

Bin Zhang: Investigation, Writing - original draft, Methodology, Formal analysis, Writing - review & editing. **Xiaohan Ma:** Methodology, Validation, Formal analysis, Data curation. **Jun Ma:** Supervision. **Yuanming Zhou:** Data curation, Formal analysis. **Guocheng Liu:** Data curation, Project administration. **Dong Ma:** Data curation, Formal analysis. **Zhihan Deng:** Data curation, Formal analysis. **Mingming Luo:** Data curation, Formal analysis. **Yanjun Xin:** Conceptualization, Writing - review & editing, Resources, Supervision, Funding acquisition.

Declaration of Competing Interest

The authors declare that they have no known competing financial interests or personal relationships that could have appeared to influence the work reported in this paper.

Acknowledgements

This work was supported by National Natural Science Foundation of China (No. 51678323), Natural Science Foundation of Shandong Province (No. ZR2019MD012, ZR2017MEE026), Support Plan on Youth Innovation Science and Technology for Higher Education of Shandong Province (No. 2019KJD014) and Natural Science Foundation of Heilongjiang Province (B2015024).

References

- [1] H. Li, W. Tu, Y. Zhou, Z. Zou, Z-Scheme photocatalytic systems for promoting photocatalytic performance: recent progress and future challenges, *Adv. Sci. (Weinh)* 3 (2016) 1500389.

- [2] S. Wang, P. Kuang, B. Cheng, J. Yu, C. Jiang, ZnO hierarchical microsphere for enhanced photocatalytic activity, *J. Alloys Compd.* 741 (2018) 622–632.
- [3] T. Di, B. Cheng, W. Ho, J. Yu, H. Tang, Hierarchically CdS–Ag₂S nanocomposites for efficient photocatalytic H₂ production, *Appl. Surf. Sci.* 470 (2019) 196–204.
- [4] X. Chen, D. Chu, L. Wang, W. Hu, H. Yang, J. Sun, S. Zhu, G. Wang, J. Tao, S. Zhang, One-step synthesis of novel hierarchical flower-like SnO₂ nanostructures with enhanced photocatalytic activity, *J. Alloys Compd.* 729 (2017) 710–715.
- [5] X. Feng, P. Wang, J. Hou, J. Qian, Y. Ao, C. Wang, Significantly enhanced visible light photocatalytic efficiency of phosphorus doped TiO₂ with surface oxygen vacancies for ciprofloxacin degradation: Synergistic effect and intermediates analysis, *J. Hazard. Mater.* 351 (2018) 196–205.
- [6] M. Yang, J. Liu, X. Zhang, S. Qiao, H. Huang, Y. Liu, Z. Kang, C₃N₄-sensitized TiO₂ nanotube arrays with enhanced visible-light photoelectrochemical performance, *Phys. Chem. Chem. Phys.* 17 (2015) 17887–17893.
- [7] L. Yang, L. Xu, X. Bai, P. Jin, Enhanced visible-light activation of persulfate by Ti (3⁺) self-doped TiO₂/graphene nanocomposite for the rapid and efficient degradation of micropollutants in water, *J. Hazard. Mater.* 365 (2019) 107–117.
- [8] H. Dong, G. Zeng, L. Tang, C. Fan, C. Zhang, X. He, Y. He, An overview on limitations of TiO₂-based particles for photocatalytic degradation of organic pollutants and the corresponding countermeasures, *Water Res.* 79 (2015) 128–146.
- [9] M. Ge, J. Cai, J. Iocozzia, C. Cao, J. Huang, X. Zhang, J. Shen, S. Wang, S. Zhang, K. Zhang, Y. Lai, Z. Lin, A review of TiO₂ nanostructured catalysts for sustainable H₂ generation, *Int. J. Hydrogen Energy.* 42 (2017) 8418–8449.
- [10] Q. Chen, Y. Xin, X. Zhu, Au-Pd nanoparticles-decorated TiO₂ nanobelts for photocatalytic degradation of antibiotic levofloxacin in aqueous solution, *Electrochim. Acta* 186 (2015) 34–42.
- [11] V. Etacheri, C. Di Valentin, J. Schneider, D. Bahnemann, S.C. Pillai, Visible-light activation of TiO₂ photocatalysts: Advances in theory and experiments, *J. Photochem. Photobiol., C* 25 (2015) 1–29.
- [12] Y. Xin, M. Gao, Y. Wang, D. Ma, Photoelectrocatalytic degradation of 4-nonylphenol in water with WO₃/TiO₂ nanotube array photoelectrodes, *Chem. Eng. J.* 242 (2014) 162–169.
- [13] H. Park, Y. Park, W. Kim, W. Choi, Surface modification of TiO₂ photocatalyst for environmental applications, *J. Photochem. Photobiol., C* 15 (2013) 1–20.
- [14] Z. Shayegan, C. Lee, F. Haghighat, TiO₂ photocatalyst for removal of volatile organic compounds in gas phase – A review, *Chem. Eng. J.* 334 (2018) 2408–2439.
- [15] Q. Zhou, Z. Fang, J. Li, M. Wang, Applications of TiO₂ nanotube arrays in environmental and energy fields: A review, *Microporous Mesoporous Mater.* 202 (2015) 22–35.
- [16] Y. Xin, Q. Chen, G. Zhang, Construction of ternary heterojunction CuS–CdS/TiO₂ nanobelts for photocatalytic degradation of gaseous toluene, *J. Alloys Compd.* 751 (2018) 231–240.
- [17] Y. Xin, H. Liu, Y. Liu, D. Ma, Q. Chen, Composition and photoelectrochemical properties of WO₃/TNAs photoelectrodes fabricated by in situ electrochemical method, *Electrochim. Acta* 104 (2013) 308–313.
- [18] R. Hao, G. Wang, H. Tang, L. Sun, C. Xu, D. Han, Template-free preparation of macro/mesoporous g-C₃N₄/TiO₂ heterojunction photocatalysts with enhanced visible light photocatalytic activity, *Appl. Catal. B* 187 (2016) 47–58.
- [19] L. Jiang, X. Yuan, Y. Pan, J. Liang, G. Zeng, Z. Wu, H. Wang, Doping of graphitic carbon nitride for photocatalysis: A review, *Appl. Catal. B* 217 (2017) 388–406.
- [20] D. Masih, Y. Ma, S. Rohani, Graphitic C₃N₄ based noble-metal-free photocatalyst systems, *Appl. Catal. B* 206 (2017) 556–588.
- [21] B. Sun, N. Lu, Y. Su, H. Yu, X. Meng, Z. Gao, Decoration of TiO₂ nanotube arrays by graphitic-C₃N₄ quantum dots with improved photoelectrocatalytic performance, *Appl. Surf. Sci.* 394 (2017) 479–487.
- [22] J. Fu, Q. Xu, J. Low, C. Jiang, J. Yu, Ultrathin 2D/2D WO₃/g-C₃N₄ step-scheme H₂-production photocatalyst, *Appl. Catal. B* 243 (2019) 556–565.
- [23] Q. Zhang, F. Yang, S. Zhou, N. Bao, Z. Xu, M. Chaker, D. Ma, Broadband photocatalysts enabled by 0D/2D heterojunctions of near-infrared quantum dots/graphitic carbon nitride nanosheets, *Appl. Catal. B* 270 (2020).
- [24] Y. Tan, Z. Shu, J. Zhou, T. Li, W. Wang, Z. Zhao, One-step synthesis of nanostructured g-C₃N₄/TiO₂ composite for highly enhanced visible-light photocatalytic H₂ evolution, *Appl. Catal. B* 230 (2018) 260–268.
- [25] L. Kong, X. Zhang, C. Wang, J. Xu, X. Du, L. Li, Ti 3+ defect mediated g-C₃N₄/TiO₂ Z-scheme system for enhanced photocatalytic redox performance, *Appl. Surf. Sci.* 448 (2018) 288–296.
- [26] X. Wang, F. Wang, C. Bo, K. Cheng, J. Wang, J. Zhang, H. Song, Promotion of phenol photodecomposition and the corresponding decomposition mechanism over g-C₃N₄/TiO₂ nanocomposites, *Appl. Surf. Sci.* 453 (2018) 320–329.
- [27] D. Ma, J. Wu, M. Gao, Y. Xin, T. Ma, Y. Sun, Fabrication of Z-scheme g-C₃N₄/RGO/Bi₂WO₆ photocatalyst with enhanced visible-light photocatalytic activity, *Chem. Eng. J.* 290 (2016) 136–146.
- [28] D. Zhou, Z. Chen, Q. Yang, X. Dong, J. Zhang, L. Qin, In-situ construction of all-solid-state Z-scheme g-C₃N₄/TiO₂ nanotube arrays photocatalyst with enhanced visible-light-induced properties, *Sol. Energy Mater. Sol. Cells.* 157 (2016) 399–405.
- [29] X. Chen, J. Wei, R. Hou, Y. Liang, Z. Xie, Y. Zhu, X. Zhang, H. Wang, Growth of g-C₃N₄ on mesoporous TiO₂ spheres with high photocatalytic activity under visible light irradiation, *Appl. Catal. B* 188 (2016) 342–350.
- [30] R. Hao, G. Wang, C. Jiang, H. Tang, Q. Xu, In situ hydrothermal synthesis of g-C₃N₄/TiO₂ heterojunction photocatalysts with high specific surface area for Rhodamine B degradation, *Appl. Surf. Sci.* 411 (2017) 400–410.
- [31] W. Kong, X. Zhang, B. Chang, Y. Zhou, S. Zhang, G. He, B. Yang, J. Li, Fabrication of B doped g-C₃N₄/TiO₂ heterojunction for efficient photoelectrochemical water oxidation, *Electrochim. Acta* 282 (2018) 767–774.
- [32] J. Ma, C. Wang, H. He, Enhanced photocatalytic oxidation of NO over g-C₃N₄-TiO₂ under UV and visible light, *Appl. Catal., B* 184 (2016) 28–34.
- [33] X. Song, Y. Hu, M. Zheng, C. Wei, Solvent-free in situ synthesis of g-C₃N₄/TiO₂ composite with enhanced UV- and visible-light photocatalytic activity for NO oxidation, *Appl. Catal., B* 182 (2016) 587–597.
- [34] K. Sridharan, E. Jang, T.J. Park, Novel visible light active graphitic C₃N₄-TiO₂ composite photocatalyst: Synergistic synthesis, growth and photocatalytic treatment of hazardous pollutants, *Appl. Catal., B* 142–143 (2013) 718–728.
- [35] S. Zhou, Y. Liu, J. Li, Y. Wang, G. Jiang, Z. Zhao, D. Wang, A. Duan, J. Liu, Y. Wei, Facile in situ synthesis of graphitic carbon nitride (g-C₃N₄)-N-TiO₂ heterojunction as an efficient photocatalyst for the selective photoreduction of CO₂ to CO, *Appl. Catal., B* 158–159 (2014) 20–29.
- [36] L. Liu, G. Zhang, J.T.S. Irvine, Y. Wu, Organic Semiconductor g-C₃N₄ modified TiO₂ nanotube arrays for enhanced photoelectrochemical performance in wastewater treatment, *Energy Technol.* 3 (2015) 982–988.
- [37] C. Han, Y. Wang, Y. Lei, B. Wang, N. Wu, Q. Shi, Q. Li, In situ synthesis of graphitic-C₃N₄ nanosheet hybridized N-doped TiO₂ nanofibers for efficient photocatalytic H₂ production and degradation, *Nano Res.* 8 (2014) 1199–1209.
- [38] Y. Li, Z. Chen, M. Wang, L. Zhang, S. Bao, Interface engineered construction of porous g-C₃N₄/TiO₂ heterostructure for enhanced photocatalysis of organic pollutants, *Appl. Surf. Sci.* 440 (2018) 229–236.
- [39] Z. Wei, F. Liang, Y. Liu, W. Luo, J. Wang, W. Yao, Y. Zhu, Photoelectrocatalytic degradation of phenol-containing wastewater by TiO₂/g-C₃N₄ hybrid heterostructure thin film, *Appl. Catal. B* 201 (2017) 600–606.
- [40] H. Wang, Y. Liang, L. Liu, J. Hu, W. Cui, Highly ordered TiO₂ nanotube arrays wrapped with g-C₃N₄ nanoparticles for efficient charge separation and increased photoelectrocatalytic degradation of phenol, *J. Hazard. Mater.* 344 (2018) 369–380.
- [41] M. Huang, J. Yu, Q. Hu, W. Su, M. Fan, B. Li, L. Dong, Preparation and enhanced photocatalytic activity of carbon nitride/titania(001 vs 101 facets)/reduced graphene oxide (g-C₃N₄/TiO₂/rGO) hybrids under visible light, *Appl. Surf. Sci.* 389 (2016) 1084–1093.
- [42] G. Wang, Q. Chen, Y. Xin, Y. Liu, Z. Zang, C. Hu, B. Zhang, Construction of graphene-WO₃/TiO₂ nanotube array photoelectrodes and its enhanced performance for photocatalytic degradation of dimethyl phthalate, *Electrochim. Acta* 222 (2016) 1903–1913.
- [43] C. Wang, G. Zhang, C. Zhang, M. Wu, M. Yan, W. Fan, W. Shi, A facile one-step solvothermal synthesis of bismuth phosphate-graphene nanocomposites with enhanced photocatalytic activity, *J. Colloid Interface Sci.* 435 (2014) 156–163.
- [44] Q. Zhang, N. Bao, X. Zhu, D. Ma, Y. Xin, Preparation and photocatalytic properties of graphene/TiO₂ nanotube arrays photoelectrodes, *J. Alloys Compd.* 618 (2015) 761–767.
- [45] W. Lin, X. Xie, X. Wang, Y. Wang, D. Segets, J. Sun, Efficient adsorption and sustainable degradation of gaseous acetaldehyde and o-xylene using rGO-TiO₂ photocatalyst, *Chem. Eng. J.* 349 (2018) 708–718.
- [46] H.M. Jang, E. Kan, A novel hay-derived biochar for removal of tetracyclines in water, *Bioresour. Technol.* 274 (2019) 162–172.
- [47] Y. Chen, Y. Ma, J. Yang, L. Wang, J. Lv, C. Ren, Aqueous tetracycline degradation by H₂O₂ alone: Removal and transformation pathway, *Chem. Eng. J.* 307 (2017) 15–23.
- [48] Y. Xin, H. Liu, L. Han, Y. Zhou, Comparative study of photocatalytic and photoelectrocatalytic properties of alachlor using different morphology TiO₂/Ti photoelectrodes, *J. Hazard. Mater.* 192 (2011) 1812–1818.
- [49] S. Xin, J. Shen, G. Liu, Q. Chen, Z. Xiao, G. Zhang, Y. Xin, High electricity generation and COD removal from cattle wastewater in microbial fuel cells with 3D air cathode employed non-precious Cu₂O/reduced graphene oxide as cathode catalyst, *Energy* 196 (2020).
- [50] M. Andreozzi, M.G. Álvarez, S. Conreras, F. Medina, L. Clarizia, G. Vitiello, J. Llorca, R. Marotta, Treatment of saline produced water through photocatalysis using rGO-TiO₂ nanocomposites, *Catal. Today* 315 (2018) 194–204.
- [51] H.Y. Hafeez, S.K. Lakhera, S. Bellamkonda, G.R. Rao, M.V. Shankar, D.W. Bahnemann, B. Neppolian, Construction of ternary hybrid layered reduced graphene oxide supported g-C₃N₄-TiO₂ nanocomposite and its photocatalytic hydrogen production activity, *Int. J. Hydrogen Energy* 43 (2018) 3892–3904.
- [52] L. Zhang, X. He, X. Xu, C. Liu, Y. Duan, L. Hou, Q. Zhou, C. Ma, X. Yang, R. Liu, F. Yang, L. Cui, C. Xu, Y. Li, Highly active TiO₂/g-C₃N₄/G photocatalyst with extended spectral response towards selective reduction of nitrobenzene, *Appl. Catal. B* 203 (2017) 1–8.
- [53] J. Zhang, S. Fang, J. Mei, G. Zheng, X. Zheng, X. Guan, High-efficiency removal of rhodamine B dye in water using g-C₃N₄ and TiO₂ co-hybridized 3D graphene aerogel composites, *Sep. Purif. Technol.* 194 (2018) 96–103.
- [54] T. Giannakopoulou, I. Papailias, N. Todorova, N. Boukos, Y. Liu, J. Yu, C. Trapalis, Tailoring the energy band gap and edges' potentials of g-C₃N₄/TiO₂ composite photocatalysts for NO_x removal, *Chem. Eng. J.* 310 (2017) 571–580.
- [55] X. Jiang, Q. Xing, X. Luo, F. Li, J. Zou, S. Liu, X. Li, X. Wang, Simultaneous photoreduction of Uranium(VI) and photooxidation of Arsenic(III) in aqueous solution over g-C₃N₄/TiO₂ heterostructured catalysts under simulated sunlight irradiation, *Appl. Catal. B* 228 (2018) 29–38.

- [56] G. Zhang, H. Miao, X. Hu, J. Mu, X. Liu, T. Han, J. Fan, E. Liu, Y. Yin, J. Wan, A facile strategy to fabricate Au/TiO₂ nanotubes photoelectrode with excellent photoelectrocatalytic properties, *Appl. Surf. Sci.* 391 (2017) 345–352.
- [57] D. Zheng, Y. Xin, D. Ma, X. Wang, J. Wu, M. Gao, Preparation of graphene/TiO₂ nanotube array photoelectrodes and their photocatalytic activity for the degradation of alachlor, *Catal. Sci. Technol.* 6 (2016) 1892–1902.
- [58] F. Wu, X. Li, W. Liu, S. Zhang, Highly enhanced photocatalytic degradation of methylene blue over the indirect all-solid-state Z-scheme g-C₃N₄-RGO-TiO₂ nanoheterojunctions, *Appl. Surf. Sci.* 405 (2017) 60–70.
- [59] S. Ni, F. Han, W. Wang, D. Han, Y. Bao, D. Han, H. Wang, L. Niu, Innovations upon antioxidant capacity evaluation for cosmetics: A photoelectrochemical sensor exploitation based on N-doped graphene/TiO₂ nanocomposite, *Sens. Actuators, B* 259 (2018) 963–971.
- [60] J. Low, B. Cheng, J. Yu, Surface modification and enhanced photocatalytic CO₂ reduction performance of TiO₂: a review, *Appl. Surf. Sci.* 392 (2017) 658–686.
- [61] G. Wang, Q. Zhang, Q. Chen, X. Ma, Y. Xin, X. Zhu, D. Ma, C. Cui, J. Zhang, Z. Xiao, Photocatalytic degradation performance and mechanism of dibutyl phthalate by graphene/TiO₂ nanotube array photoelectrodes, *Chem. Eng. J.* 358 (2019) 1083–1090.



Construction of netlike 3D Z-scheme photoelectrodes with improved photocatalytic performance based on g-C₃N₄ nanosheets modified TiO₂ nanobelt-tubes

Xiaohan Ma^{a,1}, Qinghua Chen^{a,1}, Guocheng Liu^a, Yuanming Zhou^b, Dong Ma^a, Shuaishuai Xin^a, Chengze Yu^a, **Bin Zhang^{a,*}**, Yanjun Xin^{a,*}

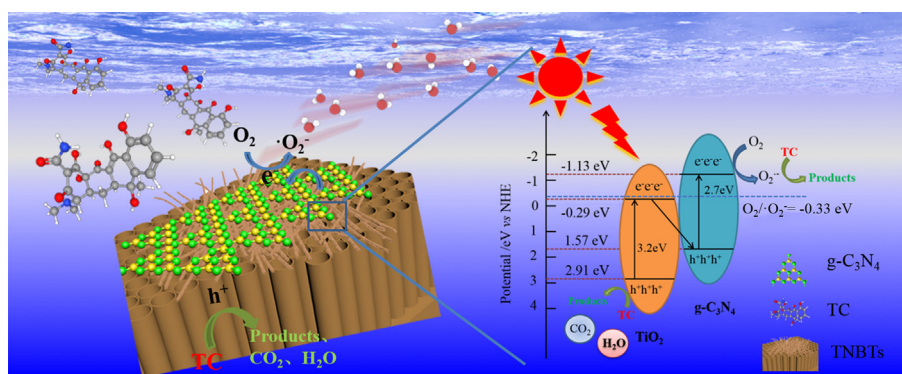
^a Qingdao Engineering Research Center for Rural Environment, College of Resources and Environment, Qingdao Agricultural University, Qingdao 266109, PR China

^b Central Laboratory, Qingdao Agricultural University, Qingdao 266109, PR China

HIGHLIGHTS

- Network 3D Z-scheme g-C₃N₄ nanosheets/TiO₂ nanobelt-tubes photoelectrodes was synthesized.
- The TiO₂ nanobelt-tubes structure improved the transfer efficiency of electrons.
- Z-scheme heterostructure facilitated the separation of photogenerated electron hole pairs.
- g-C₃N₄/TNBTs heterostructure exhibited stronger photocatalytic degradation of TC.

GRAPHICAL ABSTRACT



ARTICLE INFO

Article history:

Received 4 March 2020

Received in revised form 18 May 2020

Accepted 24 May 2020

Available online 29 May 2020

Keywords:

Graphitic carbon nitrogen
TiO₂ nanobelt-tubes network
Three-dimensional Z-scheme
Photocatalytic degradation
Tetracycline hydrochloride

ABSTRACT

Netlike 3D Z-scheme graphitic carbon nitride (g-C₃N₄) nanosheets decorated TiO₂ nanobelt-tubes (TNBTs) photoelectrodes (g-C₃N₄/TNBTs) were fabricated via anodization and coating technology. The network 3D photoelectrodes were characterized by HR-TEM, XPS and UV-Vis/DRS. The photoelectrochemical properties were examined to reveal the transfer and separation efficiency of photogenerated electrons. The photocatalytic activity was investigated by the photocatalytic decomposition of tetracycline hydrochloride (TC) under light irradiation. Results showed that g-C₃N₄ with rugged surface were loaded on TNBTs by chemical bond joint to form heterostructure. The g-C₃N₄/TNBTs exhibited stronger visible light absorption and reduced recombination of photogenerated electron-hole pairs than TNBTs. The photocurrent response of g-C₃N₄/TNBTs was ~1.88-fold that of TNBTs. The photocatalytic rate of g-C₃N₄/TNBTs for TC was significantly higher than that of TNBTs (0.017 min⁻¹ vs 0.007 min⁻¹). The ·O₂⁻ and h⁺ were the dominant oxidation species during the degradation of TC. The possible photocatalytic mechanism of constructing Z-scheme heterojunction was also proposed.

© 2020 Elsevier Ltd. All rights reserved.

1. Introduction

Recently, with the rapid development of veterinary and human medicine, potential environmental risks caused by antibiotics abuse has raised widespread attention (Roy et al., 2020;

* Corresponding author.

E-mail address: xintom2000@126.com (Y. Xin).

¹ X. Ma and Q. Chen contributed equally to this work.

Wang et al., 2019b; Wu et al., 2019a). It is thus that the degradation of wastewater containing antibiotics is urgent for human health and environmental protection (Yu et al., 2020). Tetracycline hydrochloride (TC), as important broad-spectrum antibiotics, which are extensively applied in human and veterinary medicine against infectious diseases, and their residues from the application can encourage the growth of antibiotic resistant pathogens and cause serious health and environmental issues (Chen et al., 2018; Xue et al., 2018; Zhao et al., 2019). Hence, it is a great mission to develop an efficient treatment technology to remove these tetracycline residues in the aquatic environment.

Photocatalysts have potential applications in the decomposition of contaminants and the development of new energy by utilizing solar energy as a sustainable energy source (Jiang et al., 2018; Yang et al., 2017). Fujishima and Honda firstly reported titanium dioxide (TiO_2) for hydrogen production in 1972 (Inoue et al., 1979), TiO_2 has become a promising candidate to dealing with the problems of environmental and energy crisis owing to its chemical stability, environmental-friendliness and strong oxidizing power (Turolla et al., 2018; Moreira et al., 2012). Nevertheless, TiO_2 intrinsic shortcomings of the restrained UV-light response and the rapid recombination of electron-hole pairs exhibit significant limitations in the photocatalytic reaction process. Up to now, various endeavors, such as ion doping (Schlexer et al., 2018), dye sensitization (Mohan et al., 2019) and coupling with other visible-light semiconductors (Huang et al., 2015; Mishra et al., 2018; Wu et al., 2019b; Zhang et al., 2018b; Zhou et al., 2018), have been employed to ameliorate the photocatalytic performance of TiO_2 . Thereinto, coupling with narrow band gap semiconductors is a strategy to promote the transfer of electron-hole pairs and enhance the visible light absorption (Li et al., 2019a; Sheng et al., 2019; Wang et al., 2014; Ye et al., 2012). Unfortunately, when two semiconductors are coupled, the photo-generated carriers are transferred into conduction band (CB) and valence band (VB) of opposite semiconductor according to the potential difference, thus the redox ability of composite semiconductors would be reduced (Chen et al., 2014a,b; Li et al., 2013). Compared with traditional heterostructures, all-solid-state Z-scheme systems with excellent redox ability have attractive advantages in charge separation and transportation (Zhou et al., 2014).

Since graphitic carbon nitrogen ($g\text{-C}_3\text{N}_4$) was firstly used for water splitting to produce H_2 by Wang et al. (2009), it has gained much attention in the domain of photocatalysis for CO_2 reduction (Brunetti et al., 2019), pollutant degradation (Cerdan et al., 2018; Zhang et al., 2020) and organic synthesis (Cao et al., 2015). The $g\text{-C}_3\text{N}_4$ possesses a band gap of 2.84 eV with the CB located at -1.19 eV and VB located at $+1.65$ eV vs normal hydrogen electrode (NHE), which can absorb visible light at wavelengths less than 437 nm (Boonprakob et al., 2014). The CB of $g\text{-C}_3\text{N}_4$ is adequately negative, many photocatalytic reduction reactions are promoted on the $g\text{-C}_3\text{N}_4$ surface. Furthermore, $g\text{-C}_3\text{N}_4$ has outstanding physicochemical stability on account of strong covalent bond between C and N (Chen et al., 2016; Liao et al., 2012; Liu et al., 2011). However, the VB potential and the band gap of $g\text{-C}_3\text{N}_4$ lead to weak oxidation ability and fast recombination of photo-generated carriers. Hence, the $g\text{-C}_3\text{N}_4$ with appropriate band position can be modified with TiO_2 to form a matched Z-scheme heterostructure. The distance between the VB of $g\text{-C}_3\text{N}_4$ ($+1.65$ eV) and the CB of TiO_2 (-0.30 eV) is less than their own band gap, thus the electrons in the CB of TiO_2 are readily combined with holes in the VB of $g\text{-C}_3\text{N}_4$, which makes the photogenerated electrons to accumulate in the CB of $g\text{-C}_3\text{N}_4$ with strong reducibility and the holes to accumulate in the VB of TiO_2 with high oxidative capability. TiO_2 powder modified by the 0-dimensional (0D) or 2-dimensional (2D) $g\text{-C}_3\text{N}_4$ has been illustrated to improve photocatalytic performance and raise the separation efficiency of photo-

generated carriers because of Z-scheme heterogeneous structure (Liu et al., 2019b; Lu et al., 2018; Sridharan et al., 2013). Wang et al. (2019a) constructed three-dimension (3D) TiO_2 microflowers/ $g\text{-C}_3\text{N}_4$ nanosheets through hydrothermal and calcination process, showing the excellent H_2 production activity benefiting from an effective direct Z-scheme heterojunction. Li et al. (2017) suggested that Z-scheme $g\text{-C}_3\text{N}_4\text{-TiO}_2$ nanocomposites have higher photocatalytic activity for the propylene degradation.

However, the huge cost of separating TiO_2 powder from suspension is one of the main drawbacks hindering the practical utilization of this process in pollutant treatment. The immobilized 1-dimensional (1D) TiO_2 nanostructures such as nanowires (Tan et al., 2013) and nanobelts (Chen et al., 2013) prepared by anodic oxidation have higher photochemical activity and practical application prospect compared with TiO_2 powder because of its abundant exposed edge sites, large specific surface area and overcoming the disadvantage of powder suspension (Liu et al., 2015; Zhai et al., 2014). In order to advance the transfer of photoinduced electrons and further improve photocatalytic activity, a highly ordered 1D/3D TiO_2 nanobelt-tubes (TNBTs) network photoelectrodes were tried to obtain by adjusting the anodic oxidation parameters. As we have seen, there are no literature on the construction and properties of netlike 3D Z-scheme $g\text{-C}_3\text{N}_4$ /TNBTs photoelectrodes. The mechanisms of charge transfer and photocatalysis are still unclear.

Hence, we design the highly ordered 1D/3D TNBTs network embellished with 2D $g\text{-C}_3\text{N}_4$ to construct all-solid-state network 3D Z-scheme $g\text{-C}_3\text{N}_4$ /TNBTs photoelectrodes by anodization and coating technology. In this 3D composite photoelectrode, there are three key advantages: (1) TiO_2 nanobelts provide 1D structure to increase reactive sites and enhance optical capture capability; (2) $g\text{-C}_3\text{N}_4$ nanosheets and TiO_2 form close heterostructure to enhance the optical absorption range and promote electron transfer; and (3) highly ordered TiO_2 nanotube arrays serve as efficient carriers transfer medium. The photocatalytic properties of $g\text{-C}_3\text{N}_4$ /TNBTs photoelectrodes was studied by photocatalytic degradation of TC. The heterostructure formed between $g\text{-C}_3\text{N}_4$ nanosheets and TNBTs network was examined by analyzing surface morphology, optical and photoelectric properties. The transfer mechanism of photo-induced carriers and degradation mechanism of TC over the $g\text{-C}_3\text{N}_4$ /TNBTs photoelectrodes were proposed.

2. Materials and methods

2.1. Materials

Hydrofluoric acid (HF, $\geq 40.0\%$), ethanol (75%), acetone ($\geq 99.5\%$), ammonium fluoride (NH_4F , $\geq 96.0\%$), ethylene glycol ($\geq 99.5\%$), melamine ($\geq 99.0\%$), *p*-benzoquinone (BQ, $\geq 98.0\%$), tert-butylalcohol (TBA, $\geq 98.0\%$) and ammonium oxalate (AO, $\geq 99.5\%$) were provided by Sinopharm Chemical Reagent Co. Ltd. TC (96%) are purchased from Aladdin (Shanghai China). Titanium (Ti) foils (99%) with a thickness of 0.2 mm were used raw materials. All the chemicals were analytical-grade without further purification. Ultrapure water was used in all solutions.

2.2. Synthesis of netlike $g\text{-C}_3\text{N}_4$ /TNBTs photoelectrodes

Prior to anodization, the Ti foil was pickled in a mixture containing HF and H_2O (1:1) for 15 s and then dried in air. Desiccative Ti foil was polished by 600, 1000 and 2000 mesh sandpaper in turn. Following, Ti foil was sonicated for 3 min in ultrapure water, ethanol-acetone mixture (1:1) and ultrapure water, respectively.

Netlike TNBTs photoelectrodes were fabricated by an anodization method with Ti foil (reaction area of 4 cm^2) was used as the

anode and platinum foil as cathode. The electrolyte contains ethylene glycol, 0.5 wt% ammonium fluoride (NH_4F) and 7 vol% water by inputting constant voltage of 60 V at 20 °C for 2.5 h. After, the photoelectrodes were rinsed completely with ultrapure water and dried at 101 °C for 30 min.

Ethylene glycol solution containing 10 g/L melamine was coated on surface of TNBTs photoelectrodes using a brush with various times (1, 3, 5 and 7 times) and dried in a muffle furnace at 200 °C for 10 min. Subsequently, the coated TNBTs photoelectrodes were annealed at 550 °C for 2 h after each coating. The photoelectrodes were called as $\text{g-C}_3\text{N}_4/\text{TNBTs-n}$, where n referred to the coating times.

2.3. Characterization

The microstructure and electron diffraction of the photoelectrodes were characterized by a scanning electron microscope (SEM, Hitachi S-4800, Japan), high-resolution transmission electron microscopy (HR-TEM, Tecnai G220, America). The crystal structure was investigated by X-ray diffraction (XRD, Bruker AXS, Germany) with $\text{Cu K}\alpha 1$ radiation (40 kV/30 mA). X-ray photoelectron spectroscopy (XPS) was detected using a Thermo ESCALAB 250Xi on a monochromatized $\text{Al K}\alpha$ (1486.68 eV) X-ray sources. UV-Vis diffuse reflectance spectra (DRS) were examined from a TU-1901 UV-Vis spectrophotometers. The functional properties of photoelectrodes were recorded with a Fourier transform infrared (FTIR) spectroscopy (UATR Two, PerkinElmer, USA). Photoluminescence (PL) spectra were verified by a F-4600 fluorescence spectrometer (Hitachi) with excitation wavelength of 325 nm.

The photoelectrochemical performance was investigated by measuring photocurrent response, electrochemical impedance spectra (EIS) and open-circuit voltage (V_{oc}) on an electrochemical workstation (CHI660E, China) with a standard three-electrode system, comprising the as-prepared photoelectrodes (working electrode), platinum foil (counter electrode), a saturated calomel electrode (reference electrode) and 0.1 mol/L Na_2SO_4 solution as the electrolyte. The light source was a 35 W Xenon light (Philips). The EIS measurement was conducted with frequency range of 100 kHz to 0.01 Hz at a bias of 0 V.

2.4. Photocatalytic performance

Photocatalytic performance of as-prepared photoelectrodes (TNBTs and $\text{g-C}_3\text{N}_4/\text{TNBTs-n}$ photoelectrodes) placed vertically in the quartz beaker were comparatively investigated by evaluating the degradation and rate of 2 mg/L TC solution as a model reaction. Prior to light irradiation, the quartz beaker was placed under stirring for 30 min to obtain adsorption/desorption equilibrium of TC on the photoelectrodes, and was then irradiated to a 50 W xenon lamp (CEL-HXF300) for 2 h. The concentration of TC solution at specific time intervals was measured by HPLC (Agilent 1100) with a mobile phase containing water (0.005 mol/L oxalic acid) and methanol (60/40, v/v) employing a flow rate of 1.0 mL/min. The column was C18 (4.6 mm \times 250 mm, 5 μm) and the absorbance wavelengths was 356 nm.

3. Results and discussion

3.1. Morphology and phase structures

SEM and HR-TEM images distinctly indicate the external morphology and microstructure of the photoelectrodes (Fig. 1). Fig. 1a was clearly observed that netlike TNBTs photoelectrodes exhibited well-ordered netlike 3D nanotube structure at the bottom and 1D belt-like structure on the surface with width of 20–

50 nm and length of 2–3 μm (the inset of Fig. 1a). This 1D/3D nanobelt-tubes channels are beneficial for increasing the reaction sites of organic pollutants and furthering the transfer of photo-induced carriers as efficient migration pathways (Chen et al., 2014a,b). Fig. 1b showed that some rough surface materials with 2D structure covered on the top of the TNBTs, which indicated that the $\text{g-C}_3\text{N}_4$ was effortlessly attached to TNBTs to form a network 3D photoelectrodes. Notably, several $\text{g-C}_3\text{N}_4$ stacking layers was clearly seen on the surface of TNBTs with the increase of coating times to 5 times, indicating the coatings times could affect the number of deposited layers. A well 1D belt-like and 3D nanotube network still existed, suggesting that the subsequent deposition of $\text{g-C}_3\text{N}_4$ did not deform the intrinsic structure of TNBTs.

The selected area electron diffraction pattern of the $\text{g-C}_3\text{N}_4/\text{TNBTs-5}$ photoelectrodes in the inset of Fig. 1c showed obvious polycrystalline rings for the good crystallization of TiO_2 (Ma et al., 2016). Fig. 1d showed that the different orientations and lattice spacing were 0.35, 0.23 and 0.32 nm, which are in accord with the TiO_2 (1 0 1), (0 0 1) and $\text{g-C}_3\text{N}_4$ (0 0 2) planes, respectively. Besides, EDX spectra showed the main elemental compositions of $\text{g-C}_3\text{N}_4/\text{TNBTs-5}$ photoelectrodes. The major signals of Ti, O, C and N elements were concurrently discovered in $\text{g-C}_3\text{N}_4/\text{TNBTs-5}$ photoelectrodes, whose total scale were 14.88%, 36.20%, 30.60% and 17.73%, respectively, which further demonstrated that $\text{g-C}_3\text{N}_4$ were on the TNBTs surface (Fig. 1e). These results confirmed the existence of heterostructure between $\text{g-C}_3\text{N}_4$ and TiO_2 , and the deposition of $\text{g-C}_3\text{N}_4$ nanosheets on TNBTs, which could extend visible light response and accelerate the photo-induced carriers separation. Up to now, a network 3D integration interface between $\text{g-C}_3\text{N}_4$ and TiO_2 has been expressed, which probably shows their individual advantages, for instance, $\text{g-C}_3\text{N}_4$ could broaden the absorption range towards the visible region and increase the probability of contact between reactants and photoelectrodes, TNBTs are beneficial to the transfer of photoexcited carriers. Importantly, Z-scheme heterostructure structure formed by $\text{g-C}_3\text{N}_4$ and TiO_2 can enhance the redox ability.

XRD spectroscopy were investigated to analyze the crystallographic structure of the TNBTs, $\text{g-C}_3\text{N}_4$ and $\text{g-C}_3\text{N}_4/\text{TNBTs}$ photoelectrodes. In Fig. 2a, the diffraction peaks of TNBTs and $\text{g-C}_3\text{N}_4/\text{TNBTs}$ photoelectrodes were observed. The peaks at 25.1°, 37.2°, 48.2°, 55.0°, 55.7°, 63.7° and 40.4°, 53.5°, 70.9° can be indexed to the characteristic peaks of anatase TiO_2 (JCPDS, No. 21-1272) and Ti (JCPDS, No. 65-3362), respectively, indicating the single crystal anatase structure, which are in conformity with the HR-TEM consequence. XRD spectra of pristine $\text{g-C}_3\text{N}_4$ are displayed in Fig. 2b. The diffraction peaks at 13.1° and 28.0° were observed and can be well-indexed to (1 0 0) and (0 0 2) planes (JCPDS, No. 87-1526), which belongs to the hexagonal phase graphite-like structure (Wen et al., 2018). The peak at 13.1° corresponds to the regular arrangement of triazine rings in $\text{g-C}_3\text{N}_4$ plane. The strong and sharp diffraction peak at 28.0° is characteristic interlayer stacking of π -conjugated aromatic system with the interlayer spacing of 0.318 nm by the Bragg equation. It is further demonstrated that the diffraction peak is related to the (0 0 2) plane of $\text{g-C}_3\text{N}_4$ ($d_{002} = 0.322$ nm). The results obtained were consistent with the previous report (Liu et al., 2019a; Zhao et al., 2005). For $\text{g-C}_3\text{N}_4/\text{TNBTs-5}$ and $\text{g-C}_3\text{N}_4/\text{TNBTs-7}$, the peak of $\text{g-C}_3\text{N}_4$ were observed, the intensity of diffraction peak increased gradually upon enhancing the coating times. For $\text{g-C}_3\text{N}_4/\text{TNBTs-1}$ and $\text{g-C}_3\text{N}_4/\text{TNBTs-3}$, the characteristic diffraction peaks of $\text{g-C}_3\text{N}_4$ were not measured. This may be attributed to lower loading and poor crystallization of $\text{g-C}_3\text{N}_4$ deposited (Yu et al., 2013; Zhang et al., 2012). Fig. 2c shows the XRD spectra of fresh and used $\text{g-C}_3\text{N}_4/\text{TNBTs-3}$ photoelectrodes. The used photoelectrodes had been recycled for 5 times (10 h). The diffraction peaks of Ti, anatase TiO_2 and $\text{g-C}_3\text{N}_4$ were observed in XRD patterns of both the fresh and used $\text{g-C}_3\text{N}_4/$

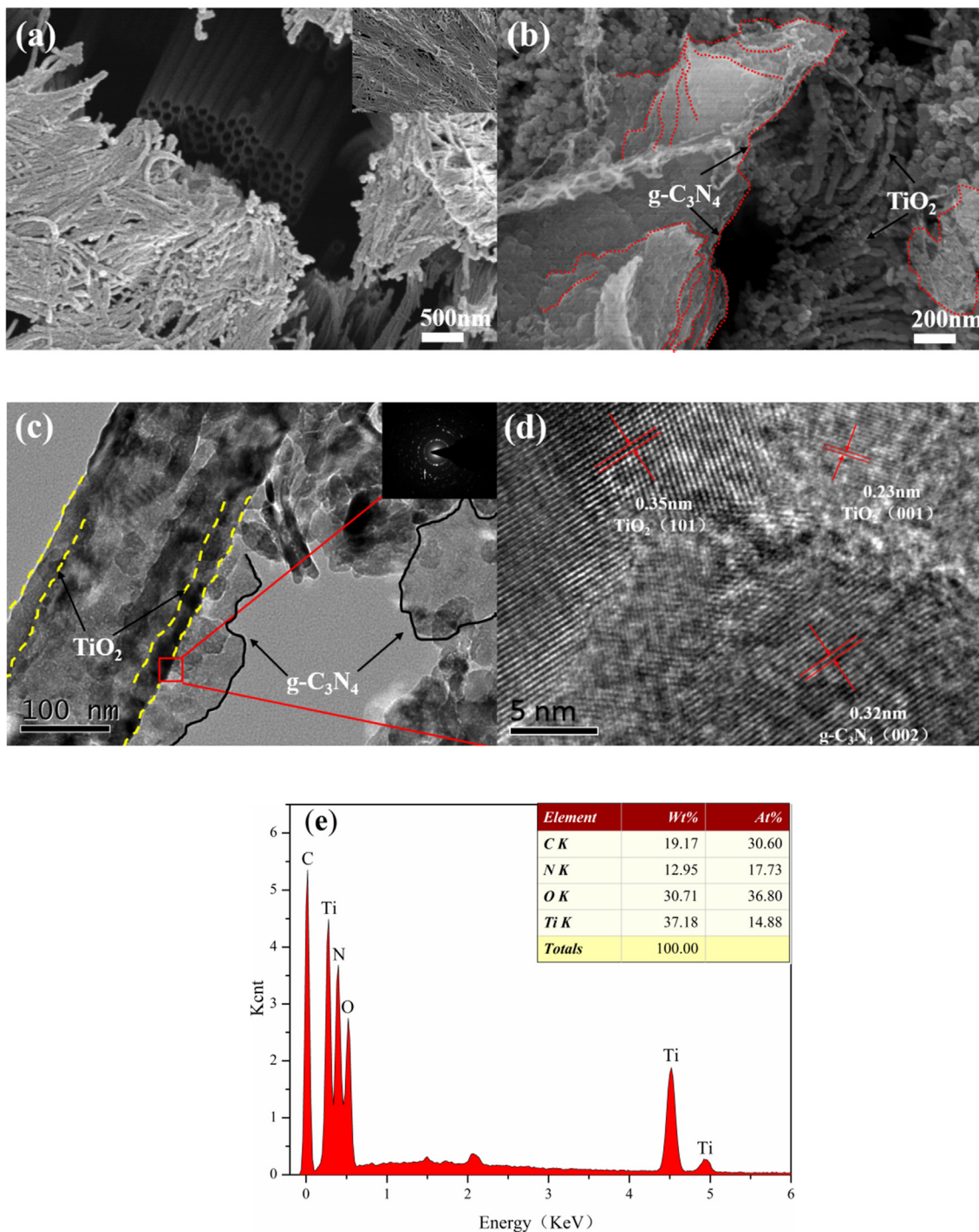


Fig. 1. SEM images of TNBTs (a) and g-C₃N₄/TNBTs-5 (b) photoelectrodes, TEM image of g-C₃N₄/TNBTs-5 photoelectrodes (c), HR-TEM image of g-C₃N₄/TNBTs-5 photoelectrodes (d), EDX of g-C₃N₄/TNBTs-5 photoelectrodes (e).

TNBTs-3 photoelectrodes, and the corresponding peak intensity and position do not change. It can be concluded that the crystallographic structure of the used g-C₃N₄/TNBTs photoelectrodes has not been altered.

3.2. XPS characterization

The chemical bonding and status of surface elements on the TNBTs and g-C₃N₄/TNBTs-3 photoelectrodes were further determined by XPS. Fig. 3 illustrated the full survey spectrum and the high-resolution survey spectrum of Ti 2p, O 1s, C 1s and N 1s ele-

ments. O, Ti, C, and N were all found in the g-C₃N₄/TNBTs-3 photoelectrodes (Fig. 3a). As shown in Fig. 3b, the peaks at 464.1 eV and 458.4 eV corresponds to Ti 2p_{1/2} and Ti 2p_{3/2} of TiO₂, respectively. There was a distance of 5.7 eV between the two peaks, indicating that the valence state of Ti was Ti⁴⁺ in TiO₂ (Liu et al., 2018). Compared with TNBTs photoelectrodes, the Ti 2p_{1/2} and Ti 2p_{3/2} peaks slightly deviated of 0.2 eV to lower binding energy in the g-C₃N₄/TNBTs-3 photoelectrodes, which was probably caused a change in the density of the electron cloud by partial substitution of Ti–O with Ti–N (Hamal and Klabunde, 2011; Wang et al., 2018b). The results confirmed that g-C₃N₄/TNBTs-3 heterostructures formed by

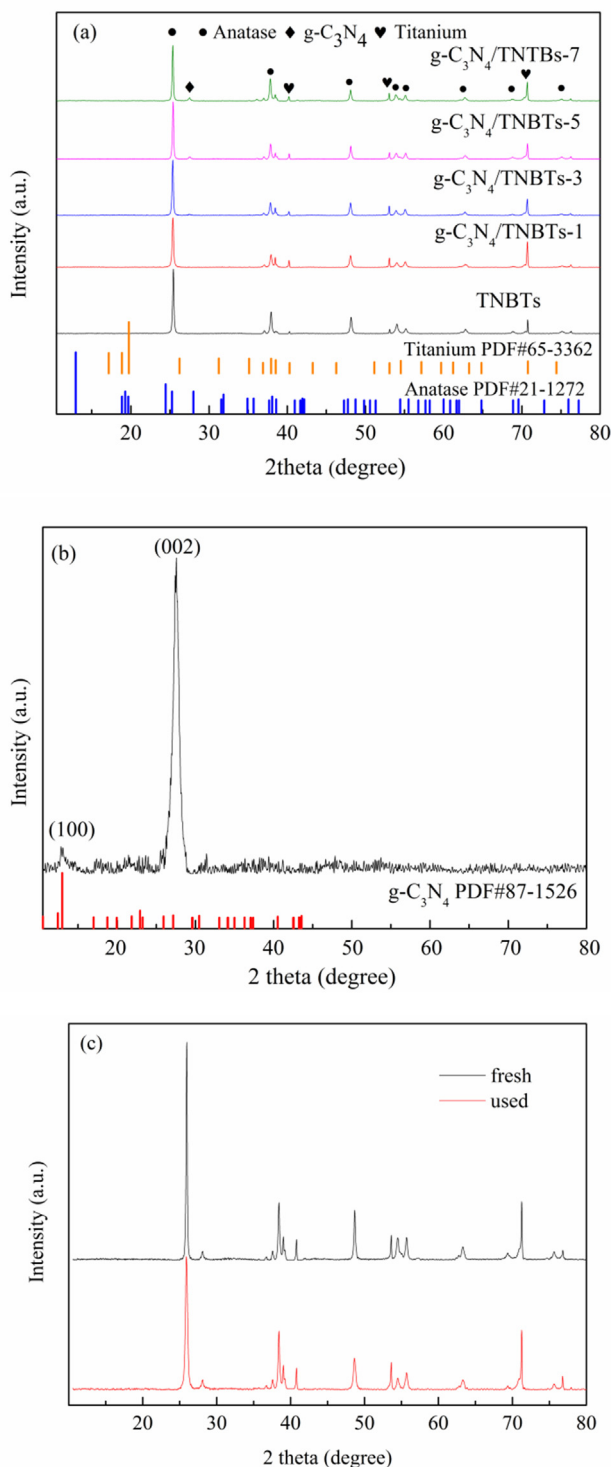


Fig. 2. XRD spectra of TNBTs, g-C₃N₄/TNBTs-n photoelectrodes (a), pure g-C₃N₄ (b) and used and fresh g-C₃N₄/TNBTs-3 photoelectrodes (c).

chemical bond joint rather than physical mixture (Wang et al., 2018a,b). The two peaks of O 1s XPS spectrum (Fig. 3c) were located at 529.8 V and 531.7 V, which were well assigned to Ti–O–Ti linkages in TiO₂ and –OH functional groups from the oxygen absorbed on the surface of TNBTs, respectively. Additionally, the binding energy of O 1s also has a slight decrease, which was probably caused by the chemical configuration (Lakhera et al., 2018). The high-resolution C 1s spectrum of g-C₃N₄/TNBTs-3 photoelectrodes were shown in Fig. 3d, asymmetric and broad peaks can be divided into

three peaks at 284.8, 286.0 and 288.3 eV, corresponding to C–C (Zhang et al., 2018a), sp² C atoms in the tri-s-triazine ring (N=C–N₂) (Lu et al., 2017) and sp³ C atoms bonded to N (C–N) of g-C₃N₄, respectively (Dong et al., 2015; Su et al., 2016). In Fig. 3e, The N1s spectrum was fitted into three peaks at 398.4, 399.3 and 400.5 eV, which are assigned to sp²-hybridized N bonded to carbon atoms (C=N–C) in thiazine rings, bridging nitrogen (N–(C)₃) and terminal amino functional groups with a hydrogen atom (–NH or –NH₂), respectively (Ma et al., 2016; Zhang et al., 2012). The existence of N–(C)₃ groups corroborated the polymerization of melamine, while the –NH or –NH₂ groups proved that melamine pyrolysis to synthesize g-C₃N₄ was incomplete condensation (Zhou et al., 2013). According to the result of XPS spectrum, g-C₃N₄ was successfully modified on the TNBTs surface via coating method, which were compatible with the above-mentioned XRD and HR-TEM.

3.3. FTIR and PL spectra analysis

The FTIR spectra of TNBTs and g-C₃N₄/TNBTs-3 photoelectrodes were conducted to analysis the chemical bonding and compositions, as shown in Fig. 4. The sharp peak at 806 cm^{−1} are assigned to the out-of-plane stretching vibration of C–N heterocycles in 3-s-triazine units (Kumar et al., 2013; Wang and Zhang, 2012). There were several strong bands in the range of 1000–1800 cm^{−1}, which were related to the characteristic stretching vibration of C–N heterocycles. Thereinto, the band of 1237–1456 cm^{−1}, with 1237, 1320, 1401 and 1456 cm^{−1}, corresponds to the stretching vibration of C–N and aromatic rings. The absorption peaks at 1548–1632 cm^{−1} were caused by the stretching vibration of C=N (Liu et al., 2015). The shoulder broad absorption at 2913–3335 cm^{−1} were accordance with the NH bond of free amino groups at the defect sites of the aromatic ring (Zhang et al., 2017). The characteristic peaks of TNBTs were not observed.

PL can also be employed to determine the photo-induced carriers behaviors of the photoelectrodes, bandgap energy level distribution, surface oxygen vacancies and defects, etc. The PL spectra of TNBTs and g-C₃N₄/TNBTs photoelectrodes in the wavelength range of 300–600 nm are shown in Fig. 5. The emission peaks of TNBTs centered at 383 and 396 nm were mainly attribute to the band-band transition of photo-induced carriers. Four peaks were detected at 452, 468, 484 and 494 nm, possibly attribute to defects and oxygen vacancies on the surface of TNBTs (Wang et al., 2018a; Lakshminarasimhan et al., 2007). In addition, the PL intensity reduced when the g-C₃N₄ was decorated into the TNBTs photoelectrodes, suggesting that g-C₃N₄/TNBTs photoelectrodes have better photogenerated carriers separation efficiency. The holes in the VB of g-C₃N₄ were combined with the electrons in the CB of TiO₂, which can release low fluorescence energy and leave holes in the VB of TiO₂ and electrons in the CB of g-C₃N₄ with stronger redox ability, respectively. Consequently, it can be predicted that the formation of Z-scheme heterostructure of netlike g-C₃N₄/TNBTs photoelectrodes will exhibit higher photocatalytic activity.

3.4. UV–Vis DRS results

The optical properties of photoelectrodes are extremely important in determining the decomposition of contaminants under solar light. The UV–Vis DRS of TNBTs, g-C₃N₄ and g-C₃N₄/TNBTs-3 photoelectrodes were recorded (Fig. 6a). For pristine TNBTs photoelectrodes, the optical band edge was 390 nm, which according with the intrinsic band gap of 3.2 eV, thus, the TNBTs photoelectrodes could only be excited by ultraviolet light. However, the absorption edge of g-C₃N₄ was extended to visible light (about 450 nm), which was owing to the charge transfer response from VB migrated by N 2p orbit to the CB formed by C 2p orbit (Li et al., 2016). After the incorporation of g-C₃N₄, the optical absorp-

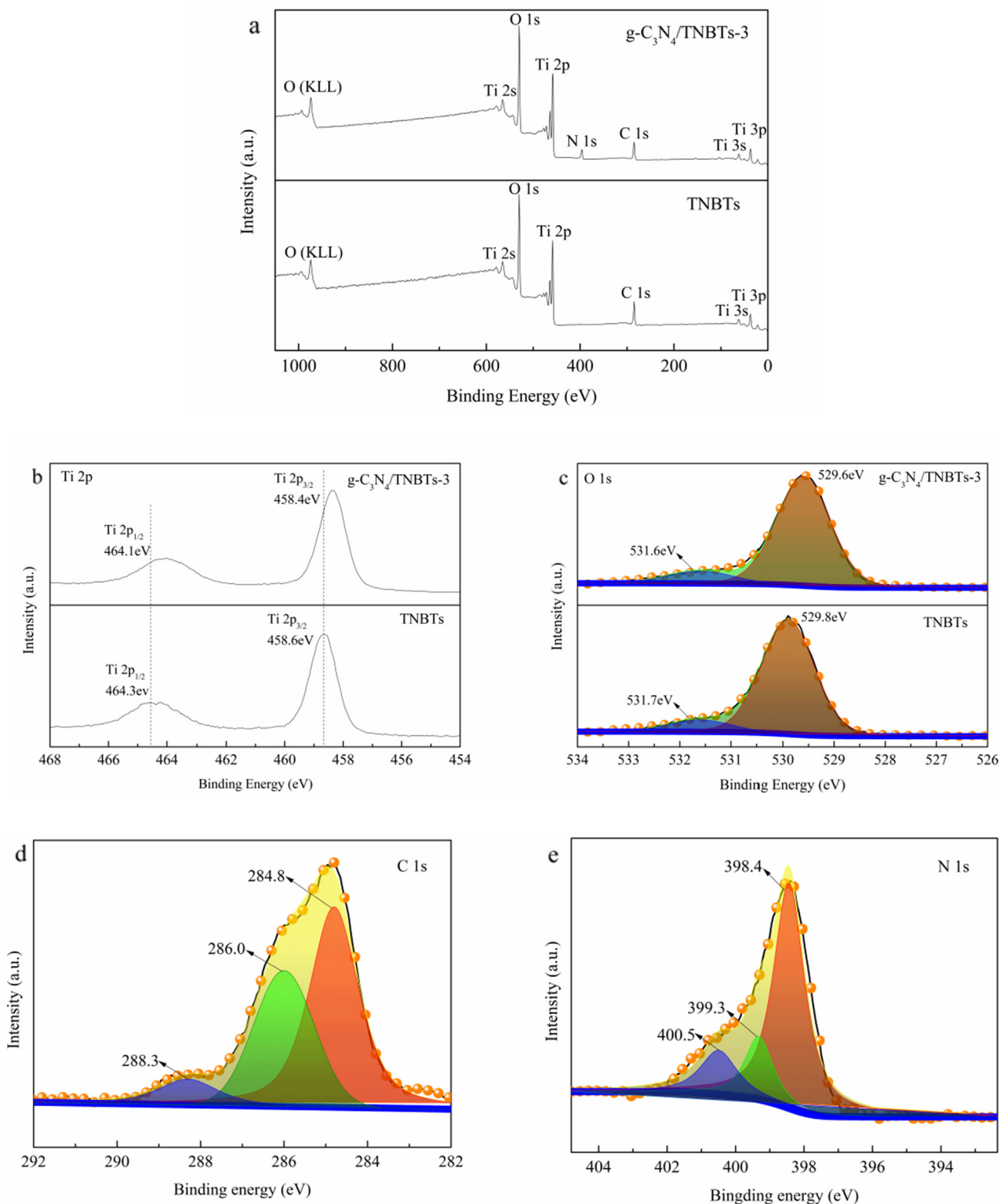


Fig. 3. Full-scale XPS spectra of TNBTs and g-C₃N₄/TNBTs-3 photoelectrodes (a) and high-resolution Ti 2p (b) and O 1s (c) XPS spectra of TNBTs and g-C₃N₄/TNBTs-3 photoelectrodes; C 1s spectrum of g-C₃N₄/TNBTs-3 (d), N 1s spectrum of g-C₃N₄/TNBTs-3 (e) photoelectrodes.

tion intensity of g-C₃N₄/TNBTs-3 photoelectrodes in both ultraviolet and visible light regions was significantly enhanced than that of TNBTs photoelectrodes, and the light absorption intensity of g-C₃N₄/TNBTs-3 photoelectrodes after 500 nm was higher than that of the ultraviolet region. The above phenomenon may be attributed

to the surface defect sites formed during heat treatment as well as light scattering by nanobelt-tubes or pores in the TNBTs array and the a compact interaction between TNBTs and g-C₃N₄, which increase the transmission length of incident light and enhance the visible light capture capacity of network 3D g-C₃N₄/TNBTs

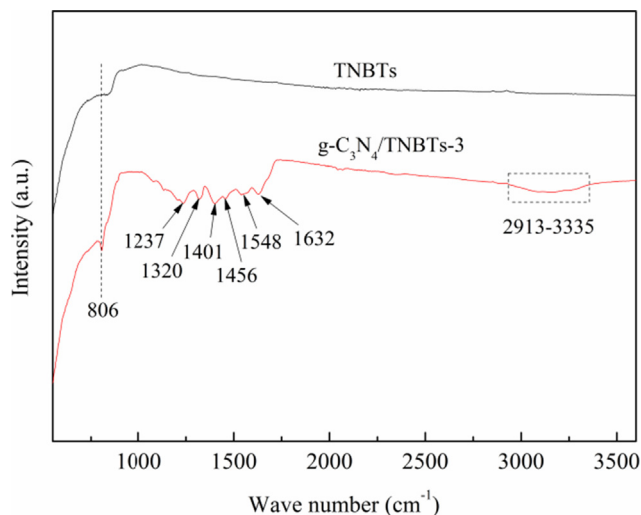


Fig. 4. FT-IR spectra of TNBTs and $g\text{-C}_3\text{N}_4/\text{TNBTs-3}$ photoelectrodes.

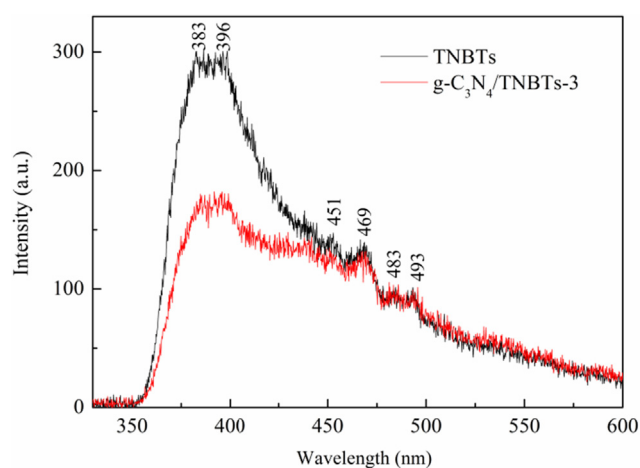


Fig. 5. PL spectra of TNBTs and $g\text{-C}_3\text{N}_4/\text{TNBTs-3}$ photoelectrodes.

photoelectrodes (Tan et al., 2018; Wang et al., 2018a,b; Zhu et al., 2009).

The bandgap energy of semiconductors can be evaluated by the Kubelka-Munk equation (Fig. 6b). The bandgap of pristine TNBTs and $g\text{-C}_3\text{N}_4$ were 3.2 and 2.7 eV, respectively. After coupling TNBTs with $g\text{-C}_3\text{N}_4$, the bandgap of TNBTs photoelectrodes changed to 3.0 eV. The improvement of optical absorption and red shift imply that the utilization of visible light was improved, leading to more electron-hole pairs and the separation of photo-induced carriers was improved owing to a compact interaction between TNBTs and $g\text{-C}_3\text{N}_4$. Consequently, it is easy to illustrate why $g\text{-C}_3\text{N}_4/\text{TNBTs}$ has improving photocatalytic activity than TNBTs.

3.5. Photoelectrochemical performance

The separation and migration efficiency can be evaluated by measuring the transient photocurrent density and V_{oc} vs time under repeated 50 s on/off irradiation cycles. The interior resistance and charge transfer kinetics of photoelectrodes could be employed using EIS (Zhao et al., 2018). From Fig. 7a, all the photoelectrodes exhibited the rise and fall response for each switch on-off illumination cycle, and the photocurrent response was completely invertible. The photocurrent density of the prepared $g\text{-C}_3\text{N}_4/\text{TNBTs-3}$ was higher than $0.028 \text{ mA}\cdot\text{cm}^{-2}$, which was almost

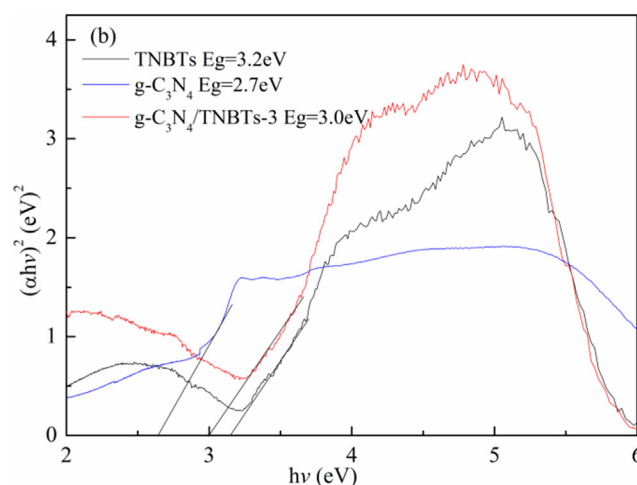
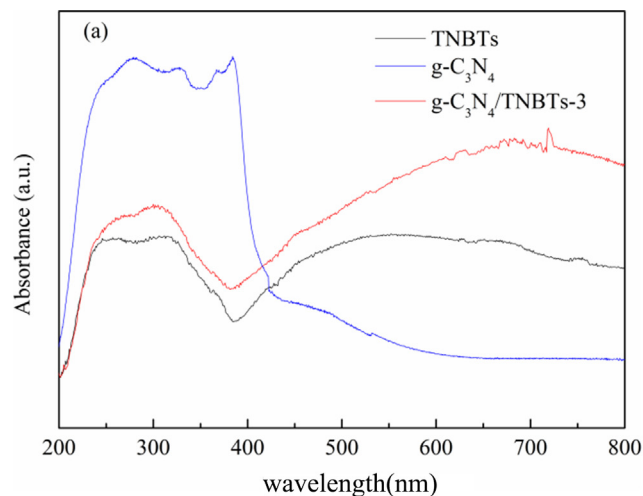


Fig. 6. UV-Vis diffuse reflectance absorption spectra (a) and plots of $(\alpha h\nu)^2$ vs photon energy ($h\nu$) (b) for TNBTs, $g\text{-C}_3\text{N}_4$ and $g\text{-C}_3\text{N}_4/\text{TNBTs-3}$ photoelectrodes.

1.47-fold and 1.88-fold that of the $g\text{-C}_3\text{N}_4$ ($0.019 \text{ mA}\cdot\text{cm}^{-2}$) and TNBTs photoelectrodes ($0.015 \text{ mA}\cdot\text{cm}^{-2}$), respectively. The enhancement of the photocurrent density of $g\text{-C}_3\text{N}_4/\text{TNBTs-3}$ can be attributed to two factors: (1) the broaden light absorption spectrum region and improved absorption intensity for the construction of $g\text{-C}_3\text{N}_4/\text{TNBTs}$ heterostructure; and (2) the enhanced charge transportation efficiency because of the formation of $g\text{-C}_3\text{N}_4/\text{TNBTs}$ heterojunction (Li et al., 2015; Zhang et al., 2018a).

The V_{oc} response is an effective method to detect the generation and aggregation of electrons under open-circuit condition and illumination. As shown in Fig. 7b, most of the excited electrons transferred and aggregated in TiO_2 film, resulting in the transfer of Fermi level to a more negative potential and the V_{oc} was gradually increasing after the light was on. Because of the competition of electrons aggregation and carriers recombination, V_{oc} reached a maximum and then maintains a steady state (Benjamin and Prashant, 2009; Mor et al., 2006). Obviously, $g\text{-C}_3\text{N}_4/\text{TNBTs-3}$ photoelectrodes exhibited higher photovoltage ($\sim 0.08 \text{ V}$) than TNBTs ($\sim 0.07 \text{ V}$) photoelectrodes. However, the photovoltage of $g\text{-C}_3\text{N}_4/\text{TNBTs-3}$ photoelectrodes showed a quickly increase, which was significantly different from the delayed increase of TNBTs photoelectrode. There are two possible reasons for the above phenomenon of TNBTs and $g\text{-C}_3\text{N}_4/\text{TNBTs-3}$ photoelectrodes: (1) the narrower bandgap of $g\text{-C}_3\text{N}_4$ can effectively improve the utilization of light, thus the most stimulated photoelectrons transferred and accumulated on the CB of $g\text{-C}_3\text{N}_4$; (2) the CB electrons of TiO_2

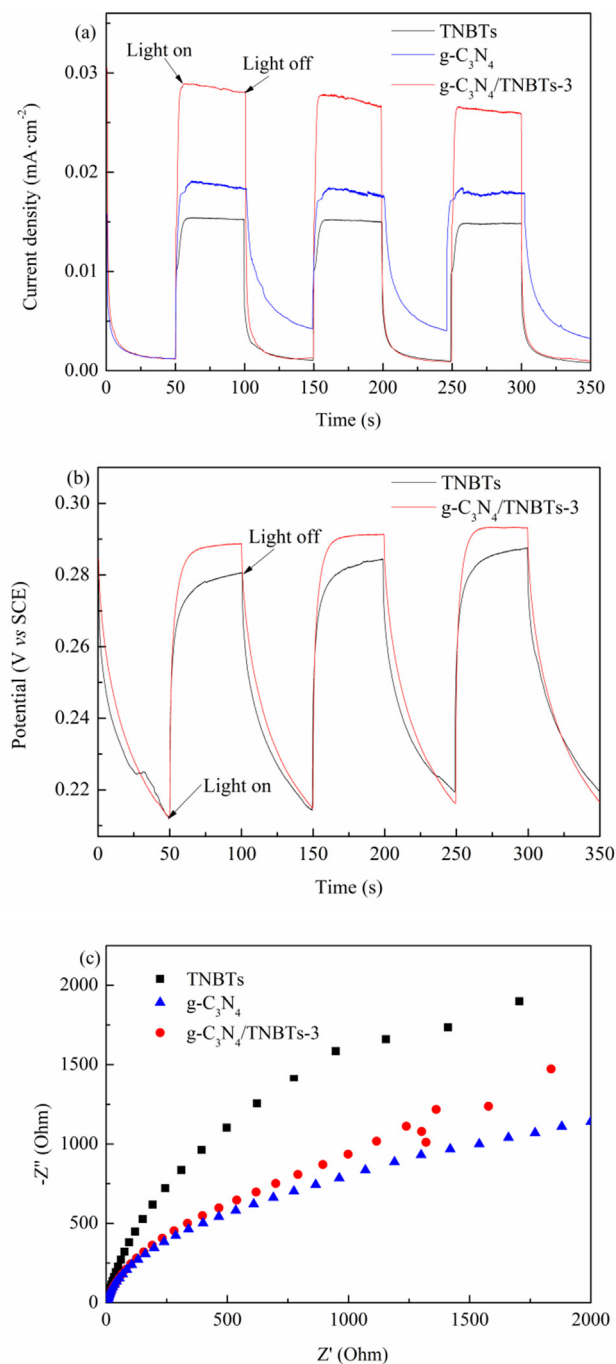


Fig. 7. Photocurrent (a) and Nyquist plots of EIS (c) response of TNBTs, g-C₃N₄ and g-C₃N₄/TNBTs-3 photoelectrodes, V_{oc} (b) of TNBTs and g-C₃N₄/TNBTs-3.

rapidly recombined with VB holes of g-C₃N₄, because of the matching between g-C₃N₄ and TNBTs. After stopping the illumination, the V_{oc} gradually decreased as the electrons accumulated in the photoelectrodes was slowly discharged and trapped through electrons acceptors in the electrolyte. The results of transient photocurrent density and V_{oc} demonstrated certainly that the network 3D g-C₃N₄/TNBTs heterostructure could improve the interfacial transfer efficiency and separation of photogenerated carriers, thus giving rise to an enhanced photocatalytic performance.

The diameter of semicircle in Nyquist diagram in EIS represents the information of the charge transfer resistance. Accordingly, it is evident that compared to TNBTs, g-C₃N₄ and g-C₃N₄/TNBTs-3

composites show much smaller semicircle diameter (Fig. 7c). This suggested that the g-C₃N₄/TNBTs-3 photoelectrodes possess a smaller charge transfer resistance and smoother charge diffusion after g-C₃N₄ modification with smallest charge transfer resistance, indicating efficient charge separation and interfacial transfer.

3.6. Photocatalytic performance and stability

To estimate the photocatalytic performance of the photoelectrodes, the removal of TC was executed by the TNBTs and g-C₃N₄/TNBTs photoelectrodes under initial TC concentration of 2 mg/L and light illumination of 120 min. To achieve adsorption equilibrium of TC molecule on the photoelectrodes surface, TC solution were magnetically stirred for 30 min before illumination. In contrast with TNBTs (59%), the significantly improved degradation rates of TC on the g-C₃N₄/TNBTs-1, g-C₃N₄/TNBTs-3, g-C₃N₄/TNBTs-5, g-C₃N₄/TNBTs-7 and g-C₃N₄/TNBTs-9 photoelectrodes were 73%, 90%, 80%, 70% and 69%, respectively (see Fig. 8a). The removal rates of TC can be enhanced with increase of coating times, and the g-C₃N₄/TNBTs-3 photoelectrodes had highest photocatalytic performance. However, the photocatalytic performance of g-C₃N₄/TNBTs-5, g-C₃N₄/TNBTs-7 and g-C₃N₄/TNBTs-9 photoelectrodes significantly decreased with the increase of coating times. The degradation process of TC by the photoelectrodes could be fitted by kinetic equation as follow:

$$\ln(C_t/C_0) = -kt \quad (1)$$

where C_0 and C_t are the initial concentration and the concentration of TC at reaction time t , respectively.

As displayed in Fig. 8b, the k and regression coefficients (R^2) were determined by the linear relationship of $\ln(C_0/C_t)$ and t . It was apparent that the k of g-C₃N₄/TNBTs-3 photoelectrodes (0.017 min⁻¹) was ~2.4-fold that of TNBTs photoelectrodes (0.007 min⁻¹).

Above phenomenon could be ascribed to the following three factors. Firstly, the formation of netlike 3D Z-scheme g-C₃N₄/TNBTs heterostructure enlarge light absorption range and restrain the recombination of the photogenerated carries. Secondly, more active sites for TC decomposition would be provided with the increase of the loading amount of g-C₃N₄ nanosheets. Thirdly, g-C₃N₄/TNBTs heterostructure would be strengthened with the increase of coating times, which further promoted the separation of photogenerated electron-hole pairs, causing the improvement of photocatalytic performance. However, the coating times of g-C₃N₄ exceeded 3 times, it was not beneficial for the utilization of light of TNBTs photoelectrode, and excessive g-C₃N₄ would become the recombination center of photogenerated carriers (Wang et al., 2015).

Besides, reusability is a significant indicator for practical application of photoelectrodes in water remediation. Therefore, the durability was examined by repeating the photocatalytic decomposition of TC on the g-C₃N₄/TNBTs heterostructures under light irradiation (Fig. 9a). The photocatalytic performance of g-C₃N₄/TNBTs-3 photoelectrodes decreased slightly before 3 consecutive cycles and stabilized afterwards. It could be concluded that the g-C₃N₄/TNBTs-3 photoelectrodes possess relatively high stability in the photocatalytic decomposition of TC, which were compatible with the unchanged XRD spectra of the used photoelectrodes.

3.7. Possible photocatalytic mechanism of g-C₃N₄/TNBTs photoelectrodes

To ascertain main reactive species and inquire into the photocatalytic decomposition mechanism of TC by g-C₃N₄/TNBTs photoelectrodes, the free radical and hole quenching experiments were implemented through adding different scavengers. Here, TBA, BQ

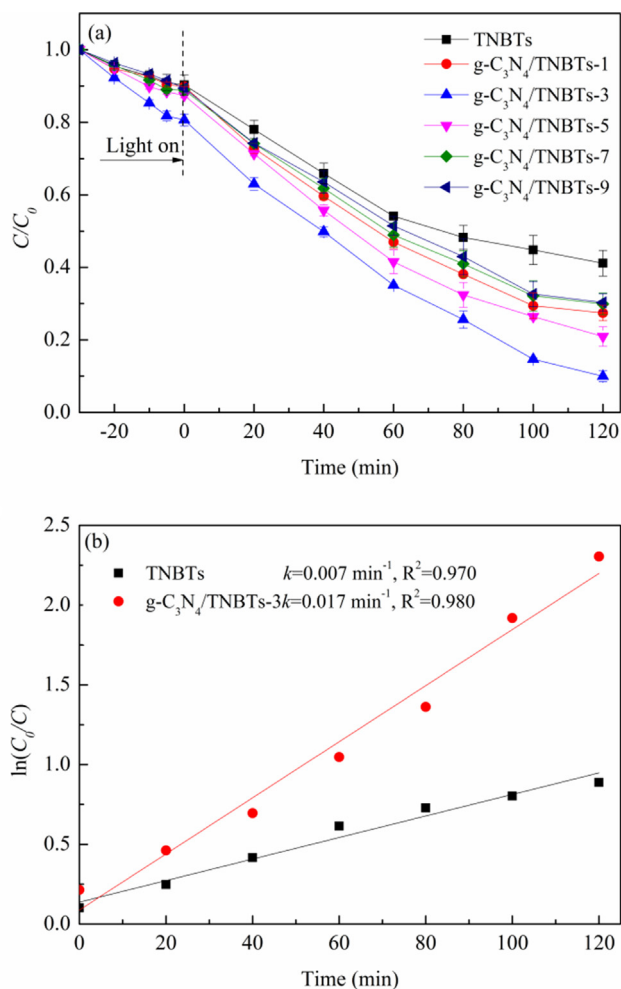


Fig. 8. Photocatalytic degradation (a) of TC on TNBTs and g-C₃N₄/TNBTs-9 photoelectrodes and rate constant (b) of TC on TNBTs and g-C₃N₄/TNBTs-3 photoelectrodes.

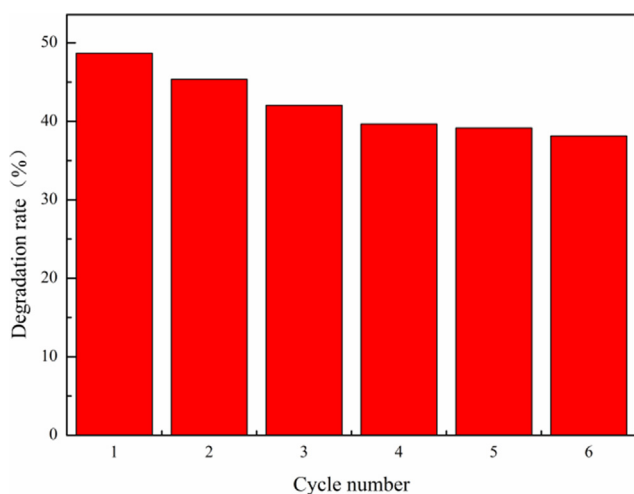


Fig. 9. Circulating runs in the degradation of TC over g-C₃N₄/TNBTs-3 photoelectrodes.

and AO were adopted as the scavengers of hydroxyl radicals ($\cdot\text{OH}$), superoxide radicals ($\cdot\text{O}_2^-$), and holes (h^+), respectively (Li et al., 2019b; She et al., 2018). As illustrated in Fig. 10, the decomposition efficiency of TC was 100.0% over g-C₃N₄/TNBTs photoelectrodes

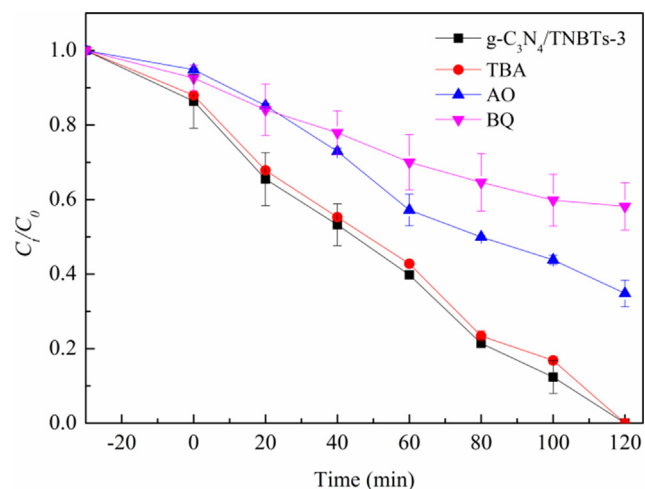


Fig. 10. Photocatalytic degradation of TC by g-C₃N₄/TNBTs-3 photoelectrodes under trapping of radical species.

without adding possessory active species scavenger. Notably, the removal efficiency of TC was suppressed to 41.8%, 65.2%, and 100.0% in the presence of AO, BQ and TBA, respectively. Obviously, the order of repression degree was AO > BQ > TBA, which also manifested that h^+ and $\cdot\text{O}_2^-$ acted as the main reactive species on the TC decomposition by g-C₃N₄/TNBTs photoelectrodes.

Zhou et al. (2016) demonstrated that $\cdot\text{OH}$ and $\cdot\text{O}_2^-$ were the primary active radicals in Rh.B photodecomposition over g-C₃N₄/TiO₂ nanotube arrays photocatalyst. Liu et al. (2019b) confirmed the content of $\cdot\text{O}_2^-$ and $\cdot\text{OH}$ was boosted by the Z-scheme g-C₃N₄/TiO₂ heterojunction. Nevertheless, h^+ and $\cdot\text{O}_2^-$ were the major active species for the decomposition of TC by g-C₃N₄/TNBTs photoelectrodes according to our experiment results. It may be a result of h^+ were more likely to react with a great deal of TC adsorbed on the g-C₃N₄/TNBTs photoelectrodes surface, instead of reacting with $\cdot\text{OH}/\text{H}_2\text{O}$ to generate $\cdot\text{OH}$.

To analyze the mechanism of photocatalytic reaction, The VB edge (E_{VB}) and CB edge (E_{CB}) of g-C₃N₄ and TNBTs can be speculated by Kubelka-Munk function (Eqs. (2) and (3)) (Zhang et al., 2017):

$$E_{\text{VB}} = X - E_e + 0.5E_g \quad (2)$$

$$E_{\text{CB}} = E_{\text{VB}} - E_g \quad (3)$$

The E_{VB} of g-C₃N₄ and TNBTs were calculated to be 1.57 eV and 2.91 eV, respectively. So, the E_{CB} of g-C₃N₄ and TNBTs were -1.13 eV and -0.29 eV, respectively.

On account of the E_{CB} and E_{VB} of g-C₃N₄ and TNBTs by Kubelka-Munk function and aforementioned analysis, an exploratory mechanism for the degradation of TC was proposed by improving the charge separation efficiency at the interactions of the g-C₃N₄/TNBTs heterostructures in Fig. 11. The standard redox potential of $\text{O}_2/\cdot\text{O}_2^-$ (-0.33 eV) (Li et al., 2019b) is more negative than the E_{CB} of TiO₂, indicating that the e^- can hardly react with O_2 to produce $\cdot\text{O}_2^-$. However, the results of radical species trapping demonstrate that $\cdot\text{O}_2^-$ is the main active species in photocatalytic degradation. Therefore, we can speculate that the g-C₃N₄/TNBTs photoelectrodes is a Z-scheme mechanism.

In theory, g-C₃N₄ has stronger reductive ability due to its more negative reductive potential (-1.13 eV) and TiO₂ has stronger oxidation ability owing to its high positive oxidation potential (2.91 eV). Under light irradiation, all-soild Z-scheme g-C₃N₄/TNBTs heterostructure could be excited and generated electron-hole pairs. Driven by internal electric field, the electrons on the CB of

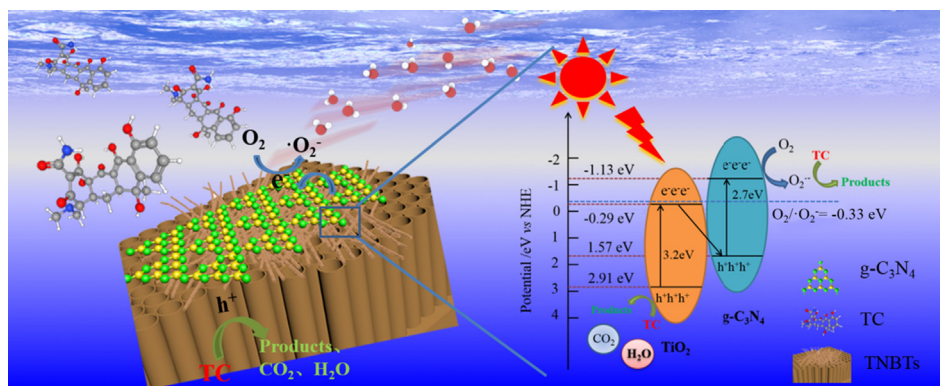
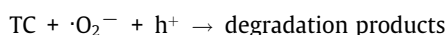
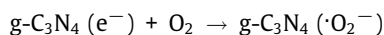
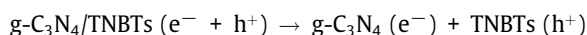
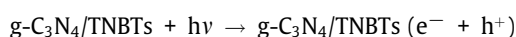


Fig. 11. Schematic illustration of possible charge transfer and photocatalytic mechanism of $g\text{-C}_3\text{N}_4/\text{TNBTs}$ photoelectrodes.

TiO_2 could transfer easily to the VB of $g\text{-C}_3\text{N}_4$ and recombine with the holes for the VB edge of $g\text{-C}_3\text{N}_4$ (1.57 eV vs NHE) was lower than TiO_2 (2.91 eV vs NHE) (Wu et al., 2017). The migration of photo-induced carriers can lead to the accumulation of photogenerated electrons on the CB of $g\text{-C}_3\text{N}_4$ (-1.13 eV), and the h^+ retained on the VB of TiO_2 (2.91 eV), which effectively restrain the electron-hole recombination and preserves higher redox activity. In addition, both layered $g\text{-C}_3\text{N}_4$ nanosheets and netlike TNBTs can effectively improve the transfer of photogenerated electrons. Subsequently, the CB potential of $g\text{-C}_3\text{N}_4$ was more negative than the E^0 ($\text{O}_2/\cdot\text{O}_2^-$), resulting that the electrons on the CB of the $g\text{-C}_3\text{N}_4$ would combine with O_2 absorbed on the surface to generate $\cdot\text{O}_2^-$ (Hamal and Klabunde, 2011). Simultaneously, the h^+ were left on the VB of TiO_2 , which have enough energy to attack TC molecules directly. Therefore, $\cdot\text{O}_2^-$ and h^+ might involve in the photocatalytic decomposition of TC to generate intermediates, which were finally mineralized into CO_2 and H_2O . The photocatalytic mechanism could be described as follows:



Generally, the photocatalytic reaction of $g\text{-C}_3\text{N}_4/\text{TNBTs}$ photoelectrodes adheres to all-solid Z-scheme $g\text{-C}_3\text{N}_4/\text{TNBTs}$ mechanism, which not only can further the separation photogenerated carriers and greatly prolong the lifetime of photogenerated electrons, but also possess higher photocatalytic efficiency for the degradation of TC.

4. Conclusion

Netlike 3D Z-scheme $g\text{-C}_3\text{N}_4/\text{TNBTs}$ photoelectrodes was successfully designed by anodization and coating technology. The as-prepared $g\text{-C}_3\text{N}_4/\text{TNBTs}$ photoelectrodes exhibited well 3D nanotube and 1D belt-like structure, and the wrinkled 2D $g\text{-C}_3\text{N}_4$ nanosheets were distributed over the netlike TNBTs. At the optimum $g\text{-C}_3\text{N}_4$ coating times, the $g\text{-C}_3\text{N}_4/\text{TNBTs}$ -3 netlike photoelectrodes exhibited an outstanding photocatalytic performance for TC degradation. The improved photocatalytic performance was because of that the network 3D Z-scheme $g\text{-C}_3\text{N}_4/\text{TNBTs}$ heterostructure improved utilization efficiency for sunlight, promoted the separation and interfacial transfer of photogenerated carrier, and could increase the attachment sites of TC molecules.

Under irradiation, A large number of electrons could transfer easily from the CB of TiO_2 to the VB of $g\text{-C}_3\text{N}_4$ and recombine with the h^+ . The photocatalytic decomposition of TC was turned out to be mainly oxidation process by the dominant active species of $\cdot\text{O}_2^-$ and h^+ based on radical trapping experiment. The network 3D Z-scheme $g\text{-C}_3\text{N}_4/\text{TNBTs}$ photoelectrodes could provide the design strategies for degradation of TC in the environment and a new viewpoint for photocatalytic mechanism of $g\text{-C}_3\text{N}_4/\text{TNBTs}$ photoelectrodes.

CRediT authorship contribution statement

Xiaohan Ma: Conceptualization, Methodology, Software, Investigation, Writing - original draft. **Qinghua Chen:** Validation, Formal analysis, Visualization, Software. **Guocheng Liu:** Validation, Formal analysis, Visualization. **Yuanming Zhou:** . **Dong Ma:** . **Shuaishuai Xin:** Writing - review & editing. **Chengze Yu:** . **Bin Zhang:** . **Yanjun Xin:** Resources, Writing - review & editing, Supervision, Data curation.

Declaration of Competing Interest

The authors declare that they have no known competing financial interests or personal relationships that could have appeared to influence the work reported in this paper.

Acknowledgements

This work is financially supported by National Natural Science Foundation of China (No. 51678323), Natural Science Foundation of Shandong Province (No. ZR2019MD012, ZR2017MEE026) and Support Plan on Youth Innovation Science and Technology for Higher Education of Shandong Province (No. 2019KJD014).

References

- Benjamin, H.M., Prashant, V.K., 2009. Got TiO_2 nanotubes? Lithium ion intercalation can boost their photoelectrochemical performance. *ACS Nano* 3, 3437–3446.
- Boonprakob, N., Wetchakun, N., Phanichphant, S., Waxler, D., Sherrell, P., Nattestad, A., Chen, J., Inceesungvorn, B., 2014. Enhanced visible-light photocatalytic activity of $g\text{-C}_3\text{N}_4/\text{TiO}_2$ films. *J. Colloid Interface Sci.* 417, 402–409.
- Brunetti, A., Pomilla, F.R., Marci, G., Garcia-Lopez, E.I., Fontananova, E., Palmisano, L., Barbieri, G., 2019. CO_2 reduction by $\text{C}_3\text{N}_4\text{-TiO}_2$ Nafion photocatalytic membrane reactor as a promising environmental pathway to solar fuels. *Environ. Appl. Catal. B*, 255.
- Cao, S., Low, J., Yu, J., Jaroniec, M., 2015. Polymeric photocatalysts based on graphitic carbon nitride. *Adv. Mater.* 27, 2150–2176.
- Cerdan, K., Ouyang, W., Colmenares, J.C., Muñoz-Batista, M.J., Luque, R., Balu, A.M., 2018. Facile mechanochemical modification of $g\text{-C}_3\text{N}_4$ for selective photo-oxidation of benzyl alcohol. *Chem. Eng. Sci.* 194, 78–84.

- Chen, B., Lin, L., Fang, L., Yang, Y., Chen, E., Yuan, K., Zou, S., Wang, X., Luan, T., 2018. Complex pollution of antibiotic resistance genes due to beta-lactam and aminoglycoside use in aquaculture farming. *Water Res.* 134, 200–208.
- Chen, Q., Liu, H., Xin, Y., Cheng, X., Li, J., 2013. Enhanced photoelectrochemical and photocatalytic performance of single-crystalline anatase TiO₂ (101) nanobelts arrays originating from nanotubes arrays. *Appl. Surf. Sci.* 264, 476–484.
- Chen, Q., Liu, H., Xin, Y., Cheng, X., 2014a. Coupling immobilized TiO₂ nanobelts and Au nanoparticles for enhanced photocatalytic and photoelectrocatalytic activity and mechanism insights. *Chem. Eng. J.* 241, 145–154.
- Chen, S., Hu, Y., Meng, S., Fu, X., 2014b. Study on the separation mechanisms of photogenerated electrons and holes for composite photocatalysts g-C₃N₄-WO₃. *Appl. Catal. B: Environ.* 150–151, 564–573.
- Chen, X., Liu, Q., Wu, Q., Du, P., Zhu, J., Dai, S., Yang, S., 2016. Incorporating graphitic carbon nitride (g-C₃N₄) quantum dots into bulk-heterojunction polymer solar cells leads to efficiency enhancement. *Adv. Funct. Mater.* 26, 1719–1728.
- Dong, G., Ho, W., Li, Y., Zhang, L., 2015. Facile synthesis of porous graphene-like carbon nitride (C₆N₉H₃) with excellent photocatalytic activity for NO removal. *Appl. Catal. B Environ.* 174–175, 477–485.
- Hamal, D.B., Klabunde, K.J., 2011. Valence state and catalytic role of cobalt ions in cobalt TiO₂ nanoparticle photocatalysts for acetaldehyde degradation under visible light. *J. Phys. Chem. C* 115, 17359–17367.
- Huang, Z., Sun, Q., Lv, K., Zhang, Z., Li, M., Li, B., 2015. Effect of contact interface between TiO₂ and g-C₃N₄ on the photoreactivity of g-C₃N₄/TiO₂ photocatalyst: (001) vs (101) facets of TiO₂. *Appl. Catal. B Environ.* 164, 420–427.
- Inoue, T., Fujishima, A., Konishi, S., Honda, K., 1979. Photoelectrocatalytic reduction of carbon dioxide in aqueous suspensions of semiconductor powders. *Nature* 277, 637–638.
- Jiang, L., Yuan, X., Zeng, G., Liang, J., Chen, X., Yu, H., Wang, H., Wu, Z., Zhang, J., Xiong, T., 2018. In-situ synthesis of direct solid-state dual Z-scheme WO₃/g-C₃N₄/Bi₂O₃ photocatalyst for the degradation of refractory pollutant. *Appl. Catal. B Environ.* 227, 376–385.
- Kumar, S., Surendar, T., Baruah, A., Shanker, V., 2013. Synthesis of a novel and stable g-C₃N₄-Ag₃PO₄ hybrid nanocomposite photocatalyst and study of the photocatalytic activity under visible light irradiation. *J. Mater. Chem. A* 1.
- Lakhera, S.K., Watts, A., Hafeez, H.Y., Neppolian, B., 2018. Interparticle double charge transfer mechanism of heterojunction α -Fe₂O₃/Cu₂O mixed oxide catalysts and its visible light photocatalytic activity. *Catal. Today* 300, 58–70.
- Lakshminarasimhan, N., Bae, E., Choi, W., 2007. Enhanced photocatalytic production of H₂ on mesoporous TiO₂ prepared by template-free method: role of interparticle charge transfer. *J. Phys. Chem. C* 111, 15244–15250.
- Li, C., Lou, Z., Yang, Y., Wang, Y., Lu, Y., Ye, Z., Zhu, L., 2019a. Hollowsphere nanoheterojunction of g-C₃N₄/TiO₂ with high visible light photocatalytic property. *Langmuir* 35, 779–786.
- Li, G., Nie, X., Gao, Y., An, T., 2016. Can environmental pharmaceuticals be photocatalytically degraded and completely mineralized in water using g-C₃N₄/TiO₂ under visible light irradiation?—Implications of persistent toxic intermediates. *Appl. Catal. B Environ.* 180, 726–732.
- Li, G., Wang, B., Zhang, J., Wang, R., Liu, H., 2019b. Rational construction of a direct Z-scheme g-C₃N₄/CdS photocatalyst with enhanced visible light photocatalytic activity and degradation of erythromycin and tetracycline. *Appl. Surf. Sci.* 478, 1056–1064.
- Li, J., Zhang, M., Li, Q., Yang, J., 2017. Enhanced visible light activity on direct contact Z-scheme g-C₃N₄-TiO₂ photocatalyst. *Appl. Surf. Sci.* 391, 184–193.
- Li, T., Zhao, L., He, Y., Cai, J., Luo, M., Lin, J., 2013. Synthesis of g-C₃N₄/SmVO₄ composite photocatalyst with improved visible light photocatalytic activities in RhB degradation. *Appl. Catal. B Environ.* 129, 255–263.
- Li, Y., Wang, J., Yang, Y., Zhang, Y., He, D., An, Q., Cao, G., 2015. Seed-induced growing various TiO₂ nanostructures on g-C₃N₄ nanosheets with much enhanced photocatalytic activity under visible light. *J. Hazard Mater.* 292, 79–89.
- Liao, G., Chen, S., Quan, X., Yu, H., Zhao, H., 2012. Graphene oxide modified g-C₃N₄ hybrid with enhanced photocatalytic capability under visible light irradiation. *J. Mater. Chem.* 22, 2721–2726.
- Liu, C., Dong, S., Chen, Y., 2019a. Enhancement of visible-light-driven photocatalytic activity of carbon plane/g-C₃N₄/TiO₂ nanocomposite by improving heterojunction contact. *Chem. Eng. J.* 371, 706–718.
- Liu, H., Zhang, Z., He, H., Wang, X., Zhang, J., Zhang, Q., Tong, Y., Liu, H., Ramakrishna, S., Yan, S., Long, Y., 2018. One-step synthesis heterostructured g-C₃N₄/TiO₂ composite for rapid degradation of pollutants in utilizing visible light. *Nanomaterials* 8, 842.
- Liu, J., Zhang, T., Wang, Z., Dawson, G., Chen, W., 2011. Simple pyrolysis of urea into graphitic carbon nitride with recyclable adsorption and photocatalytic activity. *J. Mater. Chem.* 21.
- Liu, L., Zhang, G., Irvine, J.T.S., Wu, Y., 2015. Organic semiconductor g-C₃N₄ modified TiO₂ nanotube arrays for enhanced photoelectrochemical performance in wastewater treatment. *Energy Technol.* 3, 982–988.
- Liu, Y., Zeng, X., Hu, X., Hu, J., Wang, Z., Yin, Y., Sun, C., Zhang, X., 2019b. Two-dimensional g-C₃N₄/TiO₂ nanocomposites as vertical Z-scheme heterojunction for improved photocatalytic water disinfection. *Catal. Today* 335, 243–251.
- Lu, L., Wang, G., Zou, M., Wang, J., Li, J., 2018. Effects of calcining temperature on formation of hierarchical TiO₂/g-C₃N₄ hybrids as an effective Z-scheme heterojunction photocatalyst. *Appl. Surf. Sci.* 441, 1012–1023.
- Lu, Z., Zeng, L., Song, W., Qin, Z., Zeng, D., Xie, C., 2017. In situ synthesis of C-TiO₂/g-C₃N₄ heterojunction nanocomposite as highly visible light active photocatalyst originated from effective interfacial charge transfer. *Appl. Catal. B Environ.* 202, 489–499.
- Ma, D., Wu, J., Gao, M., Xin, Y., Ma, T., Sun, Y., 2016. Fabrication of Z-scheme g-C₃N₄/RGO/Bi₂WO₆ photocatalyst with enhanced visible-light photocatalytic activity. *Chem. Eng. J.* 290, 136–146.
- Mishra, A., Mehta, A., Kainth, S., Basu, S., 2018. A comparative study on the effect of different precursors for synthesis and efficient photocatalytic activity of g-C₃N₄/TiO₂/bentonite nanocomposites. *J. Mater. Sci.* 53, 13126–13142.
- Mohanan, D., Sumina, N.B., Thomas, R.T., Mohamed, A.P., Hareesh, U.S., Ray, A.K., Pillai, S., 2019. Cucurbit[7]uril encapsulated dye-sensitized enhanced solar photocatalysis using positively charged sheet-like anatase TiO₂ mesocrystals. *Appl. Surf. Sci.* 488, 911–920.
- Mor, G.K., Shankar, K., Paulose, M., Varghese, O.K., Grimes, C.A., 2006. Use of highly-ordered TiO₂ nanotube arrays in dye-sensitized solar cells. *Nano Lett.* 6, 215–218.
- Moreira, J., Serrano, B., Ortiz, A., Lasa, H.D., 2012. A unified kinetic model for phenol photocatalytic degradation over TiO₂ photocatalysts. *Chem. Eng. Sci.* 78, 186–203.
- Roy, K., Agarkoti, C., Malani, R.S., Thokchom, B., Moholkar, V.S., 2020. Mechanistic study of sulfadiazine degradation by ultrasound-assisted fenton-persulfate system using yolk-shell Fe₃O₄@hollow@mSiO₂ nanoparticles. *Chem. Eng. Sci.* 217.
- Schlexer, P., Widmann, D., Behm, R.J., Pacchioni, G., 2018. CO oxidation on a Au/TiO₂ nanoparticle catalyst via the Au-assisted mars-van krevelen mechanism. *ACS Catal.* 8, 6513–6525.
- She, H., Li, L., Sun, Y., Wang, L., Huang, J., Zhu, G., Wang, Q., 2018. Facile preparation of mixed-phase CdS and its enhanced photocatalytic selective oxidation of benzyl alcohol under visible light irradiation. *Appl. Surf. Sci.* 457, 1167–1173.
- Sheng, Y., Wei, Z., Miao, H., Yao, W., Li, H., Zhu, Y., 2019. Enhanced organic pollutant photodegradation via adsorption/photocatalysis synergy using a 3D g-C₃N₄/TiO₂ free-separation photocatalyst. *Chem. Eng. J.* 370, 287–294.
- Sridharan, K., Jang, E., Park, T.J., 2013. Novel visible light active graphitic C₃N₄-TiO₂ composite photocatalyst: synergistic synthesis, growth and photocatalytic treatment of hazardous pollutants. *Appl. Catal. B Environ.* 142–143, 718–728.
- Su, J., Zhu, L., Chen, G., 2016. Ultrasmall graphitic carbon nitride quantum dots decorated self-organized TiO₂ nanotube arrays with highly efficient photoelectrochemical activity. *Appl. Catal. B Environ.* 186, 127–135.
- Tan, A.W., Pingguan-Murphy, B., Ahmad, R., Akbar, S.A., 2013. Advances in fabrication of TiO₂ nanofiber/nanowire arrays toward the cellular response in biomedical implantations: a review. *J. Mater. Sci.* 48, 8337–8353.
- Tan, Y., Zhu, S., Zhou, J., Li, T., Zhao, Z., 2018. One-step synthesis of nanostructured g-C₃N₄/TiO₂ composite for highly enhanced visible-light photocatalytic H₂ evolution. *Appl. Catal. B Environ.* 230, 260–268.
- Turolla, A., Bestetti, M., Antonelli, M., 2018. Optimization of heterogeneous photoelectrocatalysis on nanotubular TiO₂ electrodes: Reactor configuration and kinetic modelling. *Chem. Eng. Sci.* 182, 171–179.
- Wang, G., Chen, Q., Liu, Y., Ma, D., Xin, Y., Ma, X., Zhang, X., 2018a. In situ synthesis of graphene/WO₃ co-decorated TiO₂ nanotube array photoelectrodes with enhanced photocatalytic activity and degradation mechanism for dimethyl phthalate. *Chem. Eng. J.* 337, 322–332.
- Wang, H., Yuan, X., Wu, Y., Zeng, G., Chen, X., Leng, L., Li, H., 2015. Synthesis and applications of novel graphitic carbon nitride/metal-organic frameworks mesoporous photocatalyst for dyes removal. *Appl. Catal. B Environ.* 174–175, 445–454.
- Wang, H., Liang, Y., Liu, L., Hu, J., Cui, W., 2018b. Highly ordered TiO₂ nanotube arrays wrapped with g-C₃N₄ nanoparticles for efficient charge separation and increased photoelectrocatalytic degradation of phenol. *J. Hazard Mater.* 344, 369–380.
- Wang, H., Zhu, W., Chong, B., Qin, K., 2014. Improvement of photocatalytic hydrogen generation from CdSe/CdS/TiO₂ nanotube-array coaxial heterogeneous structure. *Int. J. Hydrogen Energy* 39, 90–99.
- Wang, J., Wang, G., Wang, X., Wu, Y., Su, Y., Tang, H., 2019a. 3D/2D direct Z-scheme heterojunctions of hierarchical TiO₂ microflowers/g-C₃N₄ nanosheets with enhanced charge carrier separation for photocatalytic H₂ evolution. *Carbon* 149, 618–626.
- Wang, J., Zhang, W., 2012. Modification of TiO₂ nanorod arrays by graphite-like C₃N₄ with high visible light photoelectrochemical activity. *Electrochim. Acta* 71, 10–16.
- Wang, Q., Li, X., Yang, Q., Chen, Y., Du, B., 2019b. Evolution of microbial community and drug resistance during enrichment of tetracycline-degrading bacteria. *Ecotoxicol. Environ. Saf.* 171, 746–752.
- Wang, X., Maeda, K., Thomas, A., Takanabe, K., Xin, G., Carlsson, J., Domen, K., Antonietti, M., 2009. A metal-free polymeric photocatalyst for hydrogen production from water under visible light. *Nat. Mater.* 8, 76–80.
- Wen, Y., Fan, H., Ning, L., Wang, C., Hu, B., Ma, J., Wang, W., Cui, K., 2018. Graphitic carbon nitride nanosheets prepared by gaseous molecules assembling for enhanced photocatalytic performance. *J. Mater. Sci.* 54, 1462–1474.
- Wu, F., Xin, L., Wei, L., Zhang, S., 2017. Highly enhanced photocatalytic degradation of methylene blue over the indirect all-solid-state Z-scheme g-C₃N₄-RGO-TiO₂ nanoheterojunctions. *Appl. Surf. Sci.* 405, 60–70.
- Wu, K., Qin, Z., Zhang, X., Guo, R., Ren, X., Pu, X., 2019a. Z-scheme BiOCl/Bi-Bi₂O₃ heterojunction with oxygen vacancy for excellent degradation performance of antibiotics and dyes. *J. Mater. Sci.* 55, 4017–4029.
- Wu, M., Leung, Y., Zhang, Y., Huang, H., Xie, R., Szeto, W., Li, F., 2019b. Toluene degradation over Mn-TiO₂/CeO₂ composite catalyst under vacuum ultraviolet (VUV) irradiation. *Chem. Eng. Sci.* 195, 985–994.
- Xue, J., Li, X., Ma, S., Xu, P., Wang, M., Ye, Z., 2018. Facile fabrication of BiOCl/RGO/protonated g-C₃N₄ ternary nanocomposite as Z-scheme photocatalyst for

- tetracycline degradation and benzyl alcohol oxidation. *J. Mater. Sci.* 54, 1275–1290.
- Yang, Q., Peng, P., Xiang, Z., 2017. Covalent organic polymer modified TiO₂ nanosheets as highly efficient photocatalysts for hydrogen generation. *Chem. Eng. Sci.* 162, 33–40.
- Ye, L., Liu, J., Gong, C., Tian, L., Peng, T., Zan, L., 2012. Two different roles of metallic Ag on Ag/AgX/BiOX (X = Cl, Br) visible light photocatalysts: surface plasmon resonance and Z-Scheme bridge. *ACS Catal.* 2, 1677–1683.
- Yu, F., Chen, Y., Pan, Y., Yang, Y., Ma, H., 2020. A cost-effective production of hydrogen peroxide via improved mass transfer of oxygen for electro-Fenton process using the vertical flow reactor. *Sep. Purif. Technol.*, 241
- Yu, J., Wang, S., Low, J., Xiao, W., 2013. Enhanced photocatalytic performance of direct Z-scheme g-C₃N₄-TiO₂ photocatalysts for the decomposition of formaldehyde in air. *Phys. Chem. Chem. Phys.* 15, 16883–16890.
- Zhai, C., Zhu, M., Lu, Y., Ren, F., Wang, C., Du, Y., Yang, P., 2014. Reduced graphene oxide modified highly ordered TiO₂ nanotube arrays photoelectrode with enhanced photoelectrocatalytic performance under visible-light irradiation. *Phys. Chem. Chem. Phys.* 16, 14800–14807.
- Zhang, C., Zhou, Y., Bao, J., Fang, J., Zhao, S., Zhang, Y., Sheng, X., Chen, W., 2018a. Structure regulation of ZnS@g-C₃N₄/TiO₂ nanospheres for efficient photocatalytic H₂ production under visible-light irradiation. *Chem. Eng. J.* 346, 226–237.
- Zhang, J.-J., Fang, S.-S., Mei, J.-Y., Zheng, G.-P., Zheng, X.-C., Guan, X.-X., 2018b. High-efficiency removal of rhodamine B dye in water using g-C₃N₄ and TiO₂ co-hybridized 3D graphene aerogel composites. *Sep. Purif. Technol.* 194, 96–103.
- Zhang, L., He, X., Xu, X., Liu, C., Duan, Y., Hou, L., Zhou, Q., Ma, C., Yang, X., Liu, R., Yang, F., Cui, L., Xu, C., Li, Y., 2017. Highly active TiO₂/g-C₃N₄/G photocatalyst with extended spectral response towards selective reduction of nitrobenzene. *Appl. Catal. B Environ.* 203, 1–8.
- Zhang, Q., Yang, F., Zhou, S., Bao, N., Xu, Z., Chaker, M., Ma, D., 2020. Broadband photocatalysts enabled by 0D/2D heterojunctions of near-infrared quantum dots/graphitic carbon nitride nanosheets. *Appl. Catal. B Environ.* 270, 118879.
- Zhang, Y., Liu, J., Wu, G., Chen, W., 2012. Porous graphitic carbon nitride synthesized via direct polymerization of urea for efficient sunlight-driven photocatalytic hydrogen production. *Nanoscale* 4, 5300–5303.
- Zhao, H., Chen, X.L., Jia, C., Zhou, T., Qu, X., Jian, J., Xu, Y., Zhou, T., 2005. A facile mechanochemical way to prepare g-C₃N₄. *Mater. Sci. Eng. B* 122, 226–230.
- Zhao, H., Cui, S., Yang, L., Li, G., Li, N., Li, X., 2018. Synthesis of hierarchically meso-macroporous TiO₂/CdS heterojunction photocatalysts with excellent visible-light photocatalytic activity. *J. Colloid Interf. Sci.* 512, 47–54.
- Zhao, R., Sun, X., Jin, Y., Han, J., Wang, L., Liu, F., 2019. Au/Pd/g-C₃N₄ nanocomposites for photocatalytic degradation of tetracycline hydrochloride. *J. Mater. Sci.* 54, 5445–5456.
- Zhou, D., Chen, Z., Yang, Q., Dong, X., Zhang, J., Qin, L., 2016. In-situ construction of all-solid-state Z-scheme g-C₃N₄/TiO₂ nanotube arrays photocatalyst with enhanced visible-light-induced properties. *Sol. Energy Mater. Sol. Cells* 157, 399–405.
- Zhou, F., Yan, C., Liang, T., Sun, Q., Wang, H., 2018. Photocatalytic degradation of orange G using sepiolite-TiO₂ nanocomposites: Optimization of physicochemical parameters and kinetics studies. *Chem. Eng. Sci.* 183, 231–239.
- Zhou, J., Yang, Y., Zhang, C.Y., 2013. A low-temperature solid-phase method to synthesize highly fluorescent carbon nitride dots with tunable emission. *Chem. Commun.* 49, 8605–8607.
- Zhou, P., Yu, J., Jaroniec, M., 2014. All-solid-state Z-scheme photocatalytic systems. *Adv. Mater.* 26, 4920–4935.
- Zhu, H., Yang, B., Xu, J., 2009. Construction of Z-scheme type CdS–Au–TiO₂ hollow nanorod arrays with enhanced photocatalytic activity. *Appl. Catal. B Environ.* 90, 463–469.

编号: 2020-608

检索证明报告

论文作者: 张彬

作者单位: 青岛农业大学

论文发表年限: 2020

检索数据库:

《科学引文索引》(SCI-EXPANDED1986-2020)

检索方式: 网络检索

检索要求: SCI 收录、期刊影响因子及分区

检索结果:

经检索, 张彬同志提交的 2 篇论文在 2020 年被 SCI 收录。(详见附件)

特此证明!

检索证明人: 苏雯雯

教育部科技查新工作站

2020-8-25



一、SCI 收录情况、期刊影响因子及分区

第 1 条, 共 2 条

标题: Fabrication of rGO and g-C(3)N(4) co-modified TiO₂ nanotube arrays photoelectrodes with enhanced photocatalytic performance

作者: Zhang, B (Zhang, Bin); Ma, XH (Ma, Xiaohan); Ma, J (Ma, Jun); Zhou, YM (Zhou, Yuanming); Liu, GC (Liu, Guocheng); Ma, D (Ma, Dong); Deng, ZH (Deng, Zhihan); Luo, MM (Luo, Mingming); Xin, YJ (Xin, Yanjun)

来源出版物: JOURNAL OF COLLOID AND INTERFACE

SCIENCE 卷: 577 页: 75-85 DOI: 10.1016/j.jcis.2020.05.031 出版年: OCT 1 2020

入藏号: WOS:000556588700010

PubMed ID: 32473478

地址: [Zhang, Bin; Ma, Xiaohan; Ma, Jun; Liu, Guocheng; Ma, Dong; Xin, Yanjun] Qingdao Agr Univ, Coll Resource & Environm, Qingdao Engr Res Ctr Rural Environm, Qingdao 266109, Peoples R China.

[Zhang, Bin; Ma, Jun] Harbin Inst Technol, State Key Lab Urban Water Resource & Environm, Harbin 150090, Peoples R China.

[Zhou, Yuanming] Qingdao Agr Univ, Cent Lab, Qingdao 266109, Peoples R China.

[Deng, Zhihan] Qingdao Agr Univ, Financial Dept, Qingdao 266109, Peoples R China.

[Luo, Mingming] Qingdao Agr Univ, Construct Engr Coll, Qingdao 266109, Peoples R China.

通讯作者地址: Xin, YJ (corresponding author), Qingdao Agr Univ, Coll Resource & Environm, Qingdao Engr Res Ctr Rural Environm, Qingdao 266109, Peoples R China.

电子邮件地址: xintom2000@126.com

ISSN: 0021-9797

eISSN: 1095-7103

impact factor

7.489 6.171

2019 5 年

JCR® 类别	类别中的排序	JCR 分区
CHEMISTRY, PHYSICAL	31/159	Q1

第 2 条, 共 2 条

标题: In situ synthesis of ultrafine TiO₂ nanoparticles modified g-C₃N₄ heterojunction photocatalyst with enhanced photocatalytic activity

作者: Zhang, B (Zhang, Bin); He, X (He, Xu); Ma, XH (Ma, Xiaohan); Chen, QH (Chen, Qinghua); Liu, GC (Liu, Guocheng); Zhou, YM (Zhou, Yuanming); Ma, D (Ma, Dong); Cui, CY (Cui, Chunyue); Ma, J (Ma, Jun); Xin, YJ (Xin, Yanjun)

来源出版物: SEPARATION AND PURIFICATION TECHNOLOGY 卷: 247 文献

号: 116932 DOI: 10.1016/j.seppur.2020.116932 出版年: SEP 15 2020

入藏号: WOS:000536142200046

地址: [Zhang, Bin; Ma, Xiaohan; Chen, Qinghua; Liu, Guocheng; Ma, Dong; Cui, Chunyue; Ma, Jun; Xin, Yanjun] Qingdao Agr Univ, Coll Resource & Environm, Qingdao Engr Res Ctr Rural Environm, Qingdao 266109, Peoples R China.

[Zhang, Bin; He, Xu; Ma, Jun] Harbin Inst Technol, State Key Lab Urban Water Resource & Environm, Harbin 150090, Peoples R China.

[Zhou, Yuanming] Qingdao Agr Univ, Cent Lab, Qingdao 266109, Peoples R China.

通讯作者地址: Xin, YJ (corresponding author), Qingdao Agr Univ, Coll Resource & Environm, Qingdao Engr Res Ctr Rural Environm, Qingdao 266109, Peoples R China.

电子邮件地址: xintom2000@126.com

ISSN: 1383-5866

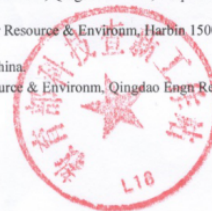
eISSN: 1873-3794

impact factor

5.774 5.257

2019 5 年

JCR® 类别	类别中的排序	JCR 分区
ENGINEERING, CHEMICAL	16/143	Q1



参研人员证明

兹证明张彬(身份证号: 372925199606078017 学号: 20182100074)同学参研国家自然科学基金面上项目《界面调控的 Z 型 TiO₂ 纳米管(带)阵列光电极构筑及协同氧化还原机制》, 并于 2018-2019 年期间承担进行了 rGO/g-C₃N₄/TiO₂ 纳米管阵列光电极的制备及其降解盐酸四环素机理的研究。

项目负责人:



青岛农业大学高层次人才科研基金

申 请 书

项目名称：不同粒径生物炭对水体抗生素环境行为的影响

项目负责人：刘国成

承担单位：资源与环境学院

起止时间：2019.6-2022.6

青岛农业大学科技处

填表日期： 2019年4月2日

一、基本信息：

申请者信息	姓名	刘国成	性别	男	出生年月	1985年3月
	学历/学位	研究生/博士	职称	副教授	主要研究领域	污染物的环境行为与控制
	电话	0532-86080571	手机	18563939539	E-mail	lg@qau.edu.cn
	毕业院校及专业	中国海洋大学/环境科学				
	单位(教研室)	资源与环境学院(环境科学教研室)				
项目基本信息	项目名称		不同粒径生物炭对水体抗生素环境行为的影响			
	所在学科		环境科学与工程			
	预计研究年限		3年			
	总预算经费		50万			

二、项目组主要成员：

编号	姓名	出生年月	职 称	学历/学位	项目分工
1	信帅帅	1990.11		博士研究生	生物炭的制备与表征
2	马小涵	1996.06		硕士研究生	不同粒径生物炭的特性差异
3	张彬	1996.06		硕士研究生	不同粒径生物炭对 ATs 的吸附特性
4	麻颖颖	1996.07		硕士研究生	不同粒径生物炭对 ATs 有效性的影响
摘要	<p>生物炭 (Biochar, BC) 在环境、农业和能源等方面具有良好应用前景。BC 在生产应用中可形成不同粒径颗粒, 其物化特性差异尚不明确, 在水体中的环境行为也尚未可知。项目通过机械/超声破损-静置/离心分离不同粒径 BC 颗粒, 研究其特性差异及在水环境中悬浮/沉降行为和稳定性。此外, 由于较大的比表面积和丰富的官能团, BC 对抗生素 (Antibiotics, ATs) 具有良好的吸附倾向。然而, 不同粒径 BC 对 ATs 吸附/解吸、迁移转化等行为的影响还少有报道。项目主要关注不同粒径 BC 对 ATs 的吸附特性, 重点探究其对 ATs 在水体中迁移转化的影响, 评估 ATs 生物有效性的变化。项目的开展将为评价 BC 环境风险和建立水体 ATs 污染的 BC 控制技术提供理论和数据支撑。</p>				
关键词 (用分号分开, 最多 5 个)			生物炭; 粒径; 抗生素; 吸附; 水体		

三、项目经费预算：

科目	预算金额（万元）	备注（计算依据与说明）
一、研究经费		
1.科研业务费		
（1）测试/计算/分析费	6.0	用于生物炭的特性表征，如元素分析、扫描透射电镜和X射线衍射分析等大型仪器的使用，共计6万元。
（2）能源/动力费	1.0	支付研究中水体、沉积物等样品的野外采集和试验所需电、燃油等能源动力费用，共计1万元。
（3）会议费/差旅费	7.2	参加学术会议、交流合作，3年×4次/年×0.6万元/次 = 7.2万元。
（4）出版物/文献/信息传播事务费	3.8	发表SCI论文5篇，申请发明专利2项。英文润色、版面费2万元（5×0.4万元/篇），专利申请费用1.2万元（2×0.6万元/项），文献检索、资料打印0.6万元（3年×0.2万元/年），共计3.8万元。
2.实验材料费		
（1）原材料/试剂/药品购置费	18.0	购置抗生素标准品、DGT被动采样膜、聚四氟乙烯滤膜、离心管、防护手套等，共计18万元。
（2）其他		
3.仪器设备费		
（1）购置	14.0	购置奥豪斯十万分之一精密天平5万元（精度0.01mg），Fisher500W超声破碎仪3.5万元，超纯水机4万元，恒温培养箱1.5万元。
（2）试制		
4.实验室改装费		
5.协作费		
6.其他		
二、国际合作与交流费		
1.项目组成员出国合作交流		
2.境外专家来华合作交流		
三、劳务费		
四、其他		
合计	50.0	

申请书正文

一、项目的立项依据、目的和意义（1000-2000字）

生物炭（biochar, BC）是废弃生物质在无氧或限氧条件下热解得到的多孔性、富碳的固态材料^[1]。近年来, BC 引起了国内外环境、农业、气候等领域科研工作者广泛的关注^[2-4]。BC 可实现碳封存, 减少土壤中 N₂O 等温室气体的排放, 缓解温室效应^[2, 5]; 改善土壤质地和肥力, 提高生产力^[6]; 吸附固持重金属和有机污染物, 降低污染物环境风险^[7-9]。BC 已成为具有固碳减排、土壤改良和污染物控制等多重功效的环境友好型材料。

BC 生产时, 一般需要经破碎工艺使颗粒粒径适宜^[10]。作土壤改良剂时, 多选择粒径小于 2 mm 的 BC^[6, 11]; 作污染物吸附剂时, BC 粒径多小于 125 μm^[7-9]。BC 破碎时, 可产生不同粒径的颗粒, 一般包括大颗粒 (Bulk BC, mm) 和小颗粒 (Dust-sized BC, μm), 甚至纳米颗粒 (Nano BC, nm)^[12]。不同破碎强度、时间决定了 BC 粒径分布。另外, 土壤中 BC 可经风化、磨损、湿润与干燥循环及微生物作用发生物理分解, 粒径减小, 也可形成纳米级 BC^[13, 14]。那么, 生产、应用中形成的不同粒径 BC 的物化特性是否存在差异? 其在水体中的环境行为又有何不同? 此研究对于深入开发 BC 的应用潜力及评价 BC 的环境风险至关重要。

目前, 我国环境污染问题日益突出。环境中抗生素 (Antibiotics, ATs) 污染日渐受到关注^[15, 16]。水体是 ATs 最重要的归宿地之一, 污水、地表水甚至地下水中均检测到了 ATs, 浓度范围为 ng L⁻¹ 至 μg L⁻¹^[16]。ATs 及其经水解、光解、生物降解等转化的代谢产物^[17], 可影响水环境中微生物, 水生植物、动物的种群结构, 破坏生态平衡。ATs 还会诱导病原菌产生耐药性, 对植物和动物产生生态毒性效应, 最终威胁人类健康。ATs 污染日趋显著, 水环境中 ATs 控制已刻不容缓。BC 对有机污染物有着良好的吸附性能^[18], 可以降低其在水体或土壤的生物有效性。不同粒径 BC 可通过地表径流、土壤淋失及在风的作用下进入水环境^[10, 19, 20]。BC 粒径的不同可能导致悬浮/沉降行为的差异, 对 ATs 产生不同的吸附/解吸行为, 进而影响 ATs 在水相、悬浮物和沉积物中的分配迁移, 最终改变 ATs 的生物有效性。因此, 研究不同粒径 BC 存在下, 水体中 ATs 的吸附、解吸、迁移、转化等环境行为, 将为 BC 在污染物控制中的成功应用提供重要的理论和技术支撑。

参考文献

- [1] Lehmann, J., et al., Biochar for environmental management: science and technology. London: Earthscan. 2009.
- [2] Lehmann, J., A handful of carbon. Nature. 2007. 447, 143-144.
- [3] Lehmann, J., Black Is The New Green. Nature. 2006. 442, 624-626.
- [4] Sutherland, W., et al., A horizon scan of global conservation issues for 2010. Trends in Ecology & Evolution. 2009. 25. 1-7.
- [5] Wang, Z., et al., Characterization and influence of biochars on nitrous oxide emission from

agricultural soil. *Environmental Pollution*, 2013. 174, 289-296.

[6] Zheng, H., et al., Impacts of adding biochar on nitrogen retention and bioavailability in agricultural soil. *Geoderma*, 2013. 206, 32-39.

[7] Liu G., et al., Adsorption characteristics and mechanisms of microcystin-LR by giant reed-derived biochars: Role of minerals, pores, and functional groups. *Journal of Cleaner Production*, 2018, 176, 463-473.

[8] Wang, Z., et al., Investigating the mechanisms of biochar's removal of lead from solution. *Bioresource Technology*, 2015.177, 308-317.

[9] 王震宇 等, 不同热解温度生物炭对 Cd(II)的吸附特性. *环境科学*. 2014. 35, 4735-4744.

[10] Gao, X. and Wu, H. Aerodynamic Properties of Biochar Particles: Effect of Grinding and Implications. *Environmental Science Technology Letters*, 2013. 1, 60-64.

[11] Vithanage, M., et al., Sorption and transport of sulfamethazine in agricultural soils amended with invasive-plant-derived biochar. *Journal of Environmental Management*, 2014.141, 95-103.

[12] Kim, W.K., et al., Characterization of cadmium removal from aqueous solution by biochar produced from a giant *Miscanthus* at different pyrolytic temperatures. *Bioresource Technology*, 2013.138, 266-270.

[13] Spokas, K.A., et al., Physical Disintegration of Biochar: An Overlooked Process. *Environmental Science Technology Letters*, 2014. 1, 326-332.

[14] Liu G., et al., Formation and physicochemical characteristics of nano biochar: Insight into chemical and colloidal stability. *Environmental Science and Technology*. 2018, 52, 10369-10379;

[15] 王敏和唐景春. 土壤中的抗生素污染及其生态毒性研究进展. *农业环境科学学报*, 2010. 29, 261-266.

[16] 章强 等. 中国主要水域抗生素污染现状及其生态环境效应研究进展. *环境化学*, 2014. 7, 1075-1083.

[17] Jia, A., et al., Occurrence and source apportionment of sulfonamides and their metabolites in Liaodong Bay and the adjacent Liao River basin, North China. *Environmental Toxicology and Chemistry*, 2011. 30,1252-1260.

[18] Kookana, R.S., The role of biochar in modifying the environmental fate, bioavailability, and efficacy of pesticides in soils: a review. *Australian Journal of Soil Research*, 2010. 48,627-637.

[19] Wang, D., et al., Transport of Biochar Particles in Saturated Granular Media: Effects of Pyrolysis Temperature and Particle Size. *Environmental Science Technology*, 2012. 47, 821-828.

[20] Wang, D., et al., Antagonistic Effects of Humic Acid and Iron Oxyhydroxide Grain-Coating on Biochar Nanoparticle Transport in Saturated Sand. *Environmental Science Technology*, 2013. 47, 5154-5161.

二、项目的研究内容、研究目标、拟解决的关键问题及特色创新之处（1000-1500 字）

1、研究内容：

(1) 不同粒径 BC 的制备和表征

- ① 农业废弃物和动物粪便在不同热解温度（300~700 ℃）下慢速热解制备 BC；
- ② 不同破损条件对 BC 粒径分布的影响，物理破损机制；
- ③ 不同粒径生物基本炭物化性质（比表面积、pH、含氧官能团等）的表征；
- ④ 不同粒径 BC 的化学稳定性；
- ⑤ 不同粒径 BC 在水环境中的悬浮沉降行为。

通过不同原料于不同热解温度下制备 BC，通过控制粉碎时间筛分不同粒径的 BC 颗粒，并表征其物理化学性质，研究不同生物质原料和不同热解温度对不同粒径 BC 产生的影响，揭示不同粒径 BC 基本物化性质的差异，探究其在水体中的悬浮沉降行为及化学稳定性，建立不同粒径的不同原料、不同热解温度 BC 的制备和表征体系。

(2) 不同粒径 BC 对水体中 ATs 环境行为的影响及内在机制

- ① 不同粒径 BC 对 ATs 的吸附、解吸；
- ② 不同粒径 BC 对 ATs 在水体环境介质分配的影响；
- ③ 不同粒径 BC 对 ATs 在水体中的水解、光降解和生物降解的影响；
- ④ 不同粒径 BC 对水体中 ATs 生物有效性的影响。

通过研究不同粒径的不同原料、不同热解温度 BC 对水体中对 ATs 的吸附、解吸特性，阐明不同类型 BC 物化性质与其对 ATs 吸附机制间的内在关系，为 BC 对水环境中 ATs 的迁移转化行为的影响提供理论基础；探究不同粒径的不同原料、不同热解温度 BC 对 ATs 在水、悬浮物和沉积物中的分配以及 ATs 的水解、光解和生物降解行为的影响，通过研究水生植物对 ATs 吸收、转运和转化的变化，为 BC 输入下水体环境中 ATs 生物有效性评估提供理论和数据支持。

2、研究目标

拟通过不同类型生物质原料于不同热解温度下制备 BC，并破碎分离不同粒径的 BC 颗粒，研究不同粒径 BC 物化特性差异及其在水环境中的悬浮沉降行为和稳定性；同时研究不同粒径 BC 对典型 ATs（如四环素类（TCs）和磺胺类抗生素（SAs））的吸附、解吸行为并揭示其内在机制，重点研究 BC 对水体中 ATs 水解、光降解及生物降解行为的影响，评估 ATs 生物有效性的变化，为最终建立适用于水体环境 ATs 污染的 BC 控制技术提供支撑，为

BC 环境风险评价提供数据支持。

3、拟解决的关键问题

- (1) 生物质原料和热解温度对 BC 颗粒物理破损的影响？
- (2) 不同粒径 BC 的表面化学特性及在水体环境中的悬浮沉降行为及碳质稳定性如何？
- (3) 不同粒径 BC 对水体中典型 ATs 的吸附、解吸如何？对 ATs 在水、悬浮物和沉积物中分配的影响如何？ATs 的转化、降解是促进还是抑制？ATs 的生物有效性是增强还是减弱？

4、特色创新之处

- (1) 研究物理破损对 BC 颗粒粒径和物化特性的影响；
- (2) 研究不同粒径 BC 碳质稳定性和在水环境中的悬浮/沉降、归趋；
- (3) 研究不同粒径 BC 对 ATs 在水环境中的吸附/解吸、迁移、转化等环境行为及生物有效性的影响。

三、项目的主要研究方法、技术路线及达到的技术经济指标（1500-2000 字）

1、主要研究方法

(1) 不同粒径 BC 的制备与表征

① 不同粒径 BC 的制备：拟采用常见且来源广泛的农业废弃物（花生壳、棉花秸秆）和动物粪便（鸡粪、牛粪）作为热解制备 BC 的生物质原料。称取一定量的生物质原料于刚玉管中，置于 300~700 ℃ 的管式炉中，在氮气保护环境下炭化 2 h。经自然冷却至室温后取出，称重计算产率。BC 经不同粉碎时间破碎后，一部分于旋振筛中分离出不同粒径的 BC 大颗粒，一部分通过超声离心分离法获得微米、纳米 BC 颗粒。微米和纳米 BC 样品经冷冻干燥后，储存于干燥皿备用。

② BC 的特性表征：利用 pH 计测定 BC 悬浊液的 pH 值；以高温灼烧法测定 BC 的灰分含量；利用元素分析仪分析 BC 的 C、H、N、O 元素含量；利用 X 射线光电子能谱（XPS）分析 BC 表面元素含量；利用物理化学吸附仪（Autosorb-IQ）分析 BC 比表面积和孔径分布；利用傅里叶转换红外光谱仪（FTIR）、固体核磁共振（¹³C-NMR）测定 BC 表面官能团；利用 X 射线衍射仪（XRD）测定 BC 矿物组分的晶相；电子扫描显微镜（SEM）和电子透射显微镜（TEM）观察 BC 表面和内部结构特征；采用 Zeta 电位分析仪测定 BC 表面电荷；以 H₂O₂ 和 K₂Cr₂O₇ 氧化法测定不同粒径 BC 的化学稳定性，通过 FTIR 测定 BC 氧化前后表面官能团的变化，利用 XPS 分析氧化对 BC 表面元素的影响，以 SEM 和 TEM 观察氧化对 BC 表面和内部结构的影响；利用静置沉降法表征不同粒径 BC 在水体中的沉降过程，在不同阳离子种类、不同离子强度和不同 DOM 种类、浓度下，利用激光粒度分析仪分析胶体颗粒 BC 在溶液中粒径变化及悬浮稳定性。

(2) 不同粒径 BC 对水体中 ATs 环境行为及生物有效性的影响

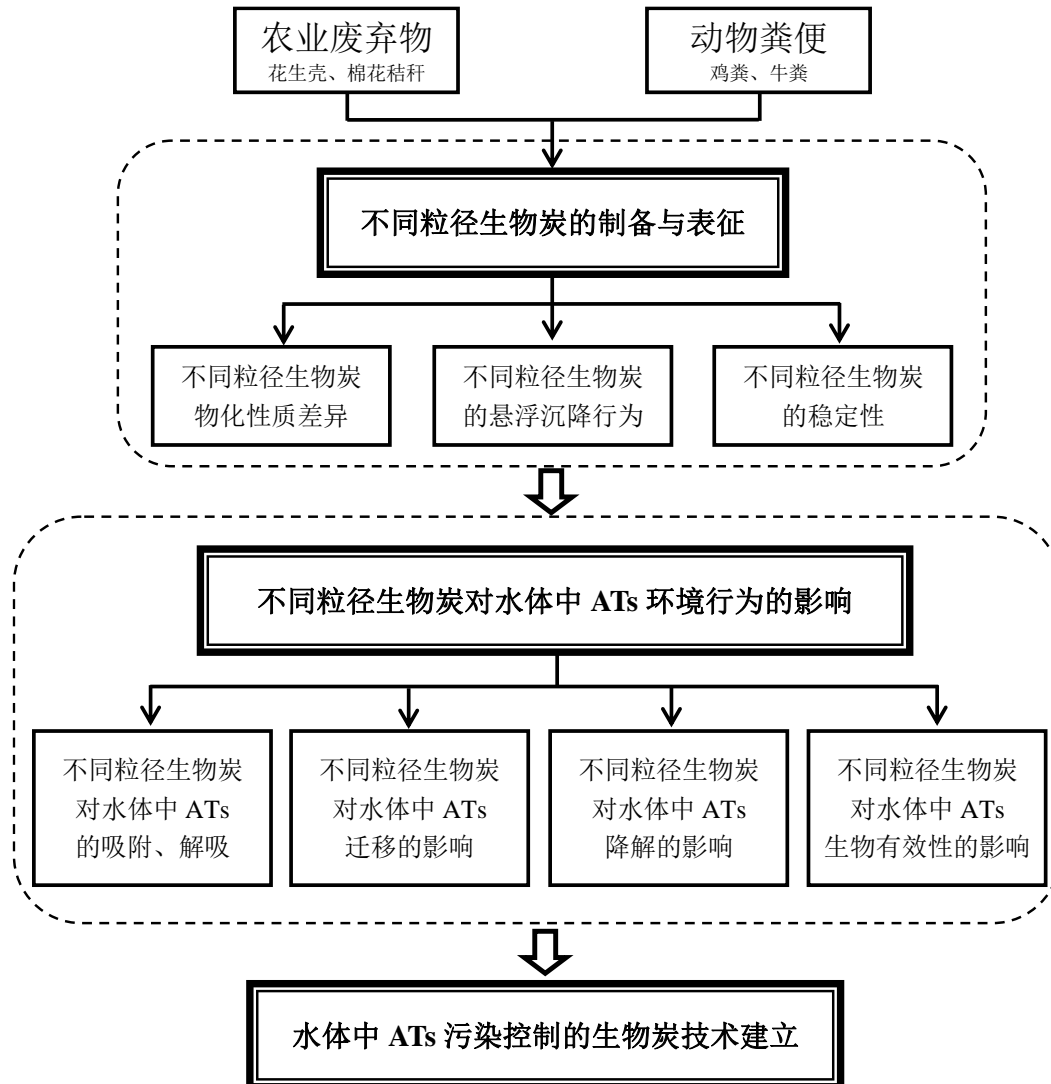
供试 ATs 选择 TCs 和 SAs 为典型代表，分别为四环素(TC)、土霉素(OTC)、金霉素(CTC) 和磺胺甲恶唑（SMX）、磺胺甲嘧啶（SMZ）、磺胺嘧啶（SPY）。

模拟水体环境条件（pH、离子强度），利用平衡吸附/解吸法测定不同粒径的不同原料、不同热解温度 BC 对 TCs 和 SAs 的吸附系数 K_{oc} 值；根据所选择的 ATs 在水相中的平衡浓度（ C_w ）和 BC 有机质固相上的含量（ C_s ）及有机碳含量（ f_{oc} ），计算其 K_{oc} 值（ $K_{oc}=C_s/(C_w f_{oc})$ ），并与理论的 K_{ow} 、溶解度和经验估计的 K_{oc} 值比较，评估不同粒径 BC 对所选 ATs 的吸附潜力，筛选出具有高效吸附能力的 BC。统计分析 K_{oc} 与不同粒径 BC 的比表面积、含氧官能团种类、数量及芳香性等特性间的相互关系，并采用 Autosorb-IQ、XPS、FTIR、NMR 等测定吸附前后 BC 比表面积、空隙结构和表面含氧官能团的变化，确定不同粒径 BC 对 ATs 吸附的内在机制。

于模拟水体环境（pH、离子强度、DOM）中加入不同量的 BC 颗粒（0~100 mg L⁻¹），通过静置沉降和离心（依据斯托克斯定律）测定 ATs 在水相、胶体 BC 颗粒和沉降 BC 颗粒中的浓度，并计算 ATs 在这些环境介质中分配比例；不同比例的不同粒径 BC 输入下，测定溶液中 ATs 及其水解产物含量，分析环境因子（pH、离子强度、DOM）变化对 ATs 水解的影响；

室内控温模拟光照环境，测定溶液中 ATs 残留和降解产物种类、含量，分析不同粒径 BC 对水体中 ATs 光降解的影响；控温暗室环境，设置抑菌和未抑菌处理，测定不同粒径 BC 存在下水溶液中 ATs 和降解产物含量，探讨不同粒径 BC 对水体中 ATs 生物降解的影响；建立“水体-植物-BC”系统，选取浮萍、金鱼藻等典型水生植物，通过水培实验测定 ATs 在水体、BC 固相和植物根系、茎、叶等部位的含量，分析植物对 ATs 的吸收、转运和转化，评估 ATs 生物有效性的变化。

2、技术路线



3、达到的技术经济指标

项目实施后，将形成一套不同粒径的不同原料、热解温度 BC 的制备与表征体系，开发可高效吸附 ATs 的 BC 产品 2 个以上，评价不同粒径 BC 对水体环境中 ATs 迁移、转化等环境行为及生物有效性的影响，建立水体 ATs 污染控制的 BC 技术，发表 SCI 论文 5 篇及以上。

四、现有的工作基础（500-1000 字）

本研究以不同的生物质原料于不同热解温度下制备 BC，通过破碎分离不同粒径的 BC 颗粒，研究不同粒径 BC 特性差异及其在水体环境中的悬浮沉降行为和稳定性，探究不同粒径 BC 对水体中 ATs 的吸附、解吸和迁移转化等环境行为及生物有效性的影响，思路可行。从 2010 年开始，申请人在 BC 制备与表征及 BC 对污染物控制等方面开展了大量探索性工作，积累了丰富的经验，于《Environmental Science and Technology》、《Journal of Cleaner Production》等国内外环境领域权威期刊上发表文章 15 篇。其中，以第一作者或通讯作者身份发表 SCI 收录论文 6 篇，6 篇 SCI 论文影响因子均大于 4.0，2 篇一区 SCI 论文的影响因子大于 5.5，总影响因子大于 25；共计 10 余次参加国际、国内会议，发表多篇 EI 收录会议论文。申请人博士生导师王震宇（江南大学环境与土木工程学院教授，环境污染过程与控制研究所所长，2006 年教育部“新世纪优秀人才”，2013 年国家自然科学基金委员会杰出青年基金获得者，2014 年山东省有突出贡献中青年专家）和博士后合作导师邢宝山（美国麻省大学终身教授，中国海洋大学教授，环境科学与工程、土壤化学领域专家，国家自然科学基金“海外杰青”，教育部“长江学者”奖励计划讲座教授，教育部“海外名师”，全球“环境与生态”领域 TOP 0.1% 科学家）将为项目提供有力的指导，确保本项目的研究方向紧扣国际前沿。另外，申请人所在资源与环境学院拥有研究所需的高效液相色谱、TOC 分析仪、离子色谱仪和物理化学吸附分析仪等大型仪器，透射/扫描电镜（TEM/SEM）、ICP-MS、液相色谱-质谱联用（HPLC-MS）等相关大型仪器可利用学校大型仪器共享平台；博士、博士后期间，申请人与中国科学院青岛生物能源与过程研究所分析测试中心杨春鹏、燕晓飞等老师已建立了良好的科研合作关系，可以利用其大型仪器共享平台开展原子力显微镜（AFM）、X 射线衍射仪（XRD）、固体核磁共振（ $^{13}\text{C-NMR}$ ）、X 射线光电子能谱（XPS）和傅里叶转换红外光谱等测试。基于对国际前沿研究工作良好的把握、严谨通畅的研究思路以及申请人所在单位和合作单位可搭建的高水平科研工作平台，本项研究工作具有良好的可行性。

五、项目计划进度：

本项目研究计划从 2019 年 6 月起至 2022 年 6 月止。研究计划如下：

（1）2019 年 6 月—2019 年 12 月：研究不同原料和不同热解温度对不同粒径 BC 产生的影响，并表征不同粒径 BC 物化特性差异，建立不同粒径 BC 的制备与表征方法，探究不同粒径 BC 颗粒在水体环境中的悬浮沉降行为和稳定性，并初步建立 BC 吸附 ATs 的方法和体系。

（2）2020 年 1 月—2020 年 6 月：利用吸附/解吸平衡模拟实验，研究不同粒径 BC 对本研究选定的典型 ATs 的吸附和解吸，筛选对 ATs 具有强吸附能力的 BC，揭示吸附机制与不同粒径 BC 特性间的内在关系。

（3）2020 年 7 月—2020 年 12 月：模拟水体环境条件，研究不同粒径 BC 颗粒对水体中 ATs 在水、悬浮物和沉积物中的分配，重点探讨不同粒径 BC 对 ATs 在水体环境中水解、光降解和生物降解的影响并揭示其内在机制。

（4）2021 年 1 月—2022 年 6 月：模拟水体环境条件，研究 BC 存在下 ATs 在“水体-植物-BC”系统中的生物有效性。

六、申请人所在学院意见：

研究内容合理，思路清晰，具有良好
理论价值与实践应用意义

负责人签字：

盖章：

2019年4月2日



七、主管部门意见：

负责人签字：

盖章：

2019年4月2日



填表说明：

- 1、纸制申请书1份及电子文档，博士论文1份一并上报。
- 2、必须由申请人所在学院负责人签字、盖章。
- 3、申请书左侧装订。



Taishan Academic Forum

泰山学术论坛

前沿交叉专题

Forum for Advanced Interdisciplinary Research

主办单位：山东省教育厅

承办单位：济南大学

支持单位：济南市政府、济南高新区管委会

时 间：2018.9.25-2018.9.28





Construction of rGO-C₃N₄/TiO₂ nanotube array photoelectrodes and its enhanced performance for photocatalytic degradation of rhodamine B

Bin Zhang, Yanjun Xin*

Qingdao Engineering Research Center for Rural Environment, College of Resources and Environment, Qingdao Agricultural University, Qingdao 266109, China.

The photoelectrode of titanium dioxide nanotube array was prepared by anodic oxidation method in this paper. rGO/C₃N₄/TiO₂ nanotube array electrode was successfully prepared by immersion method and electrochemical deposition. The effects of melamine concentration, times of immersion and GO concentration, deposition voltage, deposition time were investigated through photocatalytic degradation of Rhodamine B (Rh.B). Rh.B (5mg/L) degradation rate reached 68.7% under 60 min and reached 90.23% under 120 min by rGO/C₃N₄/TiO₂ nanotube array photocatalyst. Results showed that the photocatalytic performance of rGO/C₃N₄/TiO₂ nanotube arrays were greatly improved compared with that of TNAs.

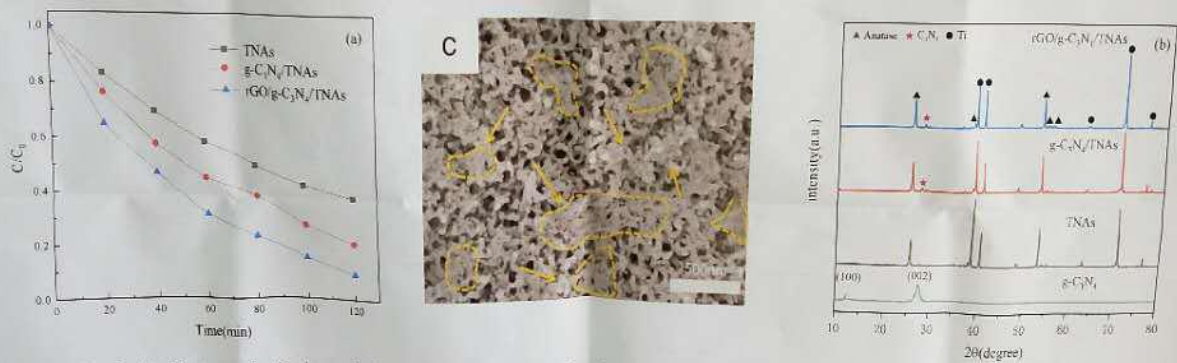


Fig.1. (a) Photocatalytic degradation of Rhodamine B (5mg/L, 40mL) under visible-light irradiation by rGO/C₃N₄/TiO₂; (b) SEM images of rGO/C₃N₄/TiO₂; (c) XRD spectra of TNAs, C₃N₄/TiO₂ and rGO/C₃N₄/TiO₂.

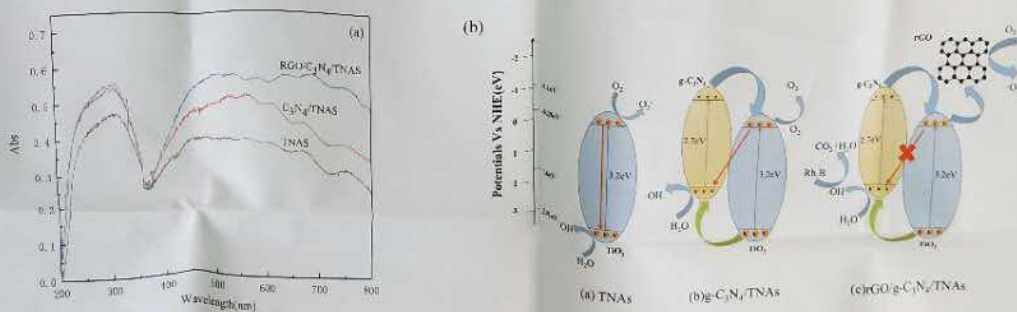


Fig.2. (a) UV-Vis absorption spectra of TNAs, C₃N₄/TiO₂ and rGO/C₃N₄/TiO₂; (b) Photocatalytic mechanism scheme of TNAs, C₃N₄/TiO₂ and rGO/C₃N₄/TiO₂.

Recent Publications:

1. G Wang, YJ Xin*, B Zhang, et al. *Electrochimica Acta*, 2016, 222, 1903-1913.
2. QH Chen, YJ Xin*, et al. *Chemical Engineering Journal*, 2016, 302, 377-387.
3. QH Chen, YJ Xin* et al. *Electrochimica Acta*, 2015, 186, 34-42.
4. QZ Zhang, YJ Xin* et al. *Journal of Alloys and Compounds*, 2015, 618, 761-767.
5. YJ Xin*, D Ma. *Chemical Engineering Journal*, 2014, 242, 162-169.
6. YJ Xin*, HL Liu*, et al. *Electrochimica Acta*, 2013, 104, 308-313.
7. YJ Xin, QH Chen* et al. *Journal of Alloys and Compounds*, 2018, 751.
8. YJ Xin*, HL Liu et al. *Journal of Hazardous Materials*, 2011, 192.
9. G Wang, YJ Xin* et al. *Chemical Engineering Journal*, 2018, 337.
10. YJ Xin*, HL Liu et al. *Journal of Materials Science*, 2011, 46.

2019年中欧膜产业技术创新合作大会

2019 Europe-China Cooperation Conference on Membrane Industrial Technology Innovation

签到处

SIGN IN



2019年中欧膜产业技术创新合作大会

2019 Europe-China Cooperation Conference on Membrane Industrial Technology Innovation

· 汇聚创新资源 膜力驱动发展 ·

主办单位

山东省科技厅 威海市人民政府 中国膜工业协会 欧洲膜学会

承办单位

威海市科技局 环翠区人民政府 哈尔滨工业大学(威海) 高等技术研究院 中欧膜技术研究院

中国·威海



继文

尤金德

2019 | 2019 Europe-China
Cooperation Conference on
Membrane Industrial
Technology Innovation

中欧膜产业技术
创新合作大会

工作证

STAFF

中国·威海 2019.7



2019年中欧 膜产业技术创新合作大会

2019 Europe-China Cooperation Conference on
Membrane Industrial Technology Innovation

—— 汇聚创新资源 膜力驱动发展 ——

2019 | 2019 Europe-China
Cooperation Conference on
Membrane Industrial
Technology Innovation

中欧膜产业技术
创新合作大会

代表证

GUEST

中国·威海 2019.7

手册

ing Manual

国·威海

hai·China

2019.7





哈尔滨工业大学
HARBIN INSTITUTE OF TECHNOLOGY

The 5th International Conference
Pollution and H

PROGRAM

August 4-6, 2019 Harbi



The 5th International Conference on Environmental
Pollution and Health

Bin ZHANG

Harbin Institute of Technology

Harbin, P.R.China
August 4-6, 2019





ROYAL SOCIETY
OF CHEMISTRY



Royal Society of Chemistry Volunteer Certificate of Appreciation

This is awarded to

Bin Zhang

In recognition of outstanding service
as a volunteer at

The 4th Fellow of the Royal Society of
Chemistry (FRSC) Forum on **Global Challenges
and Chemistry Solutions: Water Safety**

20 August 2019
Heilongjiang, China





ROYAL SOCIETY
OF CHEMISTRY



The 4th Fellow of the Royal Society of Chemistry
(FRSC) Forum on Global Challenges and
Chemistry Solutions: Water Safety

第四届英国皇家化学会会士论坛 (2019)：化学解决全球挑战之水安全篇

Venue: Room 613
613会议厅

The 4th Fellow of the Royal Society
of Chemistry (FRSC) Forum on
Global Challenges and Chemistry
Solutions: Water Safety



20 August 2019
Harbin, China

20 August 2019

Dear

**The 4th Fellow of the Royal Society of Chemistry (FRSC) Forum on Global
Challenges and Chemistry Solutions: Water Safety
20 August 2019, Harbin, Heilongjiang Province, China**

Thank you for your attendance at the above-mentioned conference. Your expertise
and experience have greatly enhanced the quality of this conference.

We are looking forward to see you in our future events!

Best regards,

RSC China Events Team

China Events Team

Royal Society of Chemistry
Office 1216, Level 12
Chong Hing Finance Centre
288 West Nanjing Road
Huangpu District
Shanghai 200003, China
RSCChina@rsc.org

Royal Society of Chemistry: www.rsc.org



Joining Instruction: the 4th FRSC Forum on Global Challenges and Chemistry Solutions: Water Safety

RSC China <shared>

详情

The 4th Fellow of the Royal Society of Chemistry (FRSC) Forum on Global Challenges and Chemistry Solutions: Water Safety



20 August 2019
Harbin, China

Dear Mr Zhang,

It is our great pleasure to welcome you to participate the forthcoming forum. We sincerely thank you for taking time and effort to attend the event.

Before the event, there are several more things we would like to pay your attention:

1. Venue

The venue is located at the **613 Meeting Room, State Key Laboratory of Urban Water Resources and Environment**, Harbin Institute of Technology (The Second Campus) (哈尔滨工业大学二校区城市水资源与水环境国家重点实验室613会议厅) and the main entrance is South Gate on Huanghe Road (黄河路南校门).

2. Registration

The registration will start at **8:00am** on 20 August. Please collect the conference materials at the registration desk before the Forum begins.

3. Catering

Lunch is arranged at the second floor of Jinxiu canteen (锦绣食间二楼自助餐厅) close to the venue.

4. Download electronic copy of materials

请在会议网站或扫描二维码下载会议手册、议程及说明

Please download the abstract book, programme or joining instructions on the [event website](#) or by scanning the QR Code below. The password for abstract book is **FRSC2019**.





Welcome 欢迎 2019 em Welcome 欢迎 Welcome 欢迎
第二十二次·全国环境微生物学学术研讨会
The 22nd Chinese National Symposium on Environmental Microbiology

—环境微生物学的新挑战与机遇—

中国·哈尔滨 8.12-8.15

- 主办单位:**
- 中国微生物学会环境微生物学专业委员会
- 承办单位:**
- 哈尔滨工业大学环境学院
 - 城市水资源与水环境国家重点实验室
 - 城市水资源开发利用(北方)国家工程研究中心

- 协办单位:**
- 黑龙江大学生命科学学院
 - 哈尔滨师范大学
 - 东北农业大学
 - 黑龙江八一农垦大学

- 赞助单位:**
- 上海曼微仪器有限公司
 - 凯杰企业管理(上海)有限公司
 - 上海凌德生物科技有限公司
 - 广州基德奥生物科技有限公司
 - 上海锐昂生物科技有限公司
 - 长春长光辰域生物科技有限公司
 - 太平洋生物